UNIVERSITY OF SOUTHAMPTON

FACULTY OF PHYSICAL SCIENCES AND ENGINEERING

Optoelectronics Research Centre

Polycrystalline silicon waveguides for integrated photonics

by

Yohann Franz

Thesis for the degree of Doctor of Philosophy

June 2018

UNIVERSITY OF SOUTHAMPTON

ABSTRACT

FACULTY OF PHYSICAL AND APPLIED SCIENCES

Optoelectronics Research Centre

Thesis for the degree of Doctor of Philosophy

POLYCRYSTALLINE SILICON WAVEGUIDES FOR INTEGRATED PHOTONICS

by Yohann Franz

Silicon photonics is an expanding domain of research since its booming a decade ago. Leveraging decades of research and development from the electronics industry, silicon photonics is the ideal candidate to overcome the bottleneck that microelectronics is facing with regard to the interconnect bandwidth limitations. In addition to being a platform compatible for both photonics and electronics, silicon is transparent in the mid-infrared regime, has a high refractive index for tight light confinement (i.e., small footprints), and presents a high nonlinear refractive index that is of high interest for optical signal processing applications. However, the integration of a silicon photonic layer is still challenging due to either the deposition flexibility or the material quality.

In this thesis, a technique is presented to integrate a silicon layer with the deposition flexibility of amorphous silicon and the material quality of crystalline silicon, whilst being low-cost and having a thermal budget of < 450 °C making it compatible with the CMOS technology. Using a laser treatment, the as-deposited amorphous silicon is locally crystallised into polycrystalline silicon, a composite material of made of crystalline silicon crystallites surrounded by an amorphous silicon matrix. Both film and wire structures are processed and the material quality is assessed through optical microscopy, Raman spectroscopy, and X-ray diffraction. The optical quality of the polycrystalline wire waveguides is also investigated in the linear and nonlinear regime.

In parallel to the planar silicon photonics geometry, silicon core fibres are also investigated in this work. These novel fibres offer the capability to integrate the functionality of silicon photonics platforms directly inside fibre architectures. Amorphous core fibres can be drawn with the lowest losses but as for the planar geometry, the material lacks electronics capabilities. On the other hand, polycrystalline silicon core fibres, which are suitable for both optical and electrical applications, can be drawn but their propagation losses remain high. In this work, two silicon core fibre material improvement methods, based on laser recrystallisation and tapering, are presented. To assess the material improvement, fibres are analysed through optical microscopy, Raman spectroscopy and X-ray diffraction. Finally, the optical losses of the improved fibres are measured on an optical transmission setup.

Table of Contents

List of Tables

List of Figures

Declaration of Authorship

I, Yohann Franz, declare that the thesis entitled *Polycrystalline silicon waveguides for integrated photonics* and the work presented in the thesis are both my own, and have been generated by me as the result of my own original research.

I confirm that:

1. This work was done wholly or mainly while in candidature for a research degree at this University;
2. Where any part of this thesis has previously been submitted for a degree or any other qualification at this University or any other institution, this has been clearly stated;
3. Where I have consulted the published work of others, this is always clearly attributed;
4. Where I have quoted from the work of others, the source is always given. With the exception of such quotations, this thesis is entirely my own work;
5. I have acknowledged all main sources of help;
6. Where the thesis is based on work done by myself jointly with others, I have made clear exactly what was done by others and what I have contributed myself;
7. Parts of this work have been published as: See Appendix A: List of publications

Signed: YOHANN FRANZ 

Date: 19 May 2018

Acknowledgements

I would like to sincerely thanks my two supervisors Anna Peacock and Sakellaris Mailis who supported me throughout this long project. For their continuous guidance in the experimental work but also in the redaction of the different reports. For giving me the opportunity to accomplish my thesis at the Optoelectronics Research Centre and believing in me. Thank you.

I also want to extend my thanks to the many colleagues and friends I met during my time at the University of Southampton. To Gregorio Jimenez Martinez, Gregoris Zisis and Antoine Runge for their help at work but also outside university. To Noel Healy for sharing his fruitful knowledge and lab experience. To Neil Session for taking the time to train me on the numerous tools. To Harold Chong, Taha Ben Masoud, Rafidah Petra and Antulio Tarazona for helping me on the samples fabrication with my extended gratitude to SweZin Oo for sharing her fabrication knowledge with me. To Konstantin Ignatyev for his guidance at the beamline at the Diamond Light Source facility. I would like to thank all my coauthors for the different projects, for their collaboration, help and cross checks. And I also want to thank the members of the group I have been working with, Li Shen, Fariza Suhailin, Haojie Zhang, Haonan Ren and Ozan Aktas, and seize the opportunity to wish good luck to Stuart MacFarquhar for continuing this project.

Besides work, I also want to thank people from both Recbad and Eagles badminton clubs for giving me some balance, for the international experiences and for the different personal achievements. I also want to thank both Justus Tobias Tsang and Antoine Runge for their support and many helpful conversations.

Last but not least, I want to Engineering and Physical Sciences Research Council for supporting the research leading to these results (EP/P000940/1 and EP/J004863/1 grants). I further acknowledge the use of the beamline i18 at the Diamond Light Source Facility (SP13025) in the completion of this work.

Finally, a huge thanks to my parents, Béatrice and Daniel Franz, for their lifelong support in ups and downs. Merci.

Definitions and Abbreviations

Al_2O_3	aluminium oxide
a-Si	amorphous silicon
a-Si:H	hydrogenated amorphous silicon
BOX	buried oxide
BS	beam splitter
C_4F_8	octofluorocyclobutane
CaO	calcium oxide
CLC	continuous wave laser crystallisation
c-Si	crystalline silicon
CVD	chemical vapour deposition
CW	continuous wave
DIC	differential interference contrast
e-beam	electron beam
FCA	free carrier absorption
FOM	figure of merit
FSR	free-spectral range
FWHM	full width at half maximum
GVD	group velocity dispersion
H_2	dihydrogen
He	helium
HF	hydrofluoric acid
HPCVD	high-pressure chemical vapour deposition
HWCVD	hot-wire chemical vapour deposition
HWHM	half width at half maximum
ICP-RIE	inductively coupled plasma reactive etching
IR	infra-red
$K_2Cr_2O_7$	potassium dichromate
LA	longitudinal acoustic
LO	longitudinal optical
MC	molten core
MCD	molten core drawing
µc-Si	micro-crystalline silicon
MOF	microstructured optical fibre
NA	numerical aperture
nc-Si	nano-crystalline silicon
NLSE	nonlinear Schrödinger equation
OSA	optical spectrum analyser
PECVD	plasma-enhanced chemical vapour deposition
p-Si	polycrystalline silicon
RF	radio frequency
RIE	reactive ion etching
RMS	root mean square

sccm	standard cubic centimeters per minute
SEM	scanning electron microscope
SF_6	sulfur hexafluoride
SiGe	silicon germanium
SiH4	silane
SiN	silicon nitride
SOI	silicon on insulator
SPM	self-phase modulation
TE	transverse electric
TFT	thin film transistor
TM	transverse magnetic
TO	transverse optical
TPA	two-photons absorption
UV	ultra-violet
XRD	X-ray diffraction

Chapter 1

Introduction

1.1 Introduction to silicon photonics

Profiting from decades of research and development in electronics, silicon is the semiconductor that has been hoisted as the leading material for microelectronics and is now the backbone of most of integrated chips. In the early 1980s, silicon was introduced as an optical material as, in addition to its electronics capabilities, it also possesses many attractive optical properties such as a high refractive index ($n_{Si} = 3.45$) for strong mode confinement, a broad transparency window covering the telecommunication wavelengths, and high nonlinear coefficients useful for signal processing applications [1]. One of the key advantages of silicon as an optical medium is its potential for integration with electronics via the already well-developed silicon on insulator (SOI) technology. Therefore, silicon photonics emerged with the pioneering work done by Soref et al. [2], from which several milestones were achieved with silicon-based waveguides, modulators and switches [3][4]. However, silicon photonics really started to boom in the 2000's when limitations began to appear in microelectronics due to the growing bandwidth demand for communications [10][11]. With the metal interconnects tending toward their physical limits, optical solutions with higher bandwidth capacities have been explored within silicon photonics [7][8][9]. Leveraging the mature electronics silicon technology, silicon photonics developed rapidly and today, many building blocks for photonic circuitry are now available on the SOI platform. Light in silicon can be guided in micrometre and sub-micrometre waveguides [10][11], modulated using Mach-Zehnder interferometers [12] or ring resonators [13] and recently, light has also been generated in silicon-based lasers despite the challenging indirect band gap present in silicon [14][15]. For detection, silicon being transparent at

telecommunication wavelengths, the incorporation of other materials such as group III-V semiconductors or germanium, is commonly used in the fabrication process [16][17].

Nevertheless, co-integrating both electronics and photonics on the same chip is still an ongoing work. As of to date, the solutions that have been proposed are still too expensive to compete with the very large scale integration process of microelectronics. Depending on the targeted application, different silicon allotropes and processing techniques are still being investigated.

1.2 Polycrystalline silicon as a promising material

Solid silicon comes in two allotropes: the amorphous form (a-Si) and the crystalline form (c-Si). The first one, in addition to being a low loss material when doped with hydrogen [18] [19], can easily be back-end integrated, stacked on-top of a pre-existing chip or substrate, onto a large variety of substrates using chemical vapour deposition (CVD) techniques with processing temperatures as low as 100 °C [20], [21]. In the electronics industry, many samples have a 450 °C thermal budget to prevent the deterioration of metallisation contacts [22]. However, a-Si is a poor material for electronic functionality and, when exposed to high optical intensities, the material quality can degrade because of the Staebler-Wronski effect [23][24]. The alternative is to use c-Si materials that can be used for both electronics and photonics applications and has low optical losses. However, the lack of deposition flexibility of c-Si materials, that has to be either grown epitaxially or sample bonded, makes the integration of a photonics layer difficult. Also, due to the different SOI thickness standards between electronics and photonics, the front-end integration is expensive as it requires local BOX layer modifications for the light to be sufficiently isolated from the substrate [25], whilst the large photonics footprint, compared to electronics, reduces the integration density [26]. Furthermore, although c-Si photonics layers can be back-end integrated using a thin film transfer technique such as bonded SOI or SmartCut, these methods have processing temperatures that are usually incompatible with CMOS substrates [27], [28]. Flip-chip method has also been used but requires high precision during the tedious manual peeling and alignment steps [29].

Fortunately, an intermediate silicon material offering the deposition flexibility of the a-Si whilst having material and optical properties close to the c-Si exists. Polycrystalline silicon (p-Si), is a composite material formed of crystalline silicon grains surrounded by an amorphous silicon matrix. Depending on the size and number of crystals present in the p-Si, different degrees of crystallinity can be defined as represented in Figure 1.1. For the low-crystallinity p-Si, the crystal boundaries, which are composed of amorphous material with dangling bonds and impurities, generate a lot of losses by scattering both photons and electrons [30], [31]. For high-crystallinity p-Si, the larger and less numerous crystals result in a reduction of the lossy crystal boundaries, thus the material is tending toward crystalline-like material.

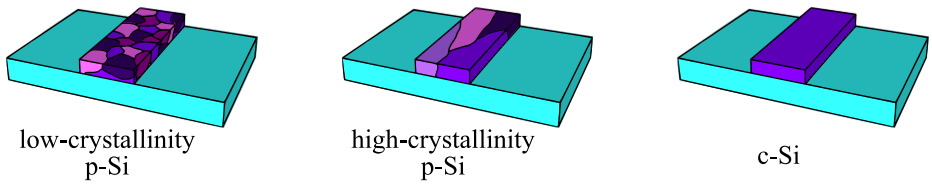

Figure 1.1: Different degrees of crystallinity for silicon material.

Since pioneering work on polycrystalline photonics [32], much progress has been made on both passive and active devices [33][34][35]. However, because the fabrication process of p-Si devices either involves the CVD of amorphous silicon material at high temperature to ignite crystallisation during deposition, or the post heat treatment of an as-deposited a-Si layer, the high thermal budget is usually incompatible for back-end integration on many substrates such as CMOS chips. At temperatures beyond 450 °C, the metallisation layers can be damaged and the dopants can diffuse [22]. To address this issue, laser crystallisation has been investigated to locally heat treat the material by focusing a laser beam onto a-Si surface. Using this technique, the melted a-Si recrystallizes into p-Si whilst the substrate, which can have a low thermal budget, is protected from the heat front by a CVD silica layer [36]. Based on this method, p-Si thin film transistors (TFTs)[37] and waveguides [38] have already been developed but further work has to be realised to reduce the losses of these p-Si devices. The development of this method for the fabrication of high crystallinity p-Si waveguides with a low thermal budget is the focus of this research. This project was supported by the recent observation of 200 µm long crystals in silicon core fibres laser processed by our group at this time.

1.3 Introduction to optical silicon core fibres

In parallel to the development of planar silicon devices, silicon photonics has recently been introduced to the fibre geometry [39][40][41]. Based on different fabrication methods, silicon core fibres have losses now competing with their planar counterparts and are of great interest for nonlinear applications due to their potential for long interaction lengths combined with the high nonlinear coefficient of silicon [42][40][43]. In addition, the silicon core fibres also have high damage thresholds. Furthermore, the seamless integration of these waveguides with well-developed conventional silica fibre technology opens up the road to all-optical fibre systems and optoelectronics devices with junctions and other electronic functions directly written into the fibre [40][44]. The effort put in the development of optical silicon core fibres is represented in Figure 1.2(a) where both publications and citations numbers are growing since 2006.

Silicon fibres can be drawn either by high-pressure CVD (HPCVD) or by the molten core drawing (MCD) technique [39][42]. Whilst the later only allows for the drawing of large cores with p-Si material, the first technique can produce both a-Si:H and p-Si core material, depending on the processing temperature, and gives access to micrometre core sizes. Figure 1.2(b) shows the progress

realised on the material quality with the propagation losses for different drawing techniques and materials. As for the planar geometry, a-Si:H has the lowest losses but lacks electronics capabilities [43]. On the other hand, p-Si losses are improving with the MCD techniques, but further progress is still required on improving the material quality.

As for the planar geometry, the purpose of this thesis is to improve the material quality of these p-Si core fibre. Starting with MCD silicon core fibres, two different improvement techniques will be used: laser processing, which consists of recrystallising p-Si crystals into larger crystals [45], and tapering, which uses a heat treatment to increase the crystal sizes whilst simultaneously the reducing core size [46].

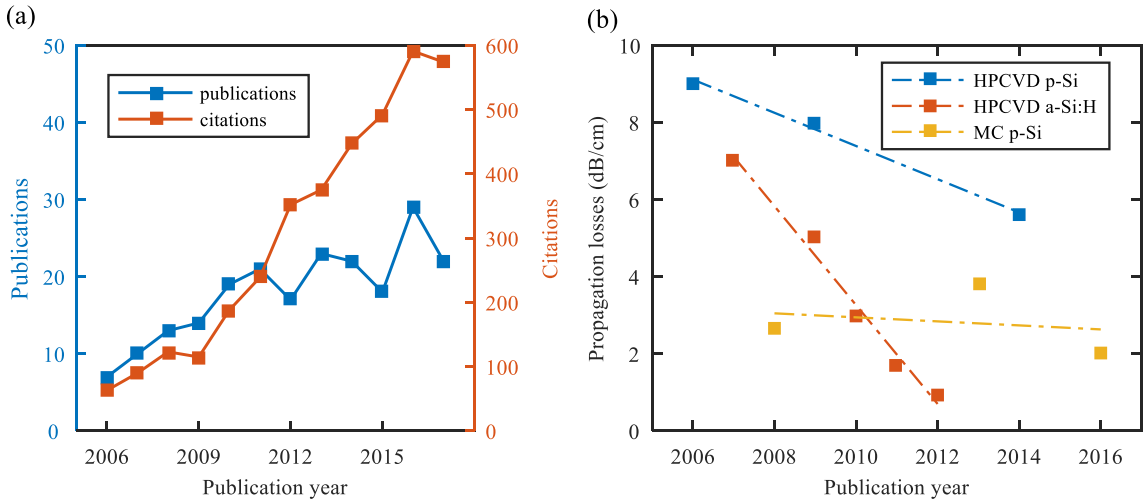

Figure 1.2: (a) Progression in time of silicon optical fibre journal publications and citations, (b) Optical propagation losses progress in the silicon optical fibres fabricated by both HPCVD and MC methods; dashed lines are given as guides to the eye. (from [39], [42]–[45], [47]–[51])

1.4 Thesis outline and contributions

Chapter 2 presents a brief background to optical waveguiding and silicon-based waveguides. It begins by describing how an optical wave propagates within a rectangular structure in the case of a planar waveguide, and within a cylindrical structure in the case of a silicon core fibre. The mode distribution is then detailed with emphasis on some particular parameters such as the mode area or optical dispersion. Later, the different silicon based materials used in waveguiding are discussed with an emphasis on silicon nitride, amorphous silicon, crystalline silicon and polycrystalline silicon. A description of polycrystalline silicon deposition techniques and their optical losses is finally made to position this project.

Chapter 3 describes the different tools used to fabricate and characterise the different waveguides presented in this thesis. Starting with planar waveguides, both plasma-enhanced and hot-wire CVD techniques are introduced. Then, photolithography and e-beam lithography processes for mask transfer are presented along with the etching step. The second part describes the fabrication process of and MCD fibres. Finally, the characterisation methods are introduced, starting with the instruments used to estimate the material quality of the waveguides fabricated for this project. Both Raman spectroscopy and X-ray diffraction techniques are described along with a brief review of their operation principle to explain how the results are extracted from their data. Then, the tools used for optical characterisation are presented along with a description of a sample facets preparation for analysis. Once the presentation of the different elements used in our optical transmission setup have been presented, the chapter ends with a summary of the different planar samples generations and their individual characteristics used during this thesis.

Chapter 4 is dedicated to the experiments and results obtained on laser crystallisation of thin silicon films. Serving as a preliminary work to validate our laser writing setup, different parameters such as laser scanning speed and laser power are investigated. Following laser processing, the samples are characterised through optical microscopy and Raman spectrometry before being sacrificially etched in an acidic solution to reveal our first observation of silicon crystal grains. The chapter ends on the presentation of direct laser writing of optical devices onto silicon using our 2D stages. This last experiment serves as a proof of concept and is not investigated in more details as it is not part of this project.

Chapter 5 is a comprehensive summary of the experiments undertaken on patterned silicon waveguides along with their results. The first part of this chapter studies the influence of the different fabrication parameters such as silicon film thickness or the width of the wire waveguide. From these results, the last and most optimised sample generation is used for a full characterisation. In addition to the microscope observations and Raman measurements, X-ray diffraction and optical loss measurements are used to assess the p-Si material quality after laser processing. As in the case of the planar samples, some samples are sacrificed into an acidic solution to reveal different crystals patterns, with the largest crystals observed for the most optimised waveguide and laser processing parameters. Finally, with optical losses being low enough, preliminary nonlinear measurements were performed to assess the quality of the processed waveguide for the observation of nonlinear dynamics.

Chapter 6 presents the work undertaken on the fibre platform with MCD silicon core fibres. The first part of this chapter focuses on a p-Si fibre recrystallized by laser processing. The material quality of the fibre after laser recrystallisation is assessed through X-ray diffraction and optical loss measurements. Results show that by adjusting the laser scanning speed and power, larger crystals can be obtained, thus revealing a higher material quality with lower losses. The second half of this chapter presents the results on tapered silicon core fibres. After a brief description of the setup used,

the material improvement is assessed through Raman spectroscopy, X-ray diffraction and optical loss measurements. All these results reveal a clear material quality improvement in addition of a tunable final core size. A last experiment consisting of removing the silica cladding reveals a smooth core/cladding interface.

Chapter 7 draws conclusions on the different results achieved throughout this thesis. High quality low-temperature p-Si waveguides deposition, crystals observations and optical loss measurements are the key topics discussed in the first part of this conclusion. The second part focuses of the silicon core fibres and the improvement in crystals size and core diameter in the case of fibre laser recrystallisation and fibre tapering, respectively. Finally, the different opportunities accessible through the work presented in this thesis are discussed.

The author is responsible for all the work presented in this thesis under the supervision of Prof. Anna Peacock and Dr. Sakellaris Mailis.

The silicon films used in Chapter 4 and Chapter 5 have been deposited by members of Dr Harold Chong's group in the ECS department. In Chapter 5, the a-Si wires patterned by SEM lithography along with the silica capping when required have been produced by members of Dr. Harold Chong's group, particularly Taha Ben Masoud, SweZin Oo and Antulio Tarazona.

The silicon core fibre preforms used in Chapter 6 were prepared by Prof. Ursula Gibson's group at Norwegian University of Science and Technology and drawn at Clemson University by members of Prof. John Ballato's group. The laser processing of the fibres was performed by Dr. Michael Fokine at the KTH Royal Institute of Technology and the X-ray measurements of these laser treated fibres have been realised by Dr. Noel Healy at Diamond Light Source. The tapering of the silicon core fibres has been realised by Haonan Ren, while the optical loss measurements of these fibres have been jointly done by Haonan Ren and I.

Finally, the Matlab code of the generalised nonlinear Schrödinger equations used in Chapter 5 for nonlinear simulation has been originally written by Prof. Anna Peacock and has been modified by Dr. Li Shen and Dr. Priyanth Mehta.

Chapter 2

Background

2.1 Introduction

In this chapter, the different background elements required to understand the waveguiding and materials requirements of this thesis are presented. It starts by describing optical waveguiding within rectangular structures for the case of planar waveguides, and then within a cylindrical structure for the case of the silicon core fibres. Key notions of waveguiding structures and optical mode distribution such as numerical aperture, the wave equations, mode effective areas and dispersion are then introduced.

The second part of this chapter details the different silicon-based material used in photonics. Silicon nitride, hydrogenated amorphous silicon, crystalline silicon and finally polycrystalline silicon materials are presented along with their deposition methods and the current state of art material quality, in order to position objectives of this thesis with respect to the literature. There is a particular emphasis for polycrystalline as this material is at the core of this project.

2.2 Optical waveguiding

2.2.1 Waveguide structures

In this thesis, two different waveguide geometries are used: planar-based wire waveguides and cylindrical single core fibres. These are both illustrated in Figure 2.1 for a propagation along the z axis. The first structure consists of a silicon wire with a height h, a width w and a refractive index n_2

deposited onto a silica substrate with a refractive index n_1. Results obtained on this structure are presented in Chapter 4 for the case of an infinite slab of silicon elongated in the x direction and in Chapter 5 for the case of wire of width w. Results obtained on the single core fibres are presented in Chapter 6. Optical waveguiding in both of these structures is ensured by the strong index difference between the silicon core material and the surrounding silica/air cladding confining light in the waveguide by total internal reflection.

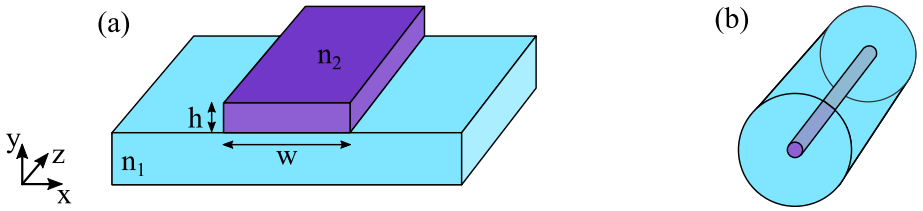

Figure 2.1: Illustrations of the waveguide structures used in this thesis. (a) planar-based wire waveguide and (b) cylindrical single core fibre.

One of the key characteristics of these structures is their numerical aperture (NA), denoting the maximum light acceptance angle θ for a waveguide. NA is defined by:

$$NA = n \sin(\theta) = \sqrt{n_2^2 - n_1^2}, \tag{2-1}$$

With n the refractive index of the incident ray medium, air in this thesis, and θ the critical angle from Snell-Descartes law corresponding to the transmission and reflection transition [52]. The large value of NA for a silicon core waveguide indicates that optical rays with many different incident angles can be collected and transmitted into the waveguide.

Another characteristic of these structures is the normalised frequency denoted by the letter V and defined as:

$$V = k_0 \, d \sqrt{n_2^2 - n_1^2}, \tag{2-2}$$

with k_0 the free-space wavevector related to the wavelength λ by $k_0 = 2\pi/\lambda$ and d the dimension of the waveguide. For the wire structure, d corresponds to either the width or the height if the normalised frequency is calculated along the x or y axis whilst in the case of fibre waveguide, d corresponds to the core radius [27], [53]. The normalised frequency, also named V-number, is used to calculate the number of modes optically guided in the structure thus determining if the waveguide is single mode or multimode. For a single core fibre, the core is multimode when $V > 2.405$ [27] whilst for a symmetric slab, the critical point at which the higher-order modes are cut off corresponds to $V = \pi/2$ [54]. For asymmetrical structures such as the wire presented in Figure 2.1(a), the highest refractive index is usually used as the cladding index [55].

2.2.2 Optical mode distribution

The distribution of the electric and magnetic fields in a waveguide can be derived from Maxwell's equations. By combining the different relations, the wave equations describing the electric field and the magnetic field distributions are then obtained for either Cartesian or cylindrical coordinates system depending on the waveguide geometry.

For a planar slab waveguide infinitely elongated in the x direction, the electric and magnetic field distributions in the xy plane, in absence of current density, can be described using the following wave equations [56]:

$$\nabla^2\mathbf{E} = \mu_m\varepsilon_m\frac{\partial^2\mathbf{E}}{\partial t^2}, \tag{2-3}$$

$$\nabla^2\mathbf{H} = \mu_m\varepsilon_m\frac{\partial^2\mathbf{H}}{\partial t^2}, \tag{2-4}$$

with μ_m and ε_m the permeability and the permittivity of the medium, respectively. Propagating plane waves are solutions to these wave equations, thus the electric field can be written as follows:

$$\mathbf{E}(x,y,z) = \mathbf{E}(x,y)e^{-i\beta z}e^{i\omega t}, \tag{2-5}$$

where β is the propagation constant and $e^{i\omega t}$ represents the time dependence.

In the case of a transverse electric (TE) mode in a slab, the electric field is polarised in the x direction, is invariant along the infinite x axis, and is periodically varying along the propagating z axis. Hence, the electric mode distribution in this case can be described by:

$$\frac{\partial E_x(y)}{\partial y} - \left(k_0^2 n_i^2 - \beta^2\right)E_x(y) = 0, \tag{2-6}$$

where $k_0 = \omega/c$, $n_i = c\sqrt{\mu_i\varepsilon_i}$ is the refractive index of the i-th medium corresponding to either the substrate, the core, or the cladding, and $c = \sqrt{\mu_0\varepsilon_0}$ is the speed of light in the vacuum related to μ_0 and ε_0, the permeability and the permittivity of the vacuum, respectively. Similar equations can be derived for **H** and transverse magnetic (TM) cases.

For a fibre waveguides, the electric field and wave equation in the cylindrical coordinates system are written as follows [55]:

$$\mathbf{E}(r,\theta,z) = \mathbf{E}(r,\theta)e^{-i\beta z}e^{i\omega t}, \tag{2-7}$$

$$\frac{\partial^2 E_z}{\partial r^2} + \frac{1}{r}\frac{\partial E_z}{\partial r} + \frac{1}{r^2}\frac{\partial^2}{\partial \theta^2} + \left(k_0^2 n_i^2 - \beta^2\right)E_z = 0, \tag{2-8}$$

The transverse electric fields are then related to the E_z and H_z fields by:

$$\begin{cases} E_r = -\dfrac{i}{(k_0^2 n_i^2 - \beta^2)} \left(\beta \dfrac{\partial E_z}{\partial r} + \dfrac{\omega \mu_0}{r}\dfrac{\partial H_z}{\partial \theta}\right) \\ E_\theta = -\dfrac{i}{(k_0^2 n_i^2 - \beta^2)} \left(\dfrac{\beta}{r}\dfrac{\partial E_z}{\partial \theta} + \omega \mu_0 \dfrac{\partial H_z}{\partial r}\right) \end{cases}, \tag{2-9}$$

Similar equations can be derived for **H** [55].

For both waveguide types, the propagation constant β corresponds to a guided mode solution in the structure and an effective refractive index n_{eff} is attributed to each of these modes as defined below:

$$\beta = n_{eff}\, k_0\,, \tag{2-10}$$

Solutions to Equations (2-6) and (2-9) are obtained by applying the boundaries conditions at the substrate/core and core/cladding interfaces. Whilst these solution can be obtained analytically for simple cases such as a symmetrical slab, more complex structures such as wire waveguide usually require numerical approach as shown in Chapter 5.

Finally, an important characteristic of an optical mode is its effective area A_{eff} which describes the mode distribution and confinement in an xy plane of the waveguide. In a Cartesian coordinates system, A_{eff} is defined as:

$$A_{eff} = \frac{\left[\iint_{-\infty}^{+\infty} |E(x,y)|^2 \, dxdy\right]^2}{\iint_{-\infty}^{+\infty} |E(x,y)|^4 \, dxdy}\,, \tag{2-11}$$

This characteristic is often used to quantify the size of the nonlinear effects in a waveguide as these are related to the intensity of the field, and thus the mode area. The effective area is also used to estimate the coupling losses caused by mode mismatch at the waveguide facet. The second factor influencing the loss injection is due to Fresnel back reflection, defined by:

$$R = \left(\frac{n_2 - n_i}{n_2 + n_i}\right)^2, \tag{2-12}$$

with n_2 and n_i the refractive indices of the core and incident beam medium, respectively.

2.2.3 Dispersion

In vacuum, the velocity of an electromagnetic wave is c. However, in a waveguide, the propagation of an electromagnetic wave is governed by two different dispersion mechanisms: the material

dispersion and the waveguide dispersion. The first mechanism, also known as the chromatic dispersion, induces a frequency-dependent phase shift in the propagating wave and is represented by $n(\omega)$. This phenomenon can easily be observed during the propagation of a short temporal pulse as the different frequency components, traveling at different velocities, participate to the broadening of the pulse. The second mechanism is an effect of the waveguide geometry and refractive indices combination resulting in an effective index n_{eff}.

The overall dispersion in a waveguide can be accounted for by expanding the propagation constant β in a Taylor series about the centre frequency ω_0 [57]:

$$\beta(\omega) = \beta_0 + \beta_1(\omega - \omega_0) + \frac{1}{2}\beta_2(\omega - \omega_0)^2 + \frac{1}{6}\beta_3(\omega - \omega_0)^3 + \cdots \quad , \qquad (2\text{-}13)$$

where:

$$\beta_m = \left(\frac{d^m\beta}{d\omega^m}\right)_{\omega=\omega_0} \quad (m = 0, 1, 2, 3, \ldots). \qquad (2\text{-}14)$$

In Equation (2-14), β_m is the m^{th} order dispersion but in this thesis, due to the short length of our waveguides, only β_1 and β_2 are needed to be able to calculate the dispersion effect of an optical pulse. The first, β_1, and the second, β_2, order dispersion coefficients are related to the refractive index by:

$$\beta_1 = \frac{1}{v_g} = \frac{1}{c}\left(n + \omega\frac{dn}{d\omega}\right) \quad , \qquad (2\text{-}15)$$

$$\beta_2 = \frac{1}{c}\left(2\frac{dn}{d\omega} + \omega^2\frac{d^2n}{d\omega^2}\right) . \qquad (2\text{-}16)$$

The parameter β_1 is related to the group velocity v_g which represents the velocity at which the pulse envelop propagates and is related to the group index n_g by $v_g = c/n_g$. However, the phase velocity is defined by $v_{ph} = c/n_{eff}$. The parameter β_2, referred as the group velocity dispersion (GVD), represents the rate at which the optical pulse is spreading. If $\beta_2 > 0$, this is the normal dispersion regime and red-shifted wavelengths propagate faster than blue-shifted wavelengths [58]. If $\beta_2 < 0$, this is the anomalous dispersion regime and red-shifted wavelengths propagate slower than blue-shifted wavelengths. Finally, if $\beta_2 = 0$, this is the zero-dispersion wavelength and higher orders of dispersion are required to calculate the dispersion.

In semiconductor materials, the wavelength-dependence of the refractive index is well approximate by the Sellmeier equation defined as [59]:

$$n^2(\lambda) = 1 + \sum_{i=1}^{m} \frac{A_i \lambda^2}{\lambda^2 - B_i^2}, \tag{2-17}$$

with A_i and B_i the different fitting coefficients. For crystalline silicon material, the refractive index has been fitted using [60]:

$$n^2(\lambda) = 1 + \frac{10.6684293\,\lambda^2}{\lambda^2 - 0.301516485^2} + \frac{0.0030434748\,\lambda^2}{\lambda^2 - 1.13475115^2} + \frac{1.54133408\,\lambda^2}{\lambda^2 - 1104^2}, \tag{2-18}$$

For the waveguide dispersion, β is usually calculated numerically by solving the Maxwell's equations as shown in Section 2.2.2. For each guided mode, the equation eigenvalue gives an effective refractive index n_{eff} can be calculated and the waveguide dispersion can be added to the material dispersion in order to obtain the overall dispersion.

2.3 Silicon-based waveguides

In this section, different silicon-based materials commonly used for waveguide fabrication and their basic optical properties are presented. Starting with a brief presentation of the low-loss silicon nitride, the three different forms of silicon, represented in Figure 2.2, are introduced with an emphasis on polycrystalline silicon and its different depositions methods.

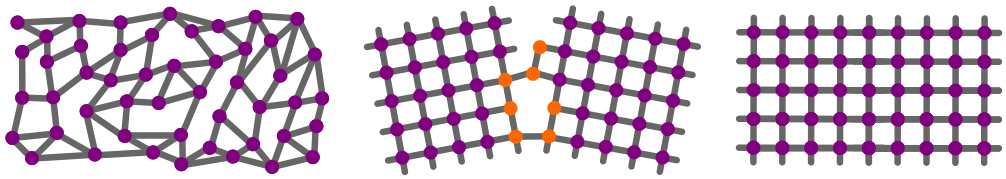

Figure 2.2: Schematic of silicon atoms in three different solid forms. (a) amorphous, (b) polycrystalline and (c) crystalline.

2.3.1 Silicon nitride

In recent years silicon nitride (Si_3N_4) has become an attractive passive material for waveguides of centimetre long lengths, and less, due to its flexible deposition techniques. In the past, silicon nitride (SiN) waveguides were mainly used in the visible domain owing to the fact that the deposition thickness was limited to ~250 nm, not high enough for infra-red (IR) structures with a refractive index of 1.99 at 1.55 μm [61]. This was because, if the structure is too high, tensile stress appears during the deposition and forms cracks that generate a lot of loss. However, this limitation was

overcome by using low-pressure CVD with multi thermal deposition steps [62], or using PECVD with alternate low and high frequencies during the deposition [63]. The first method demonstrated SiN waveguides with losses below 1 dB/cm but requires deposition at 800 °C and a thermal treatments at 1200 °C [62][64]. The later method based on PECVD results in waveguides with propagation losses of 3~4 dB/cm at 1.55 µm, but with a thermal budget below 450 °C thus compatible for back-end integration [63][65]. By playing with the silicon/nitrogen ratio, SiN can also be deposited at low temperature with propagation losses of ~1.5 dB/cm [66]. However, as for a-Si, SiN lacks good electrical properties and thus remains a material essentially used for the fabrication of passive devices [67].

2.3.2 Hydrogenated amorphous silicon

In photonics, amorphous silicon is appreciated for its low losses, its deposition flexibility and its nonlinear capabilities. The amorphous state of silicon is usually deposited by CVD making the material easy to integrate with processing temperatures depending on the technique used. In addition to the precursor gas silane (SiH_4), hydrogen is usually added during the CVD growth in order to fill in the material defects and passivate the dangling bonds of a-Si, which form energy states leading to absorption in the IR region [18]. The resulting material, hydrogenated amorphous silicon (a-Si:H), has a refractive index around 3.48 depending on the hydrogen concentration and presents losses as low as 0.5 dB/cm at 1.55 µm for a large multimode waveguide [18]. For sub-micrometre single mode waveguides, propagation losses are usually around 3 dB/cm [68]. These losses are mainly caused by the rough surface of the PECVD deposited a-Si:H layer, which can generate a lot of scattering. To improve these losses, wet-etching and chemical mechanical polishing treatments have been introduced in the fabrication flow of sub-micrometre waveguides, resulting in propagation losses of 1.1 dB/cm and sub 1 dB/cm, respectively [69] [70].

In addition to passive waveguides, a-Si:H has also been used for active devices, such as modulators based on the thermooptic [71] or the plasma dispersion effect [72], and for nonlinear applications. With a nonlinear coefficient up to 5 times higher than c-Si [73], a-Si:H is often the material of choice for low-power, high speed nonlinear optical interactions [74]. Furthermore, with a-Si:H having a larger bandgap than c-Si, the two-photon nonlinear loss mechanism is largely reduced at telecommunication wavelengths [75]. However, the electron mobility in a-Si:H material, <100 $cm^2.V^{-1}.s^{-1}$ [76], is still too low for electrical applications and amorphous silicon has been shown to suffer from time degradation due to the Staebler-Wronski effect [23][24].

2.3.3 Crystalline silicon

As discussed in the introduction, crystalline silicon (c-Si) is an excellent material for both electronics and photonics applications with an electron mobility of ~ 1000 $cm^2.V^{-1}.s^{-1}$ [77] and low propagation

losses. The crystalline silicon transmission range covers the mid-IR region from 1.1 µm up to 7 µm as shown in Figure 2.3(a) and the absorption coefficient of intrinsic c-Si is plotted in Figure 2.3(b). In this material, all silicon atoms are periodically arranged as shown in Figure 2.2(c) and the refractive index is well-defined using the Sellmeier relation shown in Equation (2-18). At 1.55 µm, a-Si has a refractive index higher than c-Si ($n_{c-Si} = 3.45$ and $n_{a-Si} = 3.48$), but depending the deposition method, a-Si can have an even much higher refractive index [19].

Largely based on the SOI platform, optical propagation losses at telecommunication wavelengths in c-Si are situated around 0.3 dB/cm for large waveguides [78], whilst the sub-micrometre waveguides present higher losses between 1 and 2 dB/cm due to stronger interactions with waveguide surfaces [79][80]. In term of applications, c-Si is extensively used in the microelectronics industry but many progresses have been realised in photonics as well. In addition to signal modulation [79] and switching [80], [81], most of the nonlinear dynamics available in silicon at telecommunication wavelengths have been investigated in details since the first demonstration of Raman amplification in a silicon waveguide [81]. These include wavelength conversion [82], supercontinuum generation [83] and parametric light amplification [84]. However, as discussed in Chapter 1, the lack of deposition flexibility for c-Si makes the integration of both electronics and photonics on the same chip a challenging task.

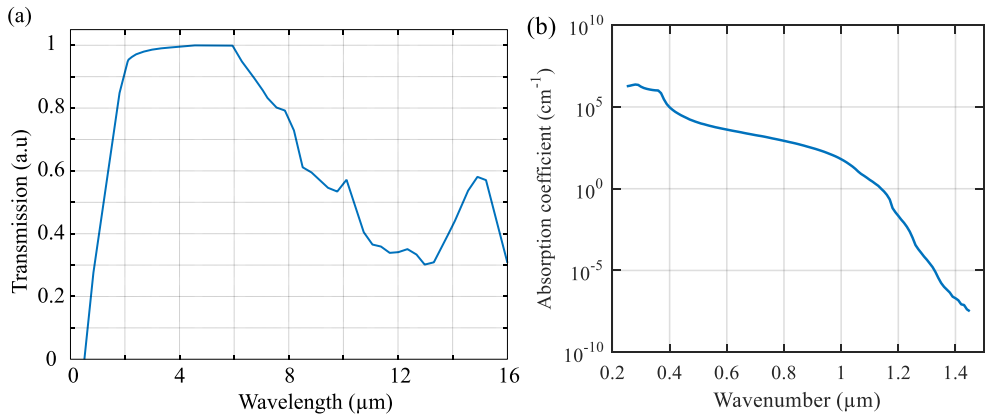

Figure 2.3: (a) Normalised transmission profiles for crystalline silicon from 1 to 16 µm, reproduced from [85]. (b) Log-scale absorption coefficient for crystalline silicon from 0.2 to 1.4 µm, reproduced from [86].

2.3.4 Polycrystalline silicon

Polycrystalline silicon (p-Si) is the core material of this thesis. Being a composite material, p-Si is a mixture of c-Si crystals surrounded by an amorphous matrix of silicon. Therefore, p-Si materials present both amorphous and crystalline properties with intensities being weighted by the amorphous/crystalline ratio. Usually, most of the p-Si material is crystallised and the amorphous silicon is situated at the crystal boundaries, which define a limitation between crystals. These crystal

boundaries are considered to be amorphous silicon because in these regions silicon atoms are disorganised with different atomic bond lengths and no periodic structure, as shown in Figure 2.2(b). Furthermore, these regions are filled with impurities, dangling bonds and crystal defects segregated during the crystal growth process. Therefore, crystal boundaries cause a lot of losses as these different defects form recombination sites for electron-hole pairs and scatter the optical signal.

For this thesis project, the objective is to deposit the silicon layer in its amorphous form using a CVD method and then to crystallise it into p-Si with the largest crystal grains in order to be as close as possible to the c-Si structure. In the remainder of this section, I'll present different techniques used to grow p-Si and the different results that have already been obtained along with their application fields.

2.3.4.1 Metal induced crystallisation

Metal induced crystallisation is a solid phase crystallisation technique which requires a low processing temperature due to the presence of a thin metallic layer in contact with the a-Si film. Different metals can be used with this method, including aluminium, nickel, silver, copper or gold [87]–[90]. Usually, a thin metallic film, ~50 nm, is deposited before or after the a-Si layer. During the heat process, the metal atoms diffuse into the silicon layer and ignite the nucleation of large crystals (tens of microns). Aluminium is largely used for metal induced crystallisation because it is low-cost and allows nucleation to happen at temperatures as low as 150 °C [91]. However, despite some work realised on thin film transistors [92], the resulting p-Si material quality is too low for photonics applications thus, metal induced crystallisation is preferably used for solar panel applications [93].

2.3.4.2 Furnace solid phase crystallisation

One of the most popular methods to obtain p-Si materials is via the thermal furnace solid phase crystallisation. The solid phase transformation of a metastable amorphous silicon material into a crystalline material requires activation energy, which is delivered through heat in this case. The crystallisation mechanism is not detailed in this thesis but explanations can be found in the literature [94]–[96]. Basically, when a-Si atoms receive enough energy, they rearrange themselves into crystalline clusters which are less strained. In the case of furnace crystallisation, the entire sample is heated and nucleation sites appear randomly in the entire film resulting in the formation of many crystalline silicon clusters. The large number of nucleation sites results in p-Si layers with small crystals, usually sub-micrometre.

Kwong et al. fabricated waveguides with amorphous silicon deposited by low pressure CVD at 550 °C and furnace processed with a first step of 40 h at 600 °C followed by second step of 5 h at 1000 °C. At the end of this process, waveguides with micrometric dimensions were found to have propagation losses of 0.56 dB/cm, while submicron waveguides had losses around 22 dB/cm [78].

Other sub-micrometre waveguides, furnace processed at 600 °C and then 1000 °C, have been demonstrated with losses of only 10 dB/cm [30]. The latest waveguides have been used for an all-optical modulator based on the plasma dispersion effect and a high speed electro-optic modulator Finally, Fang et al. demonstrated a sub-micrometre p-Si waveguide with losses of 6.45 dB/cm, but with no further investigation on crystal dimensions [97]. In addition to using high temperatures incompatible with our 450 °C thermal budget, the furnace crystallisation method only produces p-Si material with sub-micrometre crystal size, thus, in general, limiting the propagation losses >7 dB/cm [32]. In order to improve the optical quality of p-Si, larger crystals have to be grown.

2.3.4.3 Laser crystallisation

- **Excimer laser crystallisation**

Excimer lasers operate in a pulse regime in the ultra-violet domain of the electromagnetic spectrum. At these wavelengths, silicon is highly absorbing as shown in Figure 2.3(b), thus excimer lasers are an efficient way of heating silicon material. As opposed to furnace crystallisation where the entire silicon film is heated, only the exposed area is heated with laser crystallisation. Furthermore, in the case of laser crystallisation, the a-Si material is usually heated up at temperatures higher than 1414 °C, silicon melting temperature, whilst the energy transferred to the substrate is negligible [98].

Depending on the quantity of energy transferred to the silicon, different crystallisation regimes can be observed [22], [99], [100]:

- In the partial-melting regime, silicon does not receive enough energy and the silicon layer is partially melted. The molten silicon crystallises into small crystals surrounded by a-Si. This crystallisation process is also called explosive crystallisation.
- In the near-complete-melting regime, the entire volume exposed to laser radiations is melted except for few crystallites which act as nucleation sites. The crystallisation ignited by the remaining crystallites, also called super lateral growth, takes place before spontaneous nucleation sites appear therefore resulting in the formation of few large crystals.
- In the complete-melting regime, the entire volume exposed to laser radiation is melted and many random spontaneous nucleation sites can appear, typically resulting in the formation of many crystals with small sizes.

Sometimes, both small and large crystals can be observed in a laser crystallised structure. This phenomenon is described in Figure 2.4.

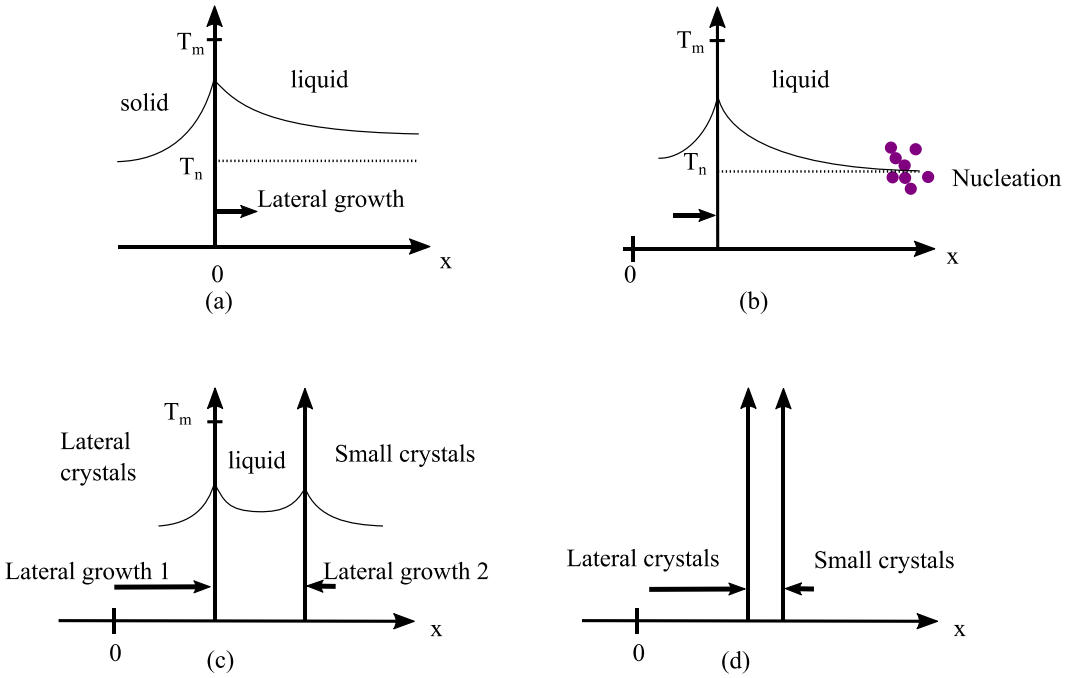

Figure 2.4: Schematics representing a simplified one-dimensional temperature distribution during the evolution of the crystal growth process. Reproduced from [101].

In Figure 2.4(a), after the pulse absorption, the exposed area is in a liquid super-cooled state below the melting point T_m whilst the unexposed solid silicon acts as a nucleation site and ignites lateral growth. In Figure 2.4(b), the super-cooled liquid silicon reaches the nucleation temperature T_n and crystallites start to form. This process being exothermic, the latent heat raises the temperature of the super-cooled liquid now sandwiched between two solid phases, as shown in Figure 2.4(c). At the end of the process, large crystals formed by the lateral growth can be observed next to small crystals originating from the random spontaneous nucleation as show in Figure 2.4(d).

Excimer lasers can also be used in sequential laser crystallisation with the exposed spot being seeded by the previous spot. By scanning the area with this method, crystals up to 200 µm long have been reported, but this method has not been studied further for optical applications [102]. Despite the use of excimer laser crystallisation for the fabrication of thin film transistors with electron mobility up to several hundreds of $cm^2.V^{-1}.s^{-1}$ [103][22], the p-Si material processed by this technique is still quite lossy with propagation losses as high as 20 dB/cm [38][104]. This is a consequence of the excimer laser short cooling time associated with the pulse duration, which results in micrometre large crystals or less.

❖ Continuous wavelength laser crystallisation

Despite sharing many common dynamics with the excimer laser crystallisation, continuous wave (CW) laser crystallisation (CLC) differs mainly by its temperature gradient [22], [105]. When scanned over the silicon film as shown in Figure 2.5, the usually Gaussian profile beam transfers less

energy to the wings of the exposed areas, resulting in a partial-melting regime for these regions whilst the central part is totally melted. When cooling down, many nucleation sites spontaneously appear forming many small crystals which seed the lateral growth at the origin of the large crystals observed in the central part of the track. Also, because of the scanning movement, crystals are dragged toward the right as the material temperature is higher toward the melting front represented by the laser spot. By finely tuning the laser spot dimension, its scanning speed and its intensity, it is expected that very large crystals can be obtained with only large laterally grown crystals over the entire scanned area.

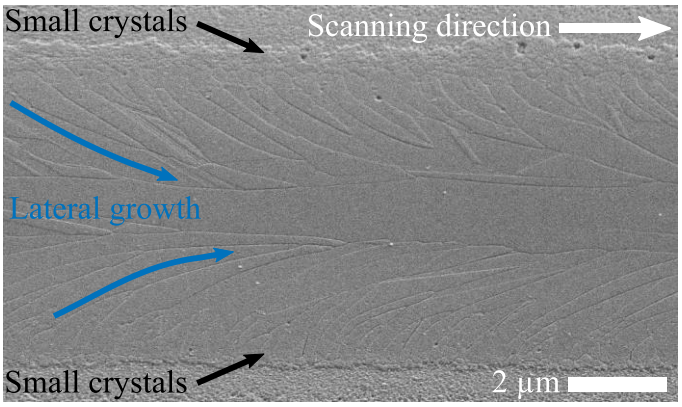

Figure 2.5: Micrograph of an a-Si film laser crystallised by a CW laser with a Gaussian beam profile.

However, one of the drawbacks of the CLC approach is the processing time. Whilst excimer laser crystallisation only requires only few tens of nanoseconds for exposure, CLC takes longer, few milliseconds, resulting in smoother and longer crystals, but at the cost of time. This technical point, that has to be investigated for wafer-scale integration, is not discussed in this project, but other groups have reported CLC at scanning speeds up to 200 cm/s with a 400×20 μm^2 laser spot [106].

For CLC, argon gas lasers emitting in the range of 488-520 nm or solid state lasers emitting at 532 nm with several watts of output are usually used. Several groups have investigated the crystallisation effect of a flat laser beam profile on an a-Si film patterned into stripes of different widths [107], [108]. Whilst this work was performed for solar panel and thin film transistor applications [109], [110], large crystals, several microns long, have been demonstrated with a thermal budget of 450 ^oC and electron mobility up to 566 $cm^2.V^{-1}.s^{-1}$, which indicates a high material quality. As yet, not a lot of work has been reported on CLC for photonics applications, except for the crystallisation of an a-Si core fibre, where crystals up to 200 µm long have been observed [44]. The main purpose of this project is to explore the different possibilities available with this method, investigate how large the crystal grains can be grown, and measure the material and optical properties of p-Si material obtained by CLC.

Chapter 3

Waveguide fabrication and characterisation

3.1 Introduction

In this work, the sample fabrication and subsequent processing steps are critical, and depend on the final application targeted. For planar geometry devices, the growth and processing temperatures are key to CMOS compatibility, whilst for silicon core fibres samples, the temperature is not a limitation factor, but large grain growth is because the fibre length is very long. In this chapter, the preparation steps for the different samples that have been used in this research project are presented, together with the various material analysis methods. For the fabrication of the silicon planar samples, the choice of substrate is discussed and a detailed presentation of the two chemical vapour deposition (CVD) techniques used to deposit the silicon materials (plasma-enhanced CVD (PECVD) and hot-wire CVD (HWCVD)) is given along with the patterning methods that are required for the fabrication of waveguides. The fabrication process of the MCD silicon core fibres used for this thesis is also presented. Finally, the different tools used to characterise the material and optical properties of the materials and devices: Raman spectroscopy, X-ray diffraction (XRD) and optical transmission measurements, are described in detail.

3.2 Planar waveguide fabrication

As the key goal of this part of the project is to remove the substrate constraints from silicon photonics, our work considers two different substrates so that a comparison can be drawn. Plain fused silica is presented first as this platform was initially used to validate the crystallisation technique presented in this thesis owing to is ready availability and low-cost. Then, silica-on-silicon wafers are introduced as these are more compatible with the HWCVD deposition method.

3.2.1 Plasma-enhanced chemical vapour deposition (PECVD)

As an initial proof of concept, we first deposited silicon films on 1 mm thick fused silica substrates. This inexpensive material allowed us to run several experiments with both hydrogenated and non-hydrogenated silicon films with the results summarised in Chapter 4. These films were deposited in a PECVD reactor schematised in Figure 3.1 using the recipe presented in Table 3-1. Starting with an argon plasma generated by a radio frequency (RF) source, both precursors, silane (SiH_4) and dihydrogen (H_2), are then injected in a pressurised chamber where hot plasma electrons separate silane and dihydrogen molecules into radicals and ions [111]. With the sample substrate being on the grounded electrode, ions are attracted toward the sample and a silicon film grows in an amorphous state as the temperature is not high enough to obtain polycrystalline silicon.

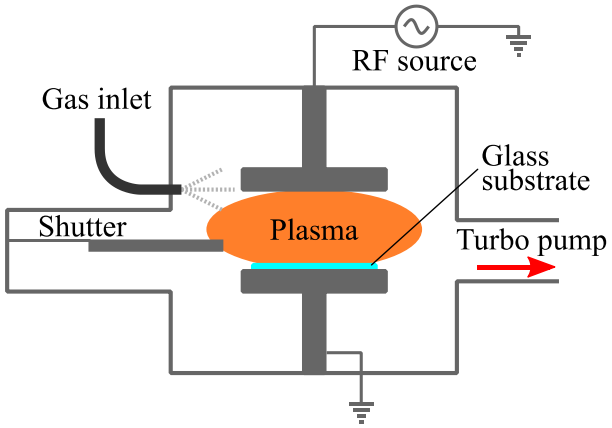

Figure 3.1: Schematic diagram of a parallel plate PECVD reactor. The process gases are injected via the gas inlet. The substrate is mounted on the lower electrode which is heated at 200 °C.

Temperature (°C)	200
Pressure (mTorr)	300
SiH_4 Flow (sccm)	50
H_2 Flow (sccm)	50
RF (W)	10
Deposition Rate (nm/s)	0.28

Table 3-1: Recipe used for the deposition of a-Si:H using a PECVD reactor.

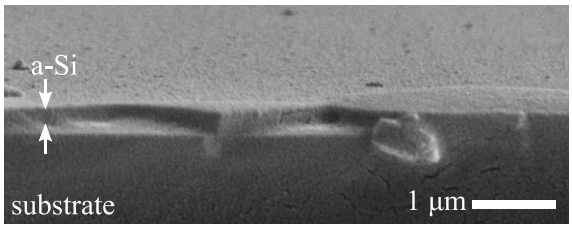

Figure 3.2: SEM micrograph of a fused silica substrate sample with a 250 nm thick PECVD deposited a-Si:H film.

Silicon films deposited by PECVD, 250 nm thick, can be seen in Figure 3.2 where the a-Si:H film, which partially lifted-off during the cleaving process, can be measured. Debris visible on the micrograph came from the cleaving, which does not result in a sharp edge for amorphous material like a-Si and fused silica. Furthermore, the roughness of the PECVD deposited material has been measured using an interferometric optical profiler system from Zemetrics. Using Mirau objectives, interference fringes are produced on sample's surface and their dephasing gives information about surface topography. The 3D map of a large 10 µm wide wire patterned into an a-Si film deposited by PECVD, and serving as a planar reference, is shown in Figure 3.3(a). A section of this wire surface has been selected for the roughness measurement, as seen in Figure 3.3(b). With this system, the root mean square (RMS) roughness of a-Si:H film deposited by PECVD was found to be ~2.1 nm.

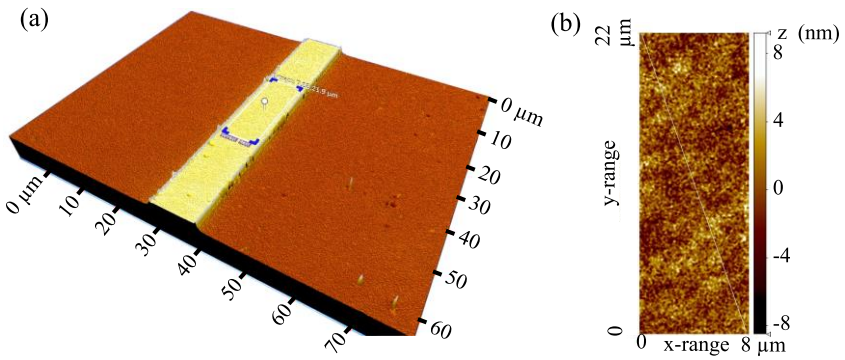

Figure 3.3: (a) 3D ZeScope map of a patterned a-Si:H film deposited on glass substrate by PECVD. (b) Surface variation of the area selected in (a) to determine the surface roughness.

In the recipe presented in Table 3-1, dihydrogen is used to prevent the formation of dangling bonds corresponding to unsatisfied valence of silicon atoms, during the deposition [112]. If left untreated, these dangling bonds would be responsible for scattering losses in silicon waveguides hence hydrogen is introduced in order to fill these voids and give access to low-loss hydrogenated amorphous silicon material [18]. However, hydrogen will out-diffuse at temperatures ~400 °C [113], which can cause problems during the laser processing as reported in Chapter 4. To reduce the amount of hydrogen present in the as-deposited material, a thermal annealing treatment was performed at

450 ºC for 1 hour with 5 ºC/min ramps. This thermal annealing process allowed for hydrogen to gently out-diffuse without damaging the silicon film structure, or forming polycrystalline silicon. Using the interferometric optical profiler system, the a-Si film roughness after thermal annealing is ~2.40 nm, which is slightly higher than the as-grown films. This difference is believed to be due to the gas out-diffusion.

At the end of this process, both a-Si:H and a-Si samples deposited by PECVD are available for experiments presented in Chapter 4 and Chapter 5.

3.2.2 Hot-wire chemical vapour deposition (HWCVD)

After a set of preliminary experiments conducted on the glass-based samples, we decided to move toward a platform closer to foundry standards and opted for crystalline silicon wafers with an oxide layer on top of it to act as the low index cladding. As discussed in Chapter 1, the standard BOX thickness in electronics of 200 nm differs from the photonics standard of 1 µm [114]. In our fabrication flow, we use oxide layers which are 2 to 4 µm thick to ensure optical isolation and ease our free-space coupling injection.

For our silicon wafer substrate, the oxide layer was grown by wet thermal oxidation [115]. Silicon wafers were placed in a tube furnace tube at 800 ºC for 100 hours in the presence of water vapour, whose molecules penetrate the material to form silica. Contrary to CVD techniques, thermal oxides are of higher quality as they contain less impurities and have a higher density, but they suffer from their slow growing rate and high processing temperatures [116][117]. However, the differences in the optical properties of a silica films obtained by either thermal oxidation or CVD are negligible when used as BOX or cladding layer.

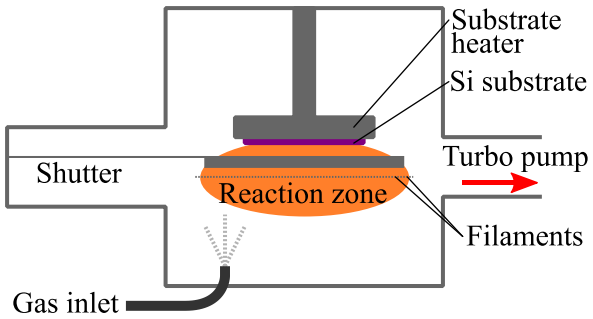

Figure 3.4: Schematic diagram of a HWCVD reactor. The substrate is located on the upper electrode which is heated at 335 °C.

Temperature (ºC)	335
Pressure (mTorr)	7.5
SiH_4 Flow (sccm)	40
H_2 Flow (sccm)	0
Deposition Rate (nm/s)	0.69

Table 3-2: Recipe used for the deposition of a-Si using a HWCVD reactor.

Once the BOX layer was grown, the amorphous silicon deposition was performed in a HWCVD reactor, shown in the schematic of Figure 3.4, using the recipe presented in Table 3-2. In the case of

HWCVD, a gas mixture of silane and molecular hydrogen is also used but decomposition of the molecules is achieved by hot tungsten wires. When the silane comes in contact with the wires, which are heated at 1400-1600 ^{o}C, it decomposes into Si and H. At this temperature, Si evaporates onto the substrate placed few centimetres away from the hot wire [118], [119]. By adjusting the gas pressure and deposition temperature, silicon films with low hydrogen content can be obtained with HWCVD, thus removing the need for the furnace annealing step used with PECVD depositions [120]. It should be noted that in order to control the deposition temperature in HWCVD, the sample is deliberately cooled down via the sample mount. Thus, thermally conductive substrates such as crystalline silicon are better suited for HWCVD than glass substrates that would need to be mounted onto another conductive substrate.

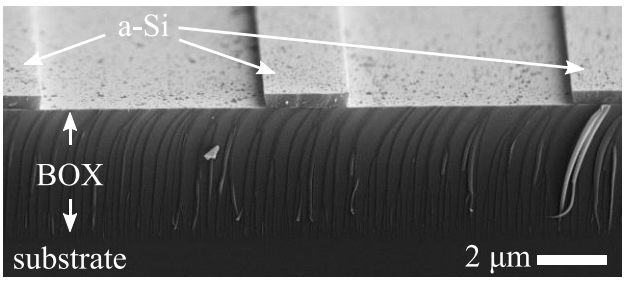

Figure 3.5: SEM micrograph of a 400 nm thick patterned a-Si film deposited by HWCVD on a crystalline silicon substrate with a 4 µm thick BOX layer.

Figure 3.5 shows the cross-section of a 400 nm thick a-Si film deposited by HWCVD on a crystalline silicon substrate with a 4 µm thick BOX layer. This film has already been patterned and the three layers of the sample can be clearly identified. The rippled area corresponds the BOX layer which is amorphous and does not result in a clean cut after cleaving. The debris visible on the micrograph are mainly due to the cleaving process. The interferometric surface profiler system has also been used to measure the film roughness as shown in Figure 3.6. For HWCVD film, the roughness is ~0.25 nm, which is significantly smoother than PECVD films. Atomic force microscope measurements of these films that have been performed by another group showed a roughness of 0.5 – 0.8 nm. Despite the small difference between the two individual measurements, these films still have a sub-nanometre roughness which should reduce scattering losses in waveguide transmission.

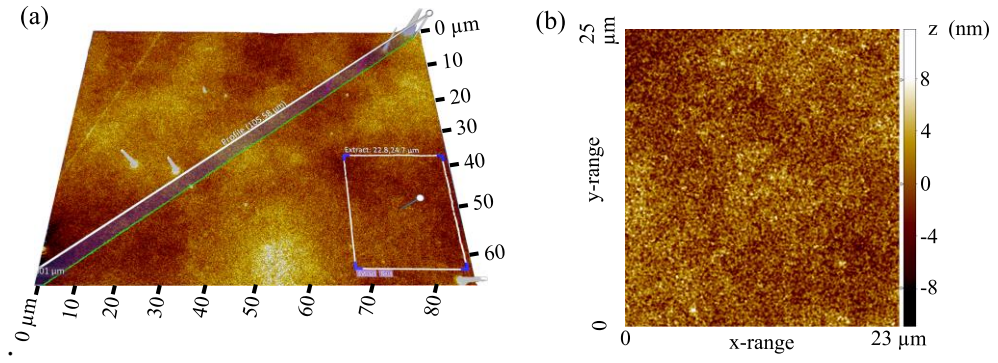

Figure 3.6: (a) 3D ZeScope map of a patterned a-Si film deposited on a BOX layer by HWCVD. (b) Surface variation of the area selected in (a) to determine the surface roughness.

3.2.3 Patterning

To facilitate the formation of optical circuits we produced patterned structures. In addition to the confinement of the optical mode both vertically and horizontally, the patterning of silicon films, prior to laser treatment, improves the quality of crystallisation with a better heat confinement during the laser processing step. With the planar silicon films, the heat energy is only confined vertically and the heat affected area is defined by the laser spot size and the diffusion of heat through the layer as illustrated schematically in Figure 3.7(a). Only a small amount of heat is transferred to the substrate as the thermal conductivity of silica glass is 0.5 W/m/K [121], compared to 1.1 W/m/K for amorphous silicon [122]. Once patterned, the heat is strongly confined in the wire, which is surrounded by low thermal conductivity material (air with 0.025 W/m/K [123]) as shown in Figure 3.7(b). Also, the reduced volume of silicon is expected to lower the quantity of spontaneous crystallisation sites that occur during the laser crystallisation process.

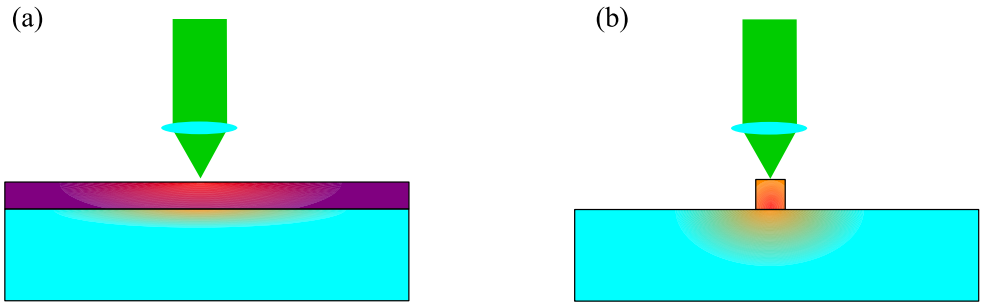

Figure 3.7: Heat distribution schematics for laser processing onto planar (a) and patterned (b) samples.

For the fabrication of wire waveguides, two different methods have been used: photolithography, which is relatively low cost and suitable for large scale patterning, but with a limited resolution, and e-beam lithography, which is suitable for complex designs and is a high resolutions patterning method.

3.2.3.1 Photolithography

The steps that are required to photolithographically pattern our silicon films are illustrated in Figure 3.8. After being cleaned and dried in a furnace at 90 °C to increase the photoresist adhesion, a layer of SU1813 photoresist is spun onto the entire surface of the sample at 300 rpm for 3 s to remove the photoresist excess, followed by a 50 s step at 5000 rpm to achieve the desired thickness (Figure 3.8(b)). The sample is then hardbaked for 30 minutes at 90 °C in an oven. Then, the harden waveguides patterns are transferred to the photoresist using a mask aligner system and a 112 mJ dose of UV radiations (Figure 3.8(c)). Because we used a positive photoresist, the exposed parts are removed by dipping the sample for 50 s in a development solution, MF-319 (Figure 3.8(d)). At the end of this process, only photoresist wires that will protect the silicon film during the etching step remain as shown in Figure 3.8(e).

The final etching step, common to both photolithography and e-beam lithography, is detailed below in Section 3.2.3.3.

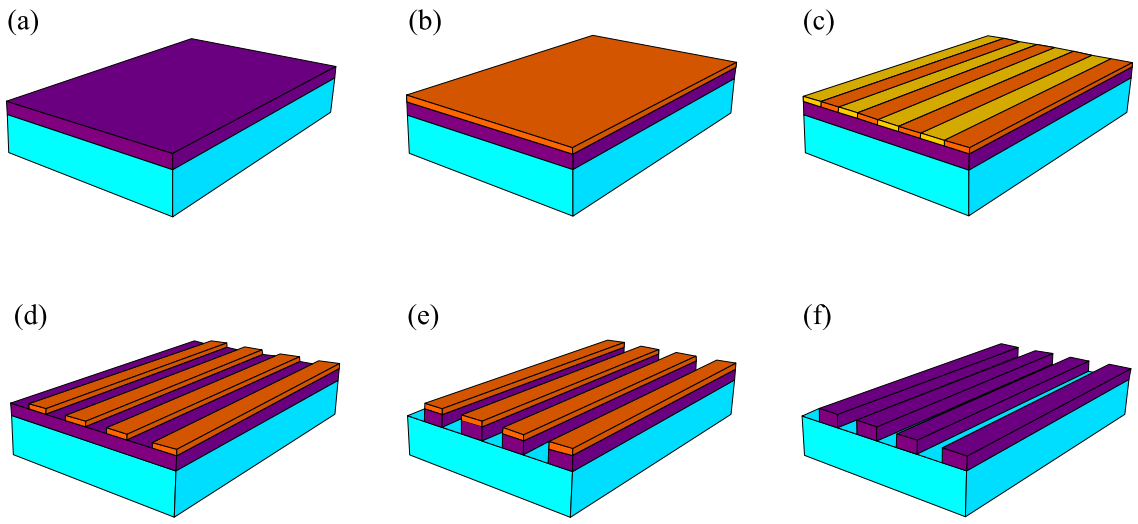

Figure 3.8: Photolithography steps. (a) dry cleaning, (b) photoresist deposition, (c) partial UV exposure with a mask, (d) removal of exposed parts by dipping the sample in a development solution, (e) etching of the entire sample and (f) removal of protective photoresist wires.

3.2.3.2 E-beam lithography

In order to have waveguides produced with high-precision patterning during the development stages of our processing technique, the silicon films have also been patterned using e-beam lithography. As with photolithography, a sensitive resist, in this case a positive tone ZEP made for SEM use, is spun at 3600 rpm on top of the film to pattern. After 180 s of pre-baking at 180°C, the sample is locally exposed by the electron beam of a SEM with a 190 J/cm^2 dose before being dipped for 100 s in a development solution, ZED-50 [124]. The main advantage of e-beam lithography is the use of a SEM to transfer the mask to the resist film. This transfer method allows us to modify the waveguide design

without ordering a new mask and also gives access to features as small as 500 nm, compared to photolithography where the smallest repeatable features were of the order of 1.5 µm with the equipment at our disposal. However, it is worth noting that high-precision photolithography systems can reach the 500 nm scale, so that in future this could be used for large scale fabrication of the optimized waveguides.

3.2.3.3 Etching

Amorphous silicon materials can be etched through two different techniques: i) wet etching, with liquid-based etchants and ii) plasma-based dry etching. Whilst wet etching is appreciated for its simplicity of equipment, dry etching is mostly preferred in the semiconductor industry as its anisotropic etch results in smooth and vertical sidewall profiles [125].

For this project, we initially used a reactive ion etching (RIE) system to pattern our silicon films using the recipe shown in Table 3-3. The principle of RIE is similar to a PECVD system where a plasma is generated between two electrode plates with the sample being placed on a powered plate. Using a high voltage difference between the two plates, ions are strongly accelerated and hit the sample surface with high velocity knocking off both the exposed silicon and the top surface of the protective photoresist wires [126]. In addition to this physical ion bombardment, chemical reactions also occur at the surface of the sample depending on the used gases. Some halogen-based gases, such as sulfur hexafluoride (SF_6), are specifically used to react with silicon, whilst other gases such as octofluorocyclobutane (C_4F_8) are used to passivate and protect the walls from lateral etching by forming a polymer film [127].

O_2 Flow (sccm)	12
SF_6 Flow (sccm)	12
Pressure (Torr)	30
Power (W)	100
Etch Rate (nm/s)	≈ 5.4

Table 3-3: RIE recipe for a-Si based on O_2/SF_6.

C_4F_8 Flow (sccm)	39
SF_6 Flow (sccm)	25
Pressure (Torr)	30
Power (W)	750
Etch Rate (nm/s)	≈ 7.5

Table 3-4: ICP-RIE recipe for a-Si based on C_4F_8/SF_6.

Later in the project, we also used an inductively coupled plasma reactive ion etching (ICP-RIE) system which consists of a RIE system with a plasma generated by a RF coil. The advantage of this system is that ion bombardment and plasma generation are decoupled and can be controlled individually. The recipe used with this system is presented in Table 3-4 and employed C_4F_8 gas, which resulted in improved wall definition as shown in the micrographs of Figure 3.9. The a-Si wire on Figure 3.9(b) has been patterned using photolithography and RIE etching whilst the a-Si wire shown in Figure 3.9(b) has been patterned using e-beam and ICP-RIE. Despite the mask deposition

techniques being different, the wavy pattern on the left side of the wire in Figure 3.9(a) is associated to photolithography issues and not to RIE etching. However, the presence of C_4F_8 in the ICP-RIE does result in more sharply defined walls.

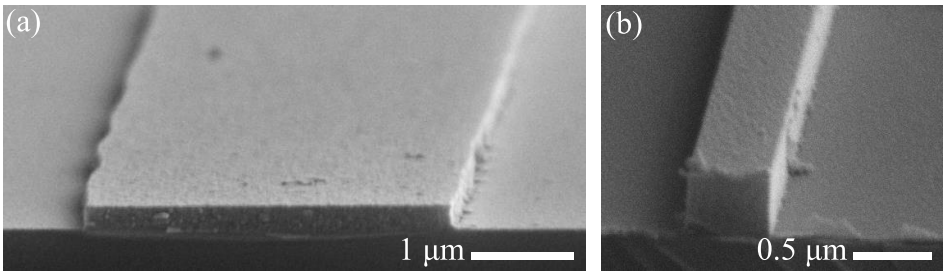

Figure 3.9: SEM micrographs of a-Si wires produced by (a) photolithography/RIE and (b) e-beam lithography/ICP-RIE (b).

During this project, we encountered an etching problem whilst using RIE system. After finely tuning our etching recipe for 200 nm thick a-Si with small dummy samples, we positioned our full size sample within the reactor for etching and ended up with an under-etched film as shown in Figure 3.10. It was later understood that because of the chemical reactions that occur during the RIE process, larger areas of materials require a longer etching time. Therefore, the etching time must be adapted to the sample size, under-etching can be observed with a profilometer as shown in Figure 3.10 where a-Si wires are 80 nm high instead of 200 nm.

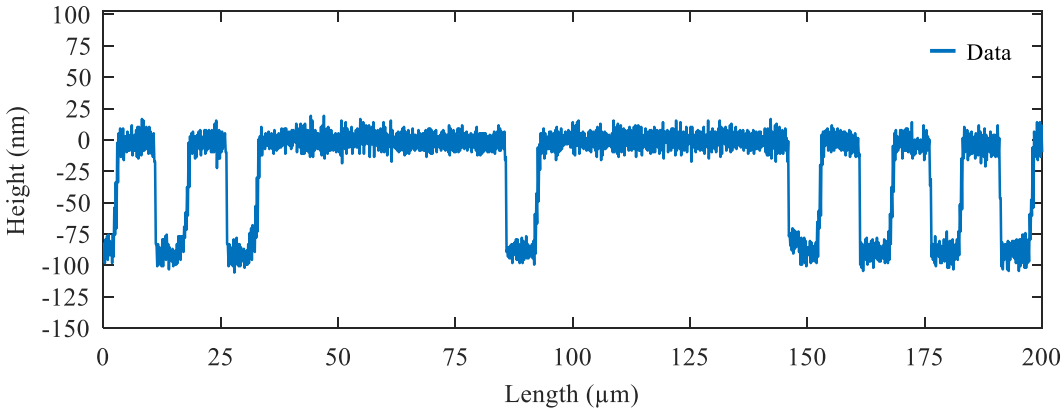

Figure 3.10: Stylus profilometer trace of a HWCVD under-etched sample (80 nm height instead 200 nm).

Once the recipe was adjusted to the sample size, the expected 200 nm high structures can be observed as shown with profilometer trace in Figure 3.11.

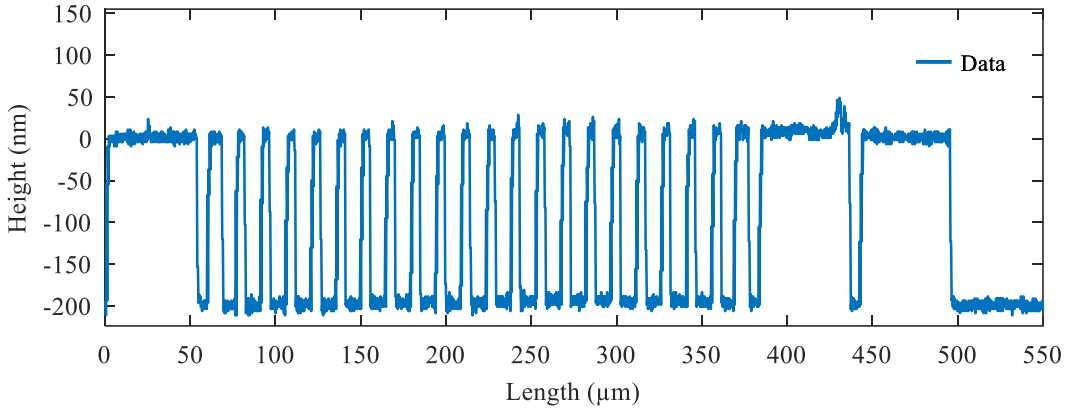

Figure 3.11: Stylus profilometer trace of a HWCVD patterned samples with an adjusted recipe.

3.3 Silicon core fibre fabrication

In addition to planar geometry silicon waveguides, this project also explores silicon core fibres as their geometry makes them easily integrable in all-fiberised systems, whilst their silicon core gives access to nonlinear dynamics that can be used for different applications such as all-optical modulation [128]. Today, there are two main fabrication approaches to produce silicon fibres: i) via chemical deposition inside a glass capillary template [39], [43], [129], and ii) via a drawing tower starting from a preform containing the silicon encapsulated in a silica cladding[42]. However, because this thesis is focused on p-Si material, molten core drawn fibres are the best candidates as they have better material quality and can be drawn up to several meters long.

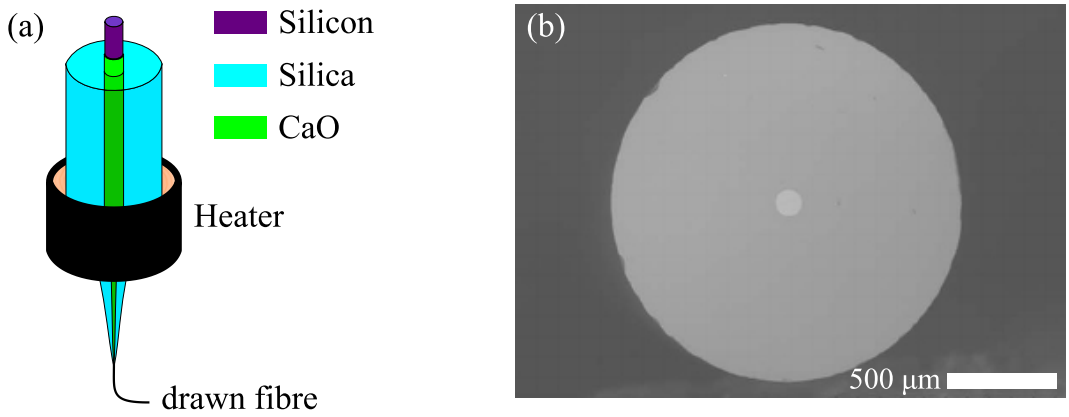

Figure 3.12: (a) Fibre drawing tower schematic for MCD method, (b) Scanning electron micrograph of a 100 µm core diameter silicon core, silica-clad optical fibre obtained via the MCD method (from [130]).

Originating from the standard fibre drawing technique, the MCD fabrication consists of melting a rod of silicon that is sleeved within a thick silica cladding, which ultimately acts as a crucible to contain the liquid core, as illustrated in in Figure 3.12(a). Pioneered in 2008 for silicon core fibres [42], this technique is similar to the powder-in-tube process, where the core material is reduced to powder in a silica capsule before being drawn in a fibre tower [131]. Alkaline compounds, such as calcium oxide (CaO) shown in Figure 3.12(a), are commonly used to stop the oxygen diffusion at the core/cladding interface and reduce the thermal material mismatch during the high temperature process required to melt the core [48]. In contrast with the chemical deposition technique, the high temperatures used in the MCD process does not allow the production of fibres with amorphous core materials, and the hydrogen content in the core is very low as it out-diffuses during the drawing process. Due to the Plateau-Rayleigh instabilities appearing in the molten phase for micron-size cores geometries [132], large cores are favoured with this method as shown in Figure 3.12(b), which makes them unsuitable for nonlinear applications. In our project, fibres produced with this method had a core diameter typically around 9 µm. However, despite these drawbacks, the primary advantage of this method is the possibility of drawing long lengths, several tens to hundreds of metres, of fibre using a traditional drawing tower [41].

3.4 Material characterisation

The laser processed materials have been extensively characterized using optical microscopy, scanning electron microscopy (SEM), Raman spectroscopy and X-ray diffraction. Whilst the results of optical microscopy and SEM are straightforward to analyse, Raman spectroscopy and X-ray diffraction require an understanding of their principle in order to extract information from their results.

3.4.1 Raman spectroscopy

The Raman spectrometer is a tool that has been used extensively in this project for its capability to provide evidence for the degree of crystallisation of our silicon material and detecting the presence of elements such as hydrogen, whilst being non-destructive, contactless and fast. Raman spectroscopy consists of analysing the Raman scattered photons produced by the inelastic interaction of incident photons with vibrations or phonons in the material lattice. The phenomenon underlying Raman spectroscopy is the transition of a molecule from a ground state (M) to a vibrational state (M*) and the reverse mechanism from M* to M. However, the photons involved in Raman scattering are not absorbed or emitted in the process, but rather shifted by the amount of energy corresponding to the molecular transition. In the Stokes mechanism, the scattered photons are shifted toward lower frequencies as the molecules absorb energy from the incident photons, whilst in the anti-Stokes mechanism, scattered photons are shifted toward higher frequencies as they collect the energy

released by the molecules during their relaxation [133]. Both mechanisms can be summarised as follows:

$$\textbf{Stokes: } M + h\nu_0 \rightarrow M^* + h(\nu_0 - \nu_v) \,, \tag{3-1}$$

$$\textbf{Anti-Stokes: } M^* + h\nu_0 \rightarrow M + h(\nu_0 + \nu_v) \,, \tag{3-2}$$

where h is Planck's constant, ν_0 is the incident photon frequency and ν_v is the vibrational frequency. Also, in Raman spectroscopy, vibrational frequencies are referred to by their wavenumber: $\bar{\nu} = \nu/c$, expressed in cm^{-1}, with c the speed of light and ν in s^{-1}.

In crystalline silicon, where Si atoms are arranged in a tetrahedral (diamond) lattice, as shown in Figure 3.17(a), only one vibration, which corresponds to a transverse optical mode of c-Si, can be observed within our spectrometer range (100 – 2400 cm^{-1}). This vibration between Si atoms results in the appearance of a single Raman peak with a Lorentzian line-shape centred at 520 cm^{-1} and a natural linewidth Γ corresponding to the vibration phonon lifetime. Because of the sensitivity of τ to impurities and temperatures, different values of Γ have been published [134][135][44]. In this thesis, for c-Si we will assume the Lorentzian full width at half maximum (FWHM) $\Gamma = 2.7$ cm^{-1} [44].

In practice, the acquired Raman peak of c-Si, as shown Figure 3.13, is a combination of two peaks: a Lorentzian peak, the intrinsic response of c-Si, and a Gaussian peak which is an instrument transfer function representing the peak broadening induced by the spectrometer [136]. Therefore, to extract the information about the material under study, the Lorentzian part of the peak has to be identified. To do so, the peak data is fitted using a Voigt function which is the convolution of a Gaussian peak and a Lorentzian peak and is defined as [137]:

$$\text{Voigt}(x, \sigma, \gamma) = \int_{-\infty}^{+\infty} G(t, \sigma) L(x - t, \gamma) dt = \frac{\text{Re}[w(z)]}{\sigma\sqrt{2}} \,, \tag{3-3}$$

with x the wavenumber shift, σ the Gaussian width related to the FWHM width by $\text{FWHM} = 2\sqrt{2\ln(2)}\sigma$, $\gamma = \Gamma/2$ the Lorentzian half width at half maximum (HWHM) and Re[w(z)] the real part of Faddeeva function, defined by $w(z) = e^{-z^2}\text{erfc}(-iz)$, evaluated for $z = (x + i\gamma)/(\sigma\sqrt{2})$ [138].

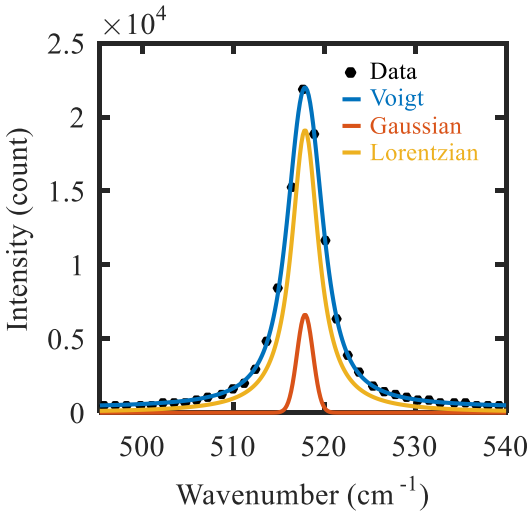

Figure 3.13: Raman spectrum of crystalline silicon. Data are fitted with a Voigt function (blue) which is the convolution of a Gaussian (red) and a Lorentzian (orange) distribution.

Experimentally, to evaluate the Lorentzian width we always perform two acquisitions: one from the sample and one from a c-Si reference. From the c-Si reference acquisition we know that: $\Gamma = 2.7$ cm^{-1}, so by using the best Voigt fitting to this sample, the Gaussian contribution is extracted. Once known, the Lorentzian contribution of the p-Si sample under measurement is determined from the best Voigt fit when applying the Gaussian contribution, as calculated by the reference measurement. For each Raman session, a new c-Si reference was taken as the Gaussian peak includes the environment variations. Once the Lorentzian contribution is determined, two parameters are used to characterise the silicon sample under study: the width (Γ) and the position of the peak.

The width of the peak is indicative of the degree of crystallisation of silicon [139]. In pure crystalline silicon material, the phonon lifetime is at its maximum so the peak width is at its smallest value: $\Gamma = 2.7$ cm^{-1}. However, in polycrystalline silicon, the presence of crystal boundaries reduces the phonon lifetime resulting in broadening of the peak width. Therefore, as shown in Figure 3.14(a), the p-Si peak, plotted in red, is broader than the c-Si peak, plotted in blue.

The position of the peak is indicative of the degree of crystallisation of silicon and the material strain, both of which are related to the Si-Si bond length. When silicon crystals are formed, the average length between the four fold coordinated Si atoms decreases when the crystal size increases [140]. This variation of the atomic bond length induces a variation of the molecular vibrational energy resulting in different Stokes and anti-Stokes shifts represented by the peak position. For this reason, two crystallisation regimes have been added to the c-Si peak centred around 520 cm^{-1} as shown in Figure 3.14(b): the nano-crystalline (nc-Si) peak, centred around 504 cm^{-1}, and the micro-crystalline silicon (µc-Si) peak, centred at 515 cm^{-1} [141]–[143].

In the case of polycrystalline silicon, these different peaks, combined with the amorphous silicon present between crystals, introduce different vibrational energies that form the tail of the asymmetric p-Si peak shown in the red spectrum of Figure 3.14(a). The Raman peak position can also be affected by tensile or compressive strain present in the material under study. In the case of a compressive stress, the bonds between the silicon atoms are shorter and the peak position is shifted toward higher frequencies, whilst a tensile stress elongates the bonds resulting is a shift toward lower frequencies [144]. Using Hooke's law, the strain of the material can be calculated from the peak shift as long as the crystal orientation and the strain direction are known [145].

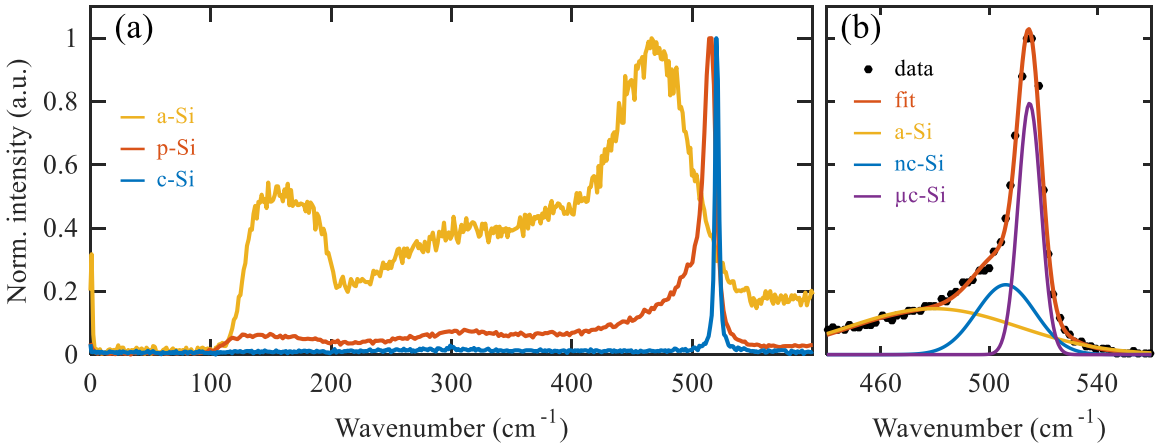

Figure 3.14: (a) Raman spectra of silicon with different degrees of crystallisation: a-Si in orange, p-Si in red and c-Si in blue, (b) Raman spectrum of a p-Si peak fitted with a-Si, nc-Si and µc-Si peaks.

Finally, Raman spectroscopy can be used to reveal the presence of amorphous silicon and hydrogen as shown in Figure 3.15. For a-Si, there are three peaks corresponding to three different vibration modes: a longitudinal acoustic (LA) centred at 311 cm^{-1}, generated by Si-Si rocking vibrations and two optical modes, a longitudinal optical (LO) centred at 418 cm^{-1} and a transverse optical (TO) centred at 480 cm^{-1}, generated by a collective stretching motion of the Si atoms [146]. These peaks are broader than the p-Si or c-Si peaks because of the disorganisation of Si atoms in the amorphous phase, resulting in shorter phonon lifetimes along with a larger variety of vibrations with different energies. Because we will not perform any quantitative work on these peaks, simple Gaussian fittings are used.

Also shown in Figure 3.15 are Raman peaks corresponding to the presence of hydrogen in the silicon film. The first one, centred at 613 cm^{-1}, is generated by wagging vibrations of Si–H bonds [147]. The second is positioned further in the spectrum and is a combination of two peaks generated by the stretching of Si-H and Si-H_2 bonds centred at 1992 cm^{-1} and 2086 cm^{-1}, respectively [148].

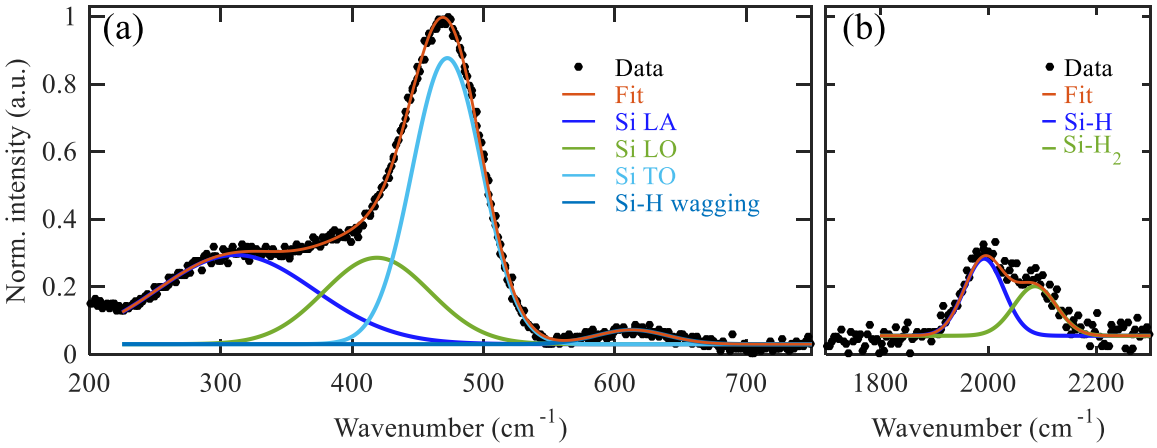

Figure 3.15: Raman spectrum of an a-Si:H film. (a) First segment of the spectrum with the acoustic mode (LA) and the two optical modes (LO+TO) of Si-Si along with the Si:H wagging mode, (b) second part of the spectrum with the Si-H and Si-H_2 stretching modes.

Raman spectra presented in this thesis have been obtained using a "Renishaw" system coupled to a 532 nm excitation laser. At this excitation wavelength, the penetration depth in silicon, measured from the absorption coefficient in Figure 2.3(b), is slightly deeper than 1 µm, which ensures the entire material thickness will be sampled. A ×50 objective was used to focus the laser beam and collect the Raman photons. The focussed spot diameter was 1 µm and the diffraction grating used had 2400 lines/mm, having a precision of 0.12 cm^{-1}.

3.4.2 X-Ray Diffraction

Another tool that we regularly used to characterise our samples is X-ray diffraction, which provides information about the number of crystals present in our samples along with their crystallographic plane. One of the benefits of X-ray diffraction is that each crystal can be analysed individually, which is not the case with Raman spectroscopy. XRD is a technique that characterises crystalline materials by sending a collimated X-ray beam on a sample and detecting the diffracted beams. X-ray beams have a wavelength of the order of the atomic bonds, ~10^{-10} m, so that the periodic atomic pattern present in the crystalline material acts as a grating. Constructive interference appears when the Bragg condition is satisfied [149]:

$$n\lambda = 2\,d\sin(\theta)\,, \tag{3-4}$$

with n an integer, λ the wavelength, d , also called d-space, is the interlayer spacing, i.e., the distance between atomic layers, and θ the incident angle between the input beam and the layer surface. In

Figure 3.16, two beams satisfying Bragg's law are represented along with black dots representing atoms, the interlayer spacing d and 2θ, twice the incident angle, corresponding to the angle between the non-diffracted beam and a diffracted beam.

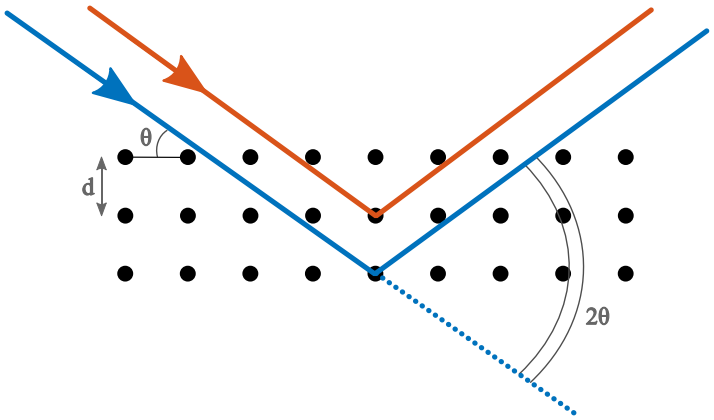

Figure 3.16: Schematic of Bragg diffraction arrangement.

In crystallography, a crystalline material is described in term of its unit cell, which is a three-dimensional stack representing the spatial arrangement of atoms in the crystal. The unit cell of silicon is a diamond structure, as shown in Figure 3.17(a). In such structures, different crystallographic planes (i.e., the planes linking the atomic nodes) can be observed in Figure 3.17(b), (c) and (d) with their crystallographic directions indicated by arrows. These planes can be identified by their Miller indices h, k and l, reciprocals of fractional intercepts that the plane makes with the crystallographic axes x, y and z [150][151]. For cubic cells like silicon, the interlayer space between adjacent crystallographic planes is defined by:

$$d_{hkl} = \frac{\alpha}{\sqrt{h^2 + k^2 + l^2}}, \tag{3-5}$$

with α the lattice constant of the cubic cell. In silicon, the lattice constant is 5.431 Å [152][153]. A consequence of this dependence between the crystallographic direction and the d-space is that the diffracted beam angle depends on the crystallographic plane the incident beam is interacting with.

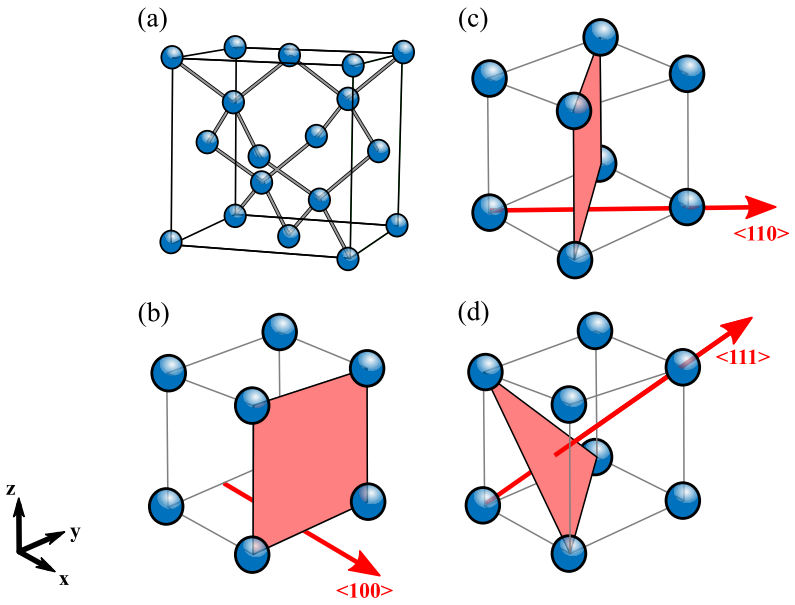

Figure 3.17: (a) Representation of Si diamond cubic crystal structure; (b), (c) and (d) Different crystallographic planes and directions in a primitive cubic cell.

When performing XRD on a polycrystalline material, which is a mixture of small crystals, it is common that the X-ray beam interacts with different crystals at the same time, resulting in the generation of different diffracted beams as illustrated in Figure 3.18. In this example, the yellow and the red crystals have both the <100> crystallographic plane interacting with the incident beam, hence, the yellow and the red diffracted beams share the same Debye cone on screen. However, because of their different orientations respectively to the incident beam, they hit the screen at different positions on the Debye cone. For the blue crystal, the incident beam interacts with the <111> plane, hence the beam is diffracted on a different Debye cone. Finally, the blue and the red crystals have the same plane orientation with respect to the incident beam as they are on the same radial line on screen.

To identify all the Debye cones accessible by our XRD system, we used a powder calibration technique which consists of scanning the powder of a crystalline material. As the powder contains all possible planes and orientations of the crystalline material, the Debye cones appear on screen, as shown in Figure 3.19, with each point corresponding to the diffraction of a small crystal with a particular orientation and crystal plane. The radii of these Debye cones are related to the 2θ angle and the distance between the sample and the detector. Thus, the range of observable Debye cones will then depend on the sample-detector distance and the wavelength used.

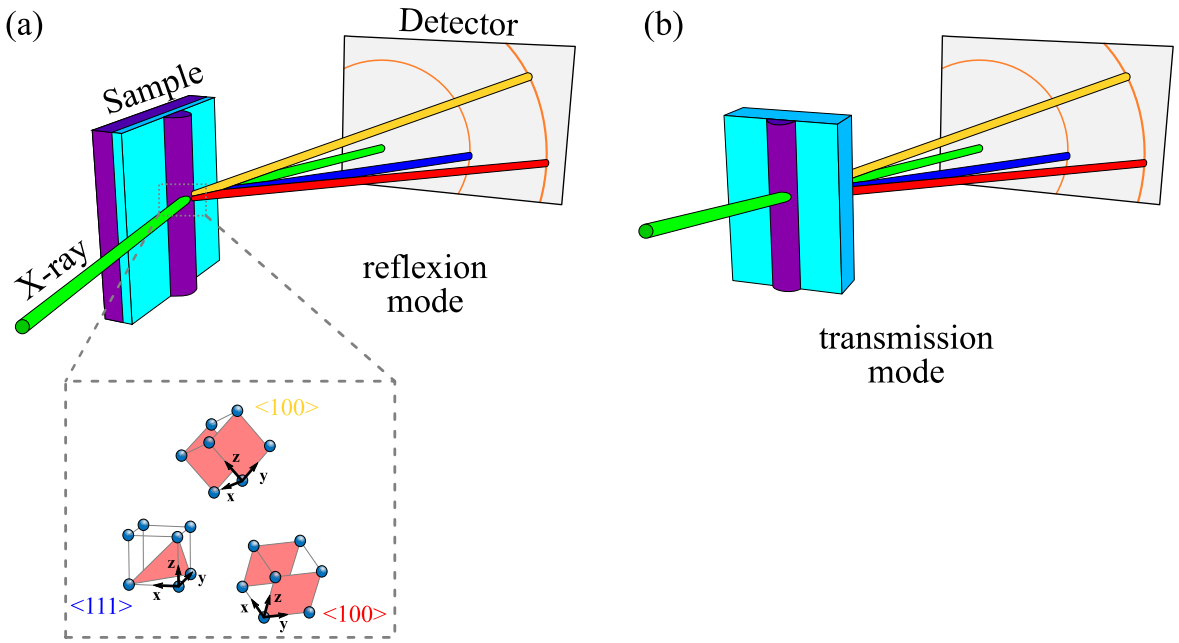

Figure 3.18: Illustration of an XRD experiment with a p-Si waveguide in grazing incidence (a) and transmission configuration (b). In the illuminated portion of the waveguide, three different crystals are diffracting the incident beam.

For our XRD experiments, depending on the sample under study, two different configurations have been used as shown in Figure 3.18. For samples with a c-Si substrate, the grazing incidence presented in Figure 3.18(a) has been used to limit the interaction of the incident beam with the substrate. By setting the incident beam with a 10^{o} angle with respect to the sample surface, only a small portion of the incident beam was diffracted by the substrate, resulting in two broad peaks on the diffraction patterns of these samples. On the other hand, samples with plain fused silica substrates, whilst being originally used in transmission configuration, can be used either way.

Finally, strain in a crystalline material can be observed and measured using an XRD system. As with Raman spectroscopy, strain in material induces a compression or an expansion of the atomic layers resulting in a decrease or an increase of the interlayer space. This modification of the d-space for a material under stress results in a change in the 2θ angle, hence, a shift on screen along the radial line. Compressive strain will increase the Debye cone radius whilst tensile strain will reduce it. The strain can then be calculated based on the stressed and unstressed d-space difference via Hooke law and the elastic modulus of the material [154][155]:

$$\sigma_x = E\,\varepsilon_x\,, \tag{3-6}$$

with σ_x the stress in x direction, E the elastic modulus and the strain $\varepsilon_x = (d_{stressed} - d_0)/d_0$.

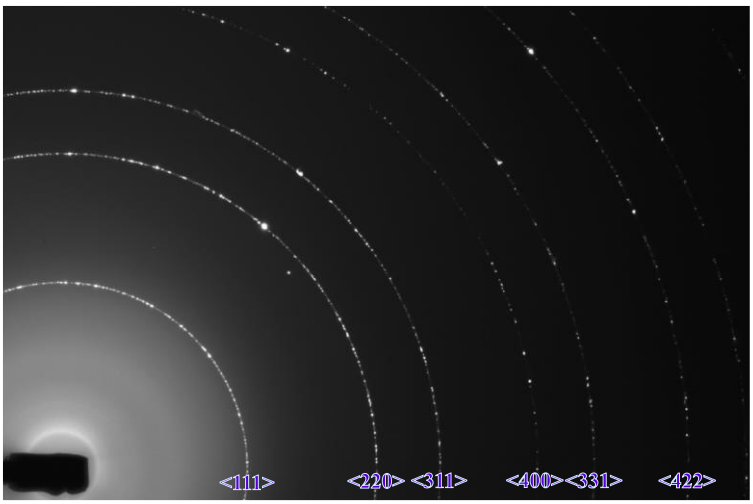

Figure 3.19: X-ray diffraction pattern of a silicon powder with crystallographic planes labelled.

All of our XRD experiments have been undertaken with the setup presented in Figure 3.20 at the Diamond light source (Didcot), a synchrotron where X-ray radiations are generated by bending accelerated electrons. This type of light source can generate the high intensity micro-focused X-ray beam required to characterise our waveguide samples which consisted of small volumes of material. In general, we worked with at a wavelength of 738 Å, 16.8 KeV, and our detector was able to capture one quadrant of the eight first silicon Debye cones.

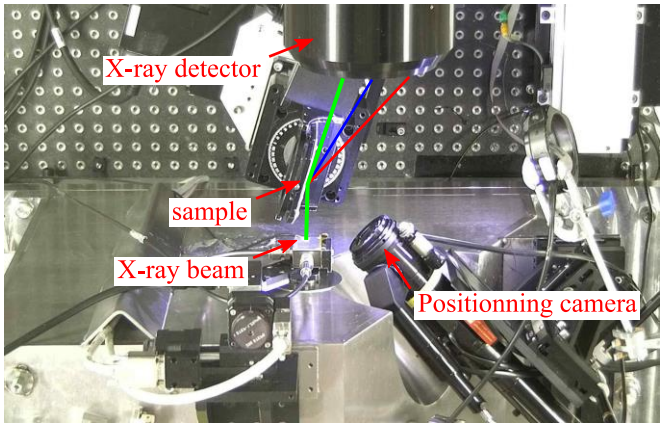

Figure 3.20: Top view photograph of the experimental setup for XRD. The blue and the red lines represent diffracted X-ray beams and the green lines the input and reflected X-ray beams.

3.5 Optical characterisation

In addition to material characterisation, optical measurements have also been realised to investigate and ensure the optical quality of the different samples fabricated during this project. For both planar

and fibre samples, the optical characterisation was composed of two steps: facet polishing and light transmission measurements, if the material quality is sufficient. Below is a detailed description of these two steps.

3.5.1 Facet polishing

Before any optical measurements can be undertaken, the waveguide facets first have to be polished to minimise coupling losses. To polish the planar samples, these were wax-mounted onto a jig by pair, with the silicon films facing inside for more protection, as shown in Figure 3.21(a). Then, the samples mounted on the jig were lapped on a rotating plate at 30 rpm using diluted aluminium oxide (Al_2O_3) particles of 9, 3 and finally 1 µm in diameter. At the end of this step, the facets of both samples are parallel, but not smooth enough for optical coupling as shown in Figure 3.21(a). For an optical polish, the jig was placed on a polishing plate at 20 rpm using a solution, labelled SF1, which contains fine silica particles of ~0.1 nm diameter for smooth polishing. Once finely polished, the facets can be inspected using an optical microscope to detect the presence of defects such as scratches, debris or film lift-of as shown in Figure 3.21(b). To avoid these defects, pressure was applied on the samples during the waxing step and the plates were thoroughly cleaned between each lapping and polishing step. At the end of the process, the samples were dismounted using a non-solvent solution and cleaned using acetone, isopropanol and de-ionised water.

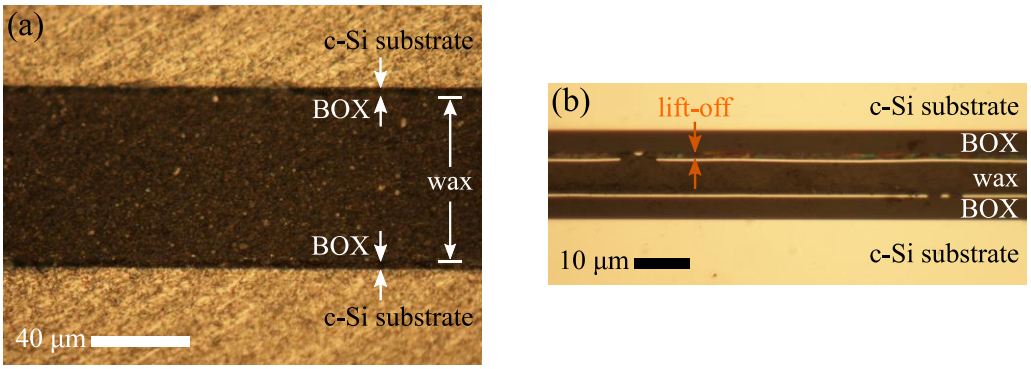

Figure 3.21: Optical microscope images of different wax-bonded planar samples after the lapping step using the 1 µm particles (a) and after the polishing step using the SF1 solution (b).

For fibre polishing, the technique was slightly different as these samples were more fragile. Before being polished, the fibres were wax-mounted into a thick silica sleeve, which was employed to act as a mechanical support during the polishing, as shown in Figure 3.22(a). Then the fibres were mounted onto a fibre polishing system composed of a fibre holder pressing the samples against a plate rotating at 80 rpm covered with humidified lapping sheets of 3, 1 and 0.02 µm grit size. For the cleaning of the polished fibres, only water and optical tissues were used as acetone would affect the wax that holds the fibre inside its silica sleeve. As for planar sample, the facets were checked under

the microscope for any trace of cracks or dirt. Figure 3.22(b) shows a polished fibre with a clean facet, whilst the fibre facet in Figure 3.22(c) contains scratches on the cladding and debris on the core facet. Simple microscope observations were adequate to reveal these defects.

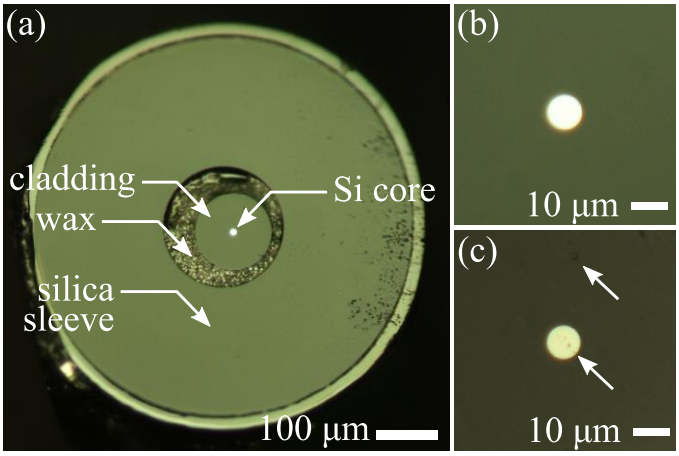

Figure 3.22: Optical microscope images of polished silicon core fibre facets. (a) Entire view of the fibre sleeved into the silica capillary, (b) clean facet, (c) facet with defects indicated by arrows.

3.5.2 Waveguide transmission setup

The transmission setup used for linear loss measurements is shown schematically in Figure 3.23. The source used was a tunable laser diode, a fiberized Tunics system, with 20 mW of maximal optical output power and an emission range from 1440 nm up to 1640 nm. The output beam from the fibre was collimated using a ×10 focusing objective and a three-axis micrometric stage. A beam splitter (90/10) was used for the beam alignment on the front facet of the sample and to verify the injection using an IR camera. The beam was then coupled into the waveguide using a ×60 fused silica microscope objective with 0.85 NA mounted on a three-axis piezo-controlled nano-positioning stage. A second ×25 fused silica microscope objective with 0.50 NA, also mounted on a three-axis piezo-controlled nano-positioning stage, was used to collect the output light from the waveguide. An iris was used to filter light leaking into the substrate or BOX layer. Finally, an IR powermeter was used to measure the power transmitted through the waveguide.

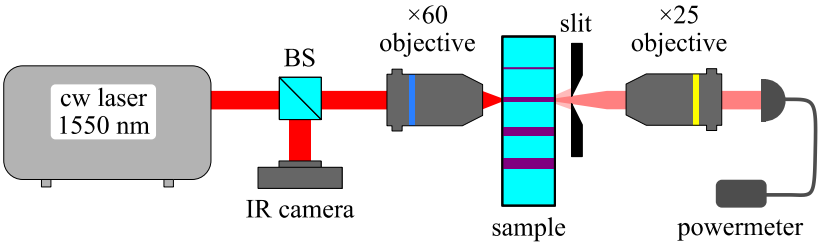

Figure 3.23: Schematic of the experimental setup for linear loss measurements.

Using the setup presented above, overall losses (propagation losses and injection losses) of the waveguide can be measured. To determine the propagation losses and eliminate the influence of the other losses, we used the cutback method, which involves measuring the overall losses through a long and short segment of the same waveguide [156]. A first overall loss measurement is performed on the waveguide followed by a polishing step as shown in Figure 3.24. The overall loss of the shorten waveguide is then measured and compared to the long segment to obtain the propagation losses using:

$$\alpha_L = \frac{-10 \log_{10}\left(\frac{P_1}{P_2}\right)}{dL}, \tag{3-7}$$

with α_L the propagation losses in dB/cm, P_1 and P_2 the output power of the long and short waveguide respectively and dL the length difference between the short and the long waveguide. Usually, this process was repeated several times, each time removing a length of ~1 mm.

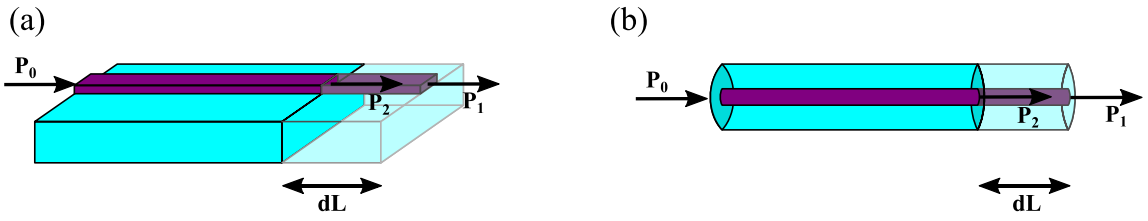

Figure 3.24: Cut back method schematic for both planar (a) and fibre (b) geometries.

Another technique based on interferometry has also been used to support the cutback results. Assuming good quality mirror facets, the Fabry-Pérot resonance technique involves measuring the waveguide losses from the fringe contrast (maxima and minima) produced by the waveguide acting as a cavity as we scan through the different wavelengths. Such measurement is possible due to the high refractive index difference between air and silicon. The advantage of this technique is that it requires only one measurement as it does not need the knowledge of coupling losses, hence, no waveguide shortening is required. The transmission intensity from a Fabry-Pérot cavity is [157]:

$$\frac{I_t}{I_i} = \frac{(1-R)^2 G}{(1-GR)^2 + 4GR\sin^2(\delta/2)}, \tag{3-8}$$

where $R = (n_1 - n_2)^2/(n_1 + n_2)^2$ the mirror reflectivity of facets with $n_1 \approx 3.45$ and $n_2 = 1$, I_i is the intensity coupled in the waveguide, I_t is the transmitted intensity, $G = e^{-\alpha L}$ represents linear losses for the waveguide of length L and $\delta = 4\pi n_1 L/\lambda$ is the round trip phase-shift. At the fringe maxima and minima, $\sin^2(\delta/2)$ becomes 0 and 1 respectively, hence, Equation (3-7) can be re-written as:

$$\alpha = -\frac{1}{L}\log\left(\frac{1}{R}\frac{\sqrt{r}-1}{\sqrt{r}+1}\right), \tag{3-9}$$

with $r = (I_t/I_i)_{max}/(I_t/I_i)_{min}$ the ratio between maximum and minimum transmission intensity. However, a limitation of this technique is that for multimode waveguides, the resonance peaks of each mode overlap and distinguishing the main resonance becomes difficult [158]. Still we can use this technique to confirm the results from our cutback measurements as it barely requires any modifications to the setup, as shown in Figure 3.25. The main modification is that we used a component tester (CT-400), to both normalise the input power coming from the tunable diode laser and to measure the sample output power as we scanned through the wavelengths.

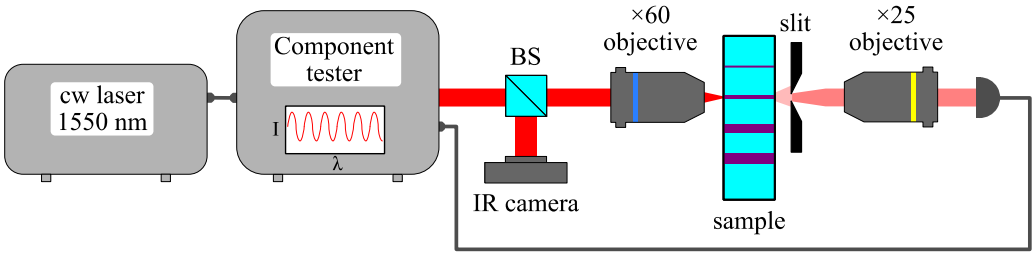

Figure 3.25: Experimental setup for linear loss measurements using Fabry-Pérot technique.

3.6 Samples summary

Throughout this project, planar samples have been fabricated with different geometries and compositions. To keep a track of the varied parameters the samples have been sorted into different "generations" as summarised in Table 3-5. Their deposition method along with the hydrogen content, thickness, patterning method and their deposition temperatures are indicated in this table. Also, samples of generation IV have been capped with a 1 µm thick silica cover deposited by PECVD at ~200 °C to instigate stronger heat confinement. The experiments conducted on these samples and their results are described in Chapter 4 and Chapter 5.

As the fabrication parameter space for the silicon core fibres is much smaller than the planar samples, the different samples will be presented along with the experimental results in Chapter 6.

	Gen. I	Gen. II	Gen. III	Gen. IV	Gen. V	Gen. VI
Deposition method	PECVD	PECVD	PECVD	PECVD	HWCVD	HWCVD
Material	a-Si:H	a-Si	a-Si	a-Si	a-Si	a-Si
Film thickness (nm)	250	250	250	250	220	400
Patterning method	x	x	PL	PL	EBL	EBL
Deposition Temperature (ºC)	350	350	350	350	320	320
Silica capped before laser processing	x	x	x	1 µm	x	x

PL: photolithography, EBL: e-beam lithography

Table 3-5: Summary of planar samples used during this thesis.

Chapter 4

Laser crystallisation of a-Si planar films

4.1 Introduction

This chapter presents an overview of the laser processing experiments on a-Si films. This work makes use of our first generation of samples deposited by PECVD on glass substrates. The purpose of this preliminary work was to estimate a range of useful laser processing parameter values to obtain good crystalline quality. These experiments also provided an opportunity to test the different characterisation techniques to monitor silicon crystallisation. The first part of this chapter describes our laser writing setup, including a discussion on the limitations associated with some of the setup components. Both hydrogenated and dehydrogenated amorphous silicon films have been studied under different laser processing conditions. Optical microscopy, Raman spectroscopy and chemical etching were all used to identify optimal combinations of scanning speed, laser power and spot size to obtain the large crystals.

4.2 Laser processing setup

To crystallise our amorphous silicon samples, we used a laser setup composed of different elements as illustrated in Figure 4.1.The laser source that was used in these experiments was an argon ion laser delivering up to 1 W of continuous wave (CW) radiation at a 488 nm wavelength which is strongly absorbed by silicon. The linearly polarized Gaussian beam was found to have a FWHM of 1.84 mm, measured using the knife edge method, before the microscope objective [159]. The beam intensity was initially controlled using a metallic neutral density filter, but this was found to be inappropriate for the laser power we used. Thus, this was replaced with a half-wave plate combined with a

polarisation cube. The beam was then focused onto the sample surface using a microscope objective mounted on a vertical stage to control the focus. The sample was then placed on a vacuum holder mounted on two air-bearing micro-precision stages to position it within the XY-plane. The three stages of this setup were controlled by a computer using G-code, also called RS-274, which is a programming language mainly used in computer-aided manufacturing. While G-code is capable of realising complex drawings, we have essentially written basic scripts to draw straight lines, while maintaining the focused beam on the sample surface.

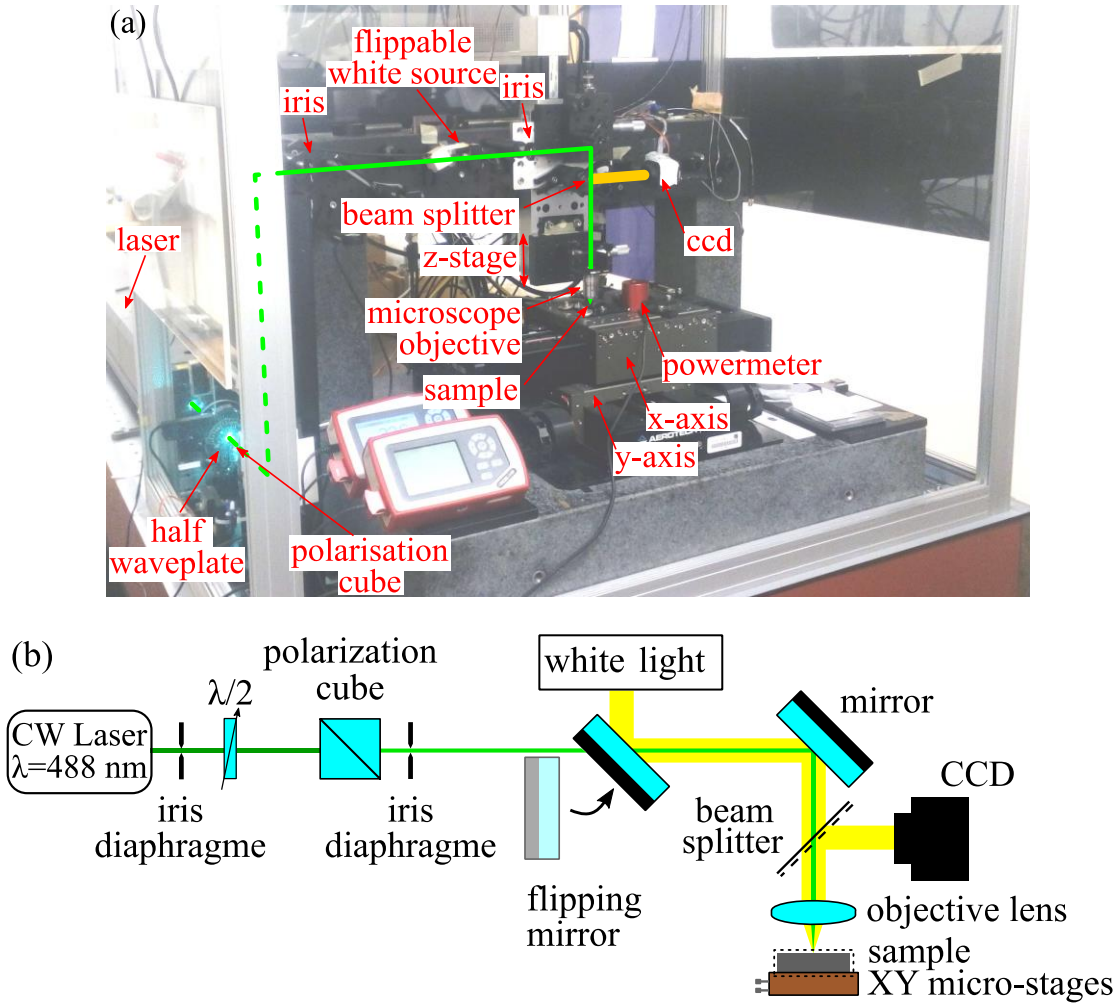

Figure 4.1: Photography (a) and schematic (b) of the experimental setup for laser processing.

To position the sample relative to the beam and to quickly verify that the beam was focused on the sample surface before and after laser processing, an imaging system was added to the setup consisting of a white light source and a CCD camera.

Several microscope objectives have been used depending on their working distance, image contrast or spot size. Initially a ×36 reflective objective was chosen for its 1 cm long working distance to avoid material re-deposition on the objective during the laser processing. However, we eventually switched to transmission objectives (×10, ×20) to avoid the power loss which is associated with

reflective objectives. The beam spot sizes that were obtained with these objectives, reported in Table 4-1, were calculated using the working wavelength λ and the lens numerical aperture NA [160]:

$$\text{Spot radius} = \frac{0.61 \cdot \lambda}{\text{NA}} \tag{4-1}$$

These were also estimated experimentally by first using the edge knife method to measure the spot size at different positions in the far-field and then extrapolating these results with Gaussian beam optics to obtain the focused beam radius ω_0. The radius is defined as [161]:

$$\omega_0 = \frac{\lambda}{\pi\,\theta}, \tag{4-2}$$

where θ is the far-field divergence of the beam after the microscope objective. The spot-sizes measured for the different objectives are reported in Table 4-1 and their values are consistent with the dimensions seen on the processed tracks, as shown later in this report. The difference between the calculated and the measured spot sizes is due to the fact that the laser beam is smaller than the objective entrance pupil which results in larger spots. For this project, we used the experimentally measured values of 2.50 µm and 4.70µm for ×20 and ×10 objectives, respectively.

Objective	NA	Theoretical calculated spot size diameter (µm)	Measured spot size diameter (µm)
×36	0.52	1.14	-
×20	0.40	1.48	2.50
×10	0.25	2.38	4.70

Table 4-1: Summary of objectives spot sizes with both calculated and experimentally measured spot size diameters.

4.3 Laser crystallisation of a-Si and a-Si:H films

Preliminary laser crystallization experiments were performed on Generation I and Generation II samples. Generation I samples have a 250 nm thick a-Si:H film deposited by PECVD on a fused silica substrate at 350 °C. Although a-Si:H waveguides are popular for the development of low loss optical waveguides, the rapid out-diffusion of hydrogen during the laser processing step was a concern. Therefore, Generation II samples were fabricated the same as Generation I samples but were later pre-treated in a furnace at 450 °C for 1 hour to slowly out-diffuse hydrogen from their silicon films. To validate the presence and absence of hydrogen in Generations I and II respectively, Raman spectra have been measured around the predicted hydrogen peak positions, 2000-2100 cm^{-1}, as shown in Figure 4.2. For the spectrum on the left, corresponding to Generation I, both Si-H and Si-H_2 vibrational peaks are visible thus confirming the presence of hydrogen. However, for Figure 4.2(b),

corresponding to Generation II samples, no peaks are visible thus confirming the furnace dehydrogenation process.

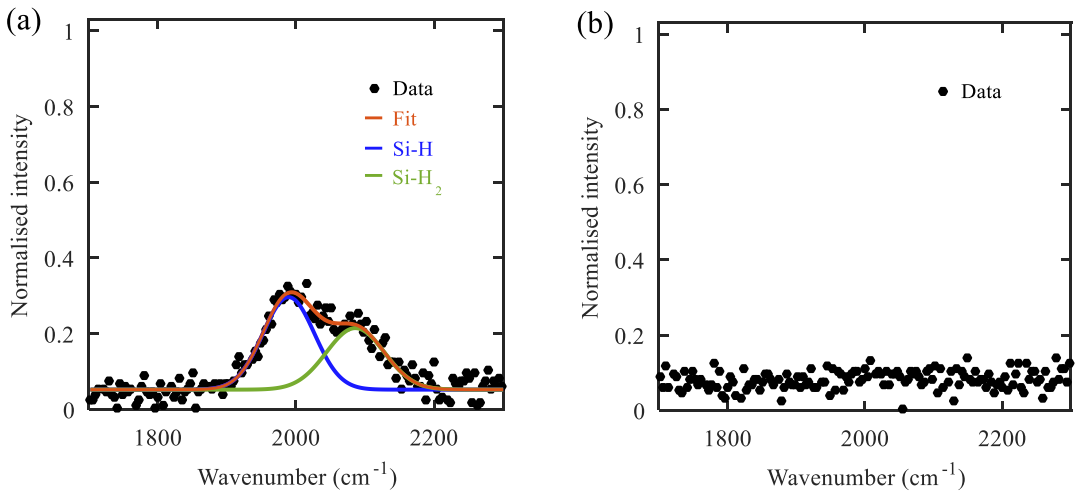

Figure 4.2: Raman spectra of Generation I (a) and Generation II (b) samples.

To investigate the influence of laser processing power and scanning speed on the crystallisation process, many p-Si tracks were written onto the films using combinations of different powers and speeds within the range of 100 – 350 mW and 0.001 – 10 mm/s, respectively. A ×10 objective with a spot diameter of 4.70 µm was used for the writing of all of the tracks on both a-Si:H and a-Si films.

4.4 Optical microscopy characterisation

The characterisation of the p-Si tracks written onto the planar films starts with optical microscope observations. Using a ×100 objective, the p-Si tracks were imaged and sorted by processing power and scanning speed for a visual interpretation as shown in Figure 4.3.

In both a-Si:H and a-Si, a damage threshold clearly exists at different positions depending on the scanning speed and the laser power. As discussed in Chapter 2, silicon crystallisation can be divided into different regimes depending on the energy absorbed by the material. In Figure 4.3, non-damaged p-Si tracks denoted by the blue lines, such as a-Si:H processed with 150 mW at 0.01 mm/s or a-Si processed with 125 mW at 0.1mm/s, represent a regime where silicon is partially molten and crystallises whilst cooling down. However, at higher absorbed energy, p-Si tracks denoted by the red lines, such as a-Si:H processed with 250 mW at 0.1 mm/s or a-Si processed with 300 mW at 0.01 mm/s, are damaged. These black areas indicate the size of the heat-affected zone from where molten material has been ejected by laser ablation [162].

It is important to note that the ablation threshold increases with scanning speed as the energy absorbed by the material decreases. Also, the fact that a-Si:H thresholds are higher than a-Si thresholds could be explained by the band gap energy of a-Si:H which increases with the hydrogen

concentration resulting in a lower absorption at 488 nm for higher hydrogen concentrations [163] [164]. Finally, the orange delimited p-Si tracks, from a-Si:H processed with 100 and 125 mW at 0.001 mm/s and from a-Si processed with 150 mW at 0.01 mm/s, are unstable tracks where several segments of both partial melting and ablated regimes were observed. From these observations, a range of laser irradiation conditions corresponding to good quality material is expected to be located for laser powers below the damaging threshold, 150-180 mW for a-Si:H and 125-200 mW for a-Si depending on scanning speeds.

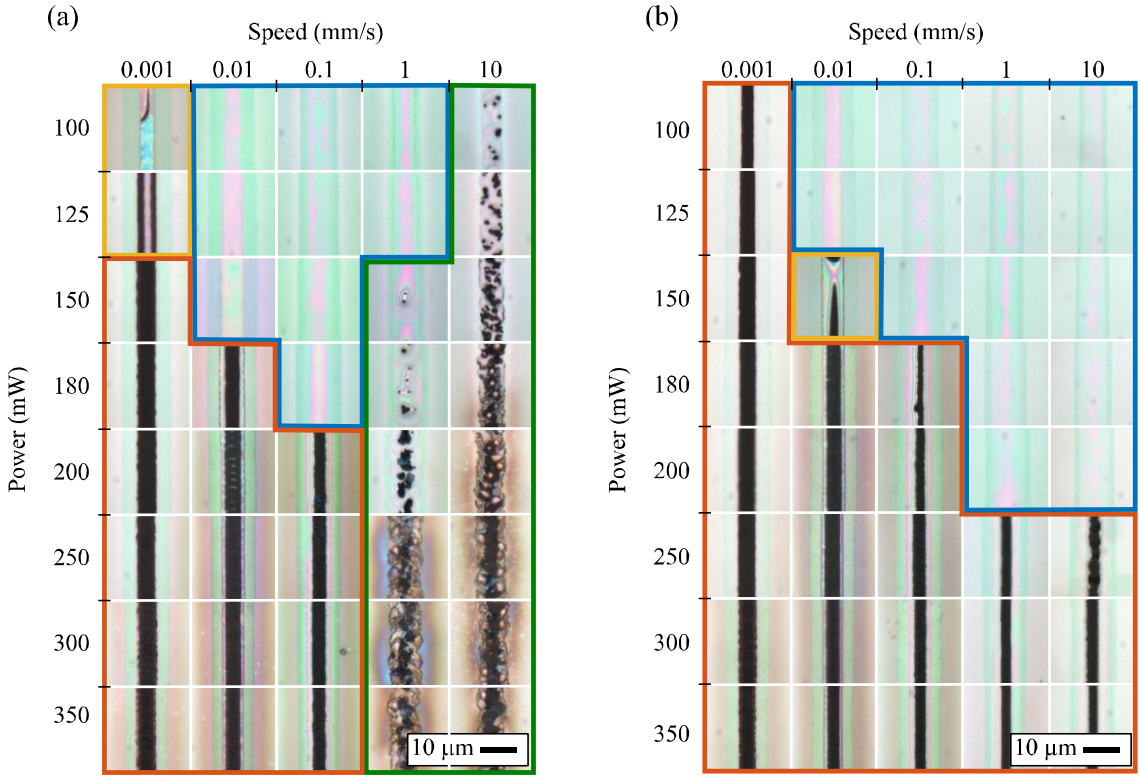

Figure 4.3: Optical microscope images of p-Si tracks for different laser processing powers and scanning speeds. (a) Generation I a-Si:H, (b) Generation II a-Si thermally annealed for 1h at 450°C.

Another observation in Figure 4.3 is that for scanning speeds higher than 1 mm/s, some p-Si tracks indicated with the green boarder are damaged in the case of a-Si:H only. There is no clear explanation for this phenomenon, however it could be attributed to violent out-diffusion of hydrogen.

At high scanning speed and low power, the a-Si:H material does not receive enough energy to melt and the hydrogen gas out-diffuses violently damaging the surface. For laser powers of 250 mW at 1 mm/s and 200 mW at 10 mm/s, violent hydrogen out-diffusion coupled with laser ablation results in largely damaged films with visible cracks. This effect only appears at high scanning speeds. For speeds slower than 1 mm/s, the heating induced by laser processing is sufficiently slow to leave enough time for the hydrogen to out-diffuse gently. For scanning speeds of 1 mm/s or faster, the steep heat gradient can be associated to the pulsed laser case where hydrogen violent out-diffusion has already been reported on a-Si:H[165].

Finally, Figure 4.3 reveals that despite using a ×10 objective with a 4.7 µm spot diameter, structures larger than the spot size are formed. In the a-Si:H material processed with 180 mW at 0.1 mm/s, the central pink feature and the larger green feature are 5 and 12.6 µm wide, respectively. This provides evidence that sharp features are difficult to obtain within planar films using this method.

As our optical microscope is equipped with a differential interference contrast (DIC) option, it is possible to increase the contrast in fine features contained in our laser-crystallized tracks. By using birefringent glasses and a polarizer, the contrast between the a-Si and p-Si features can be enhanced because of their different refractive indices. In Figure 4.4(a), no particular details can be observed on the p-Si tracks from a-Si:H processed with 125 mW at 1 mm/s, however when using DIC in Figure 4.4(b), the polycrystalline structure of the track is revealed. The "chevron" crystal pattern, pointing in the writing direction (from bottom to top), reveals micrometre long crystals in the middle, whilst the side of the track is only populated by small crystals as described in Chapter 2. This observation confirms the formation of polycrystalline silicon but also reveals the limitations of planar samples where the sides of the processed track cool down too fast leading to formation of small crystals. This problem is address in the following chapter by geometrically confining silicon material into a pre-structured wire structure.

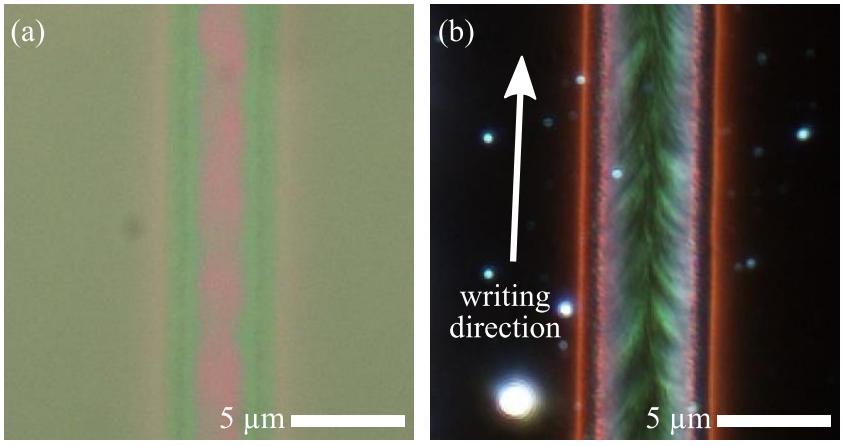

Figure 4.4: Optical microscope images of a track written at 1 mm/s with 125 mW on a-Si:H without (a) and with (b) differential interference contrast imaging.

4.5 Raman characterisation

As shown in Chapter 3, Raman spectroscopy can be used to characterize material quality of a p-Si wire by measuring the Lorentzian peak width Γ and position, and then comparing them to the c-Si reference peak width (2.7 cm^{-1}) and position at (520 cm^{-1}). Raman results are summarised in Figure 4.6 and Figure 4.7, where the Γ and peak position values of each laser processing condition have been mapped. For clarity, only the data associated to properly fitted spectra as in Figure 4.5(a) are presented. If the associated Raman spectrum is too noisy as in Figure 4.5(b), both Γ and peak position

are set blank. Usually, spectra that are too noisy to be fitted correspond to damaged tracks where all the silicon has been ablated. However, some damaged tracks such as the p-Si track processed with 350 mW at 1 mm/s, had enough remaining material for the spectrum to be fitted. Hence, both Raman spectroscopy and optical microscopy have to be jointly used to find out optimal crystallisation parameters.

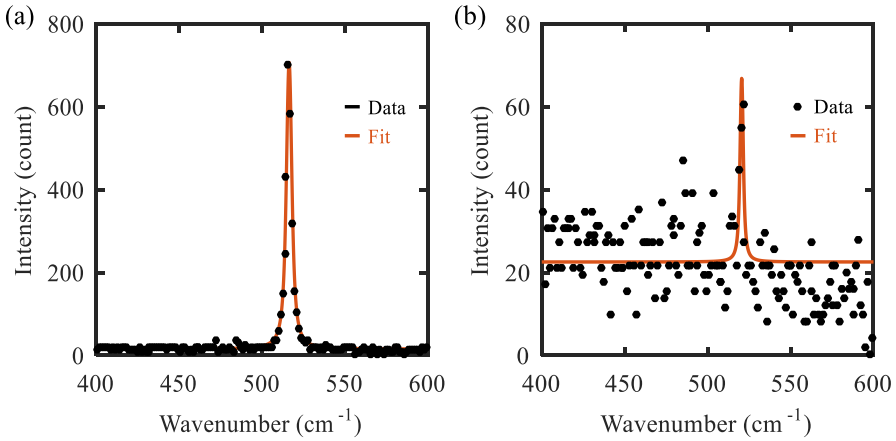

Figure 4.5: (a) Raman spectrum of a-Si:H laser processed with 125 mW at 1 mm/s conserved for Raman analysis, (b) Raman spectrum of a-Si:H laser processed with 300 mW at 1 mm/s not considered for Raman analysis because of its noise level.

The first Raman results presented in Figure 4.6 correspond to the a-Si:H film. From the Raman peak width analysis shown in Figure 4.6(a), it is revealed that p-Si tracks with high degrees of crystallinity correspond to the 100 – 180 mW range for scanning speeds between 0.1 and 1 mm/s as denoted by the magenta lines. The best crystallisation, as indicated by $\Gamma = 2.91$ cm^{-1}, was obtained with 100 mW at 1 mm/s.

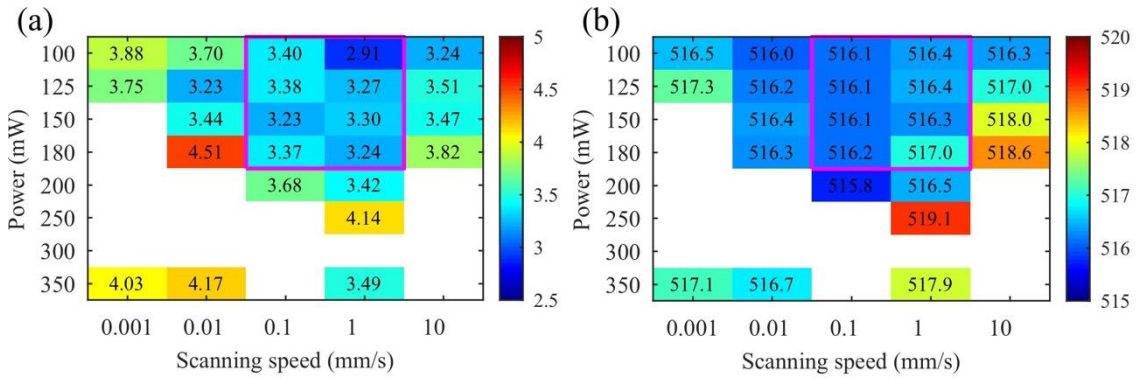

Figure 4.6: Raman maps of laser processed a-Si:H for different scanning speeds and powers with Lorentzian peak width Γ (a) and position (b). The magenta lines denote optimal laser processing conditions.

In Figure 4.6(b), the peak position analysis reveals a general tensile strain, induced by unmelted wings that pull the material whilst cooling down, with an average value of 516.4 cm^{-1}. However, for

the 1 and 10 mm/s scanning speeds where hydrogen out-diffusion has been observed by microscopy, the Raman peak is shifted toward higher frequencies compared to the tracks denoted by the magenta line. Our hypothesis is that when hydrogen out-diffuses it compresses silicon atoms resulting in a Raman shifted toward higher frequencies. Stressed peaks are also observed on the sides of damaged tracks such as the track processed with 350 mW at 10 mm/s where in this case the atoms are compressed due to the violent laser ablation process.

Similar analysis can has been conducted for the de-hydrogenated silicon films with the Raman results shown in Figure 4.7. As with the a-Si:H film, most of the damaged tracks cannot be fitted and the remaining peaks correspond to residue leftover from the laser ablation. From the width analysis in Figure 4.7(a), p-Si tracks with high degrees of crystallinity are localised in the 100 – 200 mW range for scanning speeds between 1 and 10 mm/s as delimited by the magenta lines, with the best crystallisation, $\Gamma = 2.87$ cm^{-1} , also obtained with 100 mW at 1 mm/s. In Figure 4.7(b), the peak position analysis reveals that, in absence of hydrogen, p-Si tracks processed at 1 and 10 mm/s are not stressed. Apart for some tracks with peaks position slightly shifted in higher frequencies due the compressive strain remaining after laser ablation, all p-Si peaks are centred around 516 cm^{-1}.

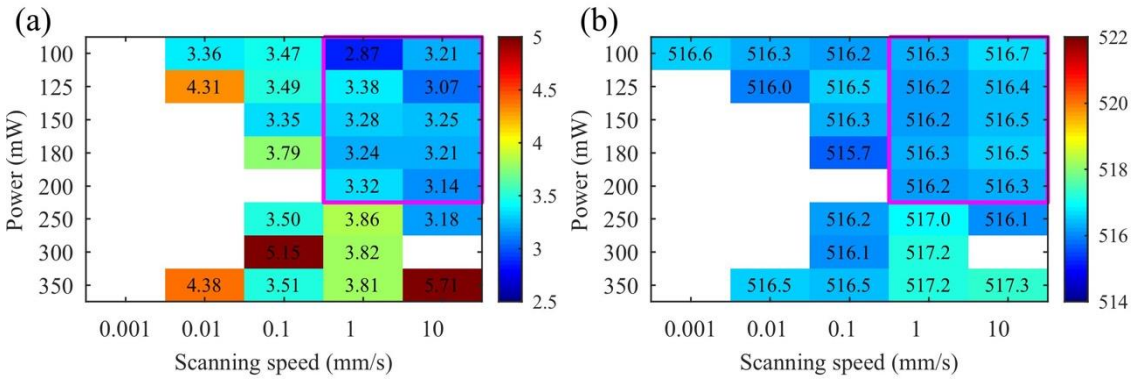

Figure 4.7: Raman maps of laser processed a-Si for different scanning speeds and powers with Lorentzian peak width Γ (a) and position (b), respectively.

For both the a-Si:H and a-Si materials, the average peak position is centred around 516.2 cm^{-1}, despite a good degree of crystallisation with an average width Γ of 3.2 cm^{-1}. A possible explanation is that, when the molten silicon cools down, it would naturally occupy a smaller volume as c-Si is denser than a-Si [44]. However, due to the planar geometry, the sides of the heat affected zone remain solid and apply tensile strain on the molten phase by surface tension. When the p-Si cools down, this tensile strain results in a peak position shifted toward low frequencies compared to the expected 520 cm^{-1}.

4.6 Preferential etching

Following the completion of our optical and Raman microscopy analysis, the samples were subject to analysis via etching to reveal information about the crystal boundaries. Besides acting as preferential sites for segregation of impurities during crystal growth, crystal boundaries are also filled with weak Si-Si bonds due to mismatches between different crystalline domains. Because of these disordered weak bonds, silicon material present at the crystal boundaries are considered to be amorphous, so that they can be selectively etched away using specific chemicals.

Different etching solutions such as potassium hydroxide [166], Sopori etch [167] and Secco etch [166] are used in the silicon industry. In our experiments, we used the Secco etch solution, which is composed of an oxidizing agent, potassium dichromate ($K_2Cr_2O_7$), that is used to oxidize the weakly bonded silicon at crystal boundaries to form silica, and hydrofluoric acid (HF), which is a silica etchant. Using two parts of HF (48%) and one part of $K_2Cr_2O_7$ (0.16 M), diluted 10 times in water for a more accurate control over time, the a-Si etching rate was measured to be 150 nm/min.

At the end of the etch process, the crystal boundaries are revealed as trenches that could be easily observed using a SEM. With this technique, crystals with length up to 6 µm have been observed as shown in Figure 4.8 where a laser processed track has been imaged before and after Secco etch treatment.

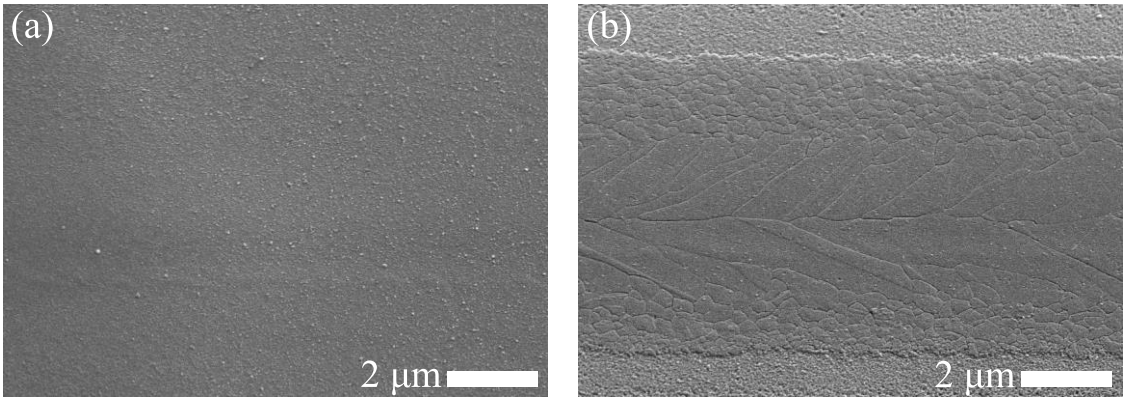

Figure 4.8: SEM micrographs before (a) and after (b) Secco etch treatment on a-Si irradiated with 125 mW at 1 mm/s.

In contrast to the SEM micrograph of the non-etched sample, where crystal boundaries are not visible, the Secco etched sample micrograph reveals micrometre long crystals. As expected, large crystals are formed in the middle, whilst lots of small crystals form at the tracks edges due to the faster cooling rate. This process will be discussed in more details in Chapter 5. This final analysis, despite being destructive, validates our observation with the microscope equipped with the DIC system and gives a clear confirmation about the need to improve the heat confinement in order to improve the crystallisation quality and grow larger crystals.

4.7 2D patterning

As discussed earlier in this chapter, the high precision 2D translation stages of the laser-writing setup allow for the irradiation of complex patterns using the G-code language. By combining the laser processing technique to selectively crystallise a-Si, and the Secco etching to remove unexposed a-Si, it is possible to easily and quickly transfer a pattern designed on a computer directly onto a planar a-Si film. As a proof of concept, a pattern composed of tracks and circles similar to a ring resonator device but with a ring overlapping the waveguide, has been designed and transferred on to an a-Si film, using the laser scanning parameters of 130 mW and 0.1 mm/s. After Secco etch treatment, the structure is revealed in Figure 4.9 where large crystals can be observed in the centre with smaller crystals forming edges, as expected. The small crystals composing track edges create a rough surface that would generate optical losses in such waveguide. However, in the section where the ring overlaps with the waveguide, we see evidence of crystals merging, as shown in Figure 4.9(b). Thus the effect of the double pass laser scan on the processed material helps to transform the initial low quality edge of the track into larger, high quality crystals. Therefore, we expect that a second scan with the laser over the track edges could be used to improve the p-Si material after Secco etching.

This work has not been pursued further in this thesis as it was dedicated to another project. Besides, the heat diffusion problem, which results in large p-Si tracks, is still a concern for obtaining high precision designs via this approach.

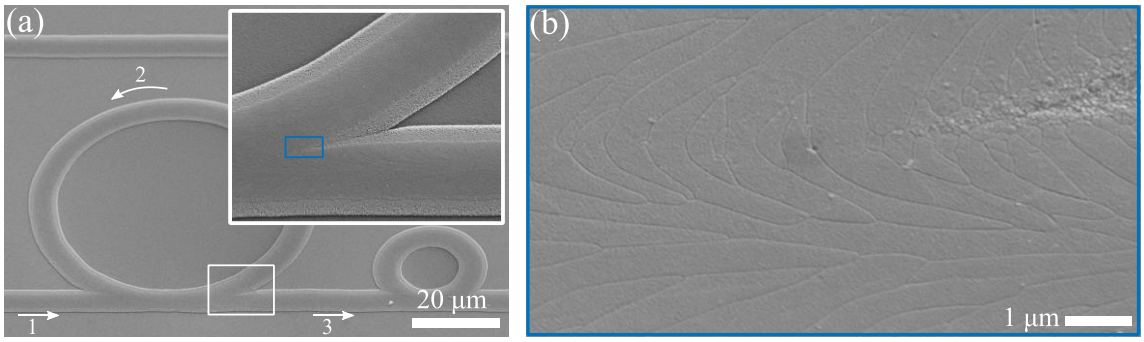

Figure 4.9: SEM micrographs after Secco etch treatment of an a-Si film, laser processed in the order indicated by arrows with 130 mW at 1 mm/s. (a) Overall view of the structure. Inset: close up to the junction area. (b) Magnified view of the inset where the crystals have merged.

4.8 Conclusion

In this chapter, preliminary work to investigate laser processing of a-Si thin films has been presented. Using optical microscopy combined with Raman spectroscopy, combinations of processing powers and scanning speeds have been obtained for the formation of p-Si tracks with the best Lorentzian

widths Γ of 2.91 and 2.87 cm^{-1} for a-Si:H and a-Si, respectively. The role of hydrogen in the crystallisation process has been studied. Using Raman spectroscopy, the stress of the p-Si tracks has also been estimated, revealing a general tensile strain for p-Si tracks grown in planar films. Finally, crystalline structures have been observed with both optical microscopy and with the use of a destructive acid treatment revealing silicon crystals up to 6 µm long in the laser exposed a-Si areas.

The growth of silicon crystals using our laser processing method along with the ability to observe and characterise them validates this preliminary work. Different concerns encountered in this chapter will be addressed in the following chapter. To improve the crystallisation process and grow larger crystals, pre-patterned a-Si wires will be used as a starting material instead of planar films, which lack lateral heat confinement. Also, to prevent hydrogen abrupt out-diffusion during the laser processing, only hydrogen-free silicon will be used in the remaining work of this project.

Chapter 5

Pre-patterned silicon waveguides

5.1 Introduction

As shown previously, laser crystallization can grow silicon crystals up to 6 µm long on a-Si planar films. In this chapter, laser crystallization experiments on pre-patterned a-Si wires are presented with the goal to improve the crystallisation process. The first part of this chapter contains details of the different sample generations and discusses their potential impact on the crystallisation process. This includes samples with different waveguide widths, thicknesses, and substrate type, as well as those deposited using different methods and the addition of a silica capping layer. The second part of the chapter is focused on the last generation of samples, Gen. VI, and presents the latest results on both material and optical characterisation.

5.2 Material impacts of different fabrication parameters

5.2.1 Visual inspection of p-Si tracks before analysis

In this section, a variety of patterned sample generations, from Gen. III to Gen. VI, are studied. After being laser processed, their material characteristics are inspected using the different tools presented in Chapter 4. Because of the large number of p-Si tracks that have been processed during this project, optical microscopy imaging has been used to quickly inspect the quality of each laser processed track and estimate its degree of crystallisation. The p-Si tracks are sorted into five different categories as shown in Figure 5.1.

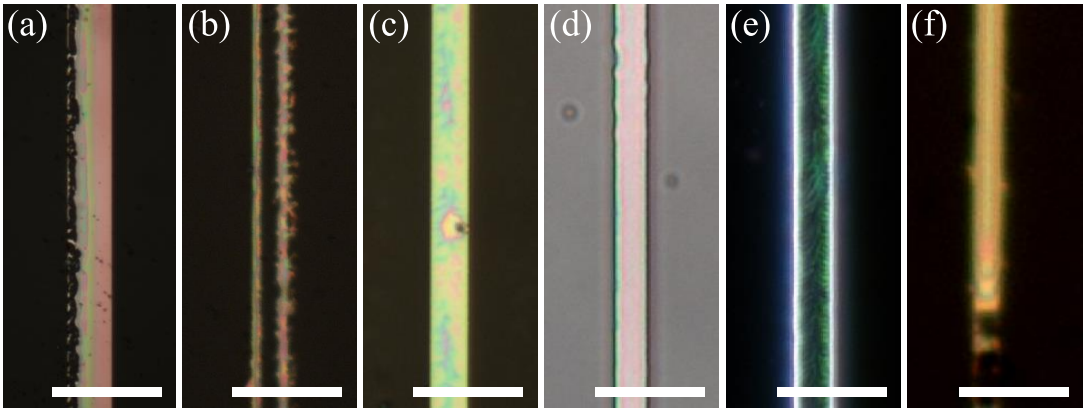

Figure 5.1: Optical microscope images of the five categories for laser processed p-Si tracks observed throughout this thesis. (a) Side processing, (b) damaged wire, (c) under processed inhomogeneous wire, (d)-(e) homogeneously processed wire with crystals in chevron pattern imaged, without and with DIC system, and (f) homogeneous rounded wire with long crystals with alignment marks at the bottom. [scale bars: 5 µm]

The first category, presented in Figure 5.1(a), corresponds to a misalignment of the laser beam with respect to the a-Si wire, resulting in a partially processed p-Si track. To address this issue, which was not present in the previous planar study, finer steps have been used in our G-code scripts and alignment of the beam to the a-Si track was checked regularly to assess proper operation of the setup. Also, the microscope objective used to focus the laser beam on the a-Si track was adjusted to ensure that the spot size was larger than the processed wire. Figure 5.1(b) represents a wire that has been damaged because it received too much power. As with the a-Si films, the material has been ablated resulting in a black area at the centre. The p-Si material on the edges remains as these areas cool down faster than the central area. The p-Si track presented in Figure 5.1(c) reveals clear modification of the initial a-Si material. However, the inhomogeneity of its surface indicates a low degree of crystallisation. Figure 5.1(d) and (e) are two micrographs of the same track captured without and with the DIC system, respectively. Under regular top illumination, the p-Si track looks homogeneously modified, however, the refractive index contrast is enhanced with the DIC system and crystals organised in a chevron pattern can be observed. Finally, Figure 5.1(f) represents the most promising type of p-Si track. This wire was processed from the bottom to the top, and the black spot visible under the track serves a mark to locate the centre. The rounded iridescent pattern at the start of the track indicates a smooth rounded shape and the homogeneity of this pattern along the track suggests the presence of long crystals.

Observations of these different categories have been used throughout this entire project to perform quick estimations and reduce the number of parameter combinations. The good materials were then characterised in more detail to determine the effect of individual fabrication.

5.2.2 Effect of the wire width

The first set of a-Si wires were fabricated on Gen. II films, which underwent a furnace annealing process to remove hydrogen. The 250 nm thick film was patterned into wires with widths varying from 10 to 2 µm using photolithography. Laser processing was performed using a ×20 objective, giving a 2.5 µm diameter spot for a total overlap with the thinner wires and a partial overlap for wider wires. Three different laser powers were considered, 100, 120 and 150 mW, with the scanning speed fixed at 0.1 mm/s. The Raman results of these processing processes are presented in Figure 5.2.

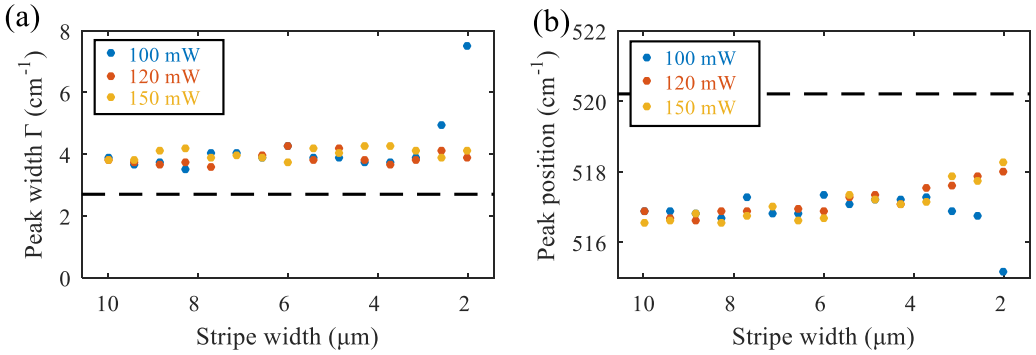

Figure 5.2: Evolution of Raman peak width (a) and position (b) for different p-Si wire linewidths. [scanning speed: 0.1 mm/s, dashed lines: c-Si reference]

For the three powers in Figure 5.2(a), the Lorentzian peak width Γ is relatively unchanged across all linewidths, except for a sudden increase for the two smallest tracks at 100 mW. Some changes were expected for wires smaller than the laser spot, but no obvious trends were observed, except for the increase at 100 mW. With an average width of 3.9 cm^{-1} and the lowest value being 3.52 cm^{-1}, the degree of crystallisation of these p-Si tracks is low. In Figure 5.2(b), the peak position is constant from 10 to 6 µm for the three powers and then the lines processed at 120 and 150 mW increase toward the c-Si reference, whilst the lines at 100 mW shifts toward lower frequencies. Because the peak width is not varying for different widths of wires, the peak position shift is attributed to stress and not to the crystallisation quality [140]. This stress originates from the mismatch between the wire width and the heat affected area which is larger than the spot diameter. For linewidths larger than 6 µm, the heat affected zone is smaller than the wire, which behaves as a planar structure, i.e., maintains solid sidewalls that apply tensile strain as the p-Si cools down, as explained in Chapter 4. For linewidths below 6 µm, most of the wire is softened by heat, hence less tensile stress. The p-Si material being more and more relieved from stress, the Raman peak shifts toward the frequency associated to its p-Si material quality when free of stress. Compared to the 120 and 150 mW tracks, the lower laser processing power of the 100 mW tracks combined with small wires resulted in the formation of smaller crystals, as revealed by the Γ increase in Figure 5.2(a). As small crystals have an associated Raman frequency situated toward lower frequencies, this justifies the shift in Figure 5.2(b). For example, we note that the nano-crystals Raman peak is situated around 514 cm^{-1}.

For the remainder of this project, except for generation IV samples, which were based on generation III, we decided to opt for smaller linewidths with wire widths between 1-2 µm. In addition to being totally covered by the 2.5 µm laser spot, these dimensions are closer to photonic waveguide standards.

5.2.3 Effect of the deposition method and crystalline substrate

As discussed in Chapter 3, during this project samples changed from PECVD deposited on glass substrates to HWCVD deposited on a c-Si substrate with a 4.7 µm thick BOX layer. Because two different film deposition methods have been used, the purpose of this study is to assess the repeatability of the results obtained on generation III, 250 nm thick a-Si deposited by PECVD, for comparison with those of generation V, 220 nm thick a-Si deposited by HWCVD.

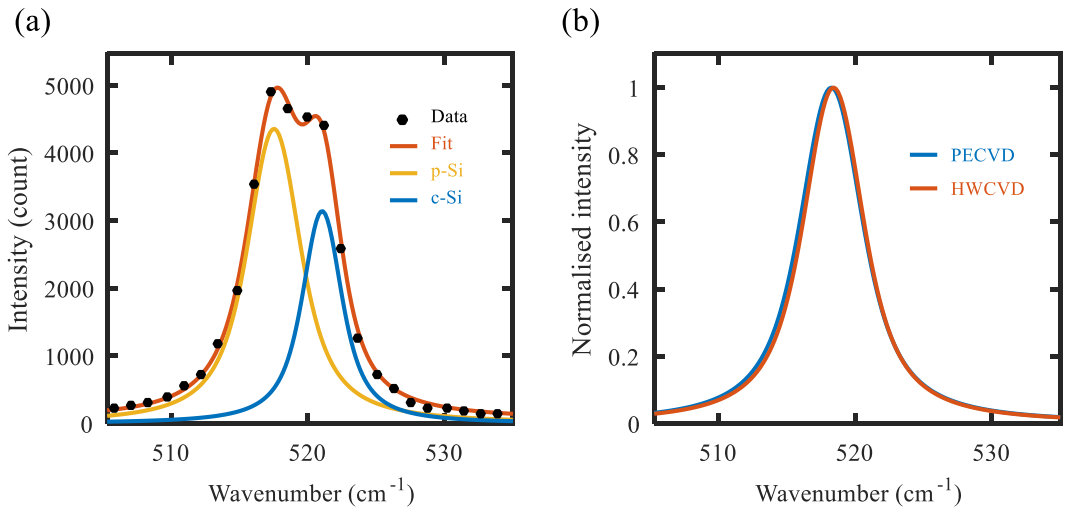

Figure 5.3: (a) Raman spectrum of a generation IV sample using the two peaks fitting method. (b) Raman Lorentzian fit comparison of PECVD (blue) and HWCVD (red) a-Si wires laser processed with 270 mW at 0.1 mm/s.

Figure 5.3(a) shows the Raman spectrum of a 2 µm wide, HWCVD deposited a-Si wire laser processed with 260 mW at 0.11 mm/s using a ×20 objective. Compared to the generation III samples, this shows a broader Raman feature, which appears to contain two individual peaks. For a Raman excitation wavelength of 532 nm, the penetration depth in silicon is deeper than the thickness of the silicon wire, hence a portion of the excitation laser radiation reaches the c-Si substrate. Therefore, the Raman spectrum contains a peak from the c-Si substrate, which has to be taken into account during the fitting. The two-peak fitting method presented in Chapter 3 is validated by the strong agreement of the overall fitting with the data points. However, because of the presence of the c-Si substrate peak in some generations, the raw datasets from generation III and generation V cannot be compared directly. Figure 5.3(b) shows the fitted Lorentzians extracted from Raman spectra acquired from two different generations but processed with the same conditions. Both a-Si tracks were 2 µm

wide and 220 - 250 nm high, and both have been laser processed with 270mW at 0.1 mm/s using a ×20 objective to focus the laser beam. The width Γ of these peaks is 4.22 and 4.08 cm^{-1} for PECVD and HWCVD, respectively, whilst the positions of these peaks are 518.25 and 518.40 cm^{-1}. These differences, slightly higher than the spectrometer accuracy which is 0.12 cm^{-1}, confirm that the difference induced by the deposition methods is negligible.

5.2.4 Effect of the film thickness

During this project, the thickness of the deposited a-Si was increased from 220 nm to 400 nm to optimise light coupling for the optical waveguide characterisation. The impact of this transition between generation V and generation VI will be discussed here.

It is expected that with a thicker a-Si wire, more energy is required to reach the complete melting regime. This is confirmed by the Raman maps shown in Figure 5.4. These maps indicate the measured p-Si peak position for 2 µm wide wires, which are 220 and 400 nm thick, respectively. For both of these samples, the double peak fitting method is used to take account of the c-Si substrate contribution. But when the p-Si track is damaged, only the substrate c-Si peak remains and the overall peak position suddenly shifts to the c-Si reference position, as shown in Figure 5.4(a), for laser powers that are located below the magenta line. Thus, the optical damage threshold can be obtained by searching for a Raman peak shift as shown in Figure 5.4. For both 220 nm and 400 nm thick films, the 2 cm^{-1} peak shift toward higher frequencies indicating the damaged threshold is delimited by magenta lines. Despite having different damage thresholds for the different film thickness, overall we can conclude that, with the correct power, the p-Si material quality after laser processing is similar as indicated by the Lorentzian peak widths of 3.3 cm^{-1} and 3.19 cm^{-1}. These lines were processed with 90 mW and 240 mW for the 200 nm and 400 nm thick silicon films, respectively, both with a scanning speed of 0.1 mm/s. The increase of wire thickness from 220 to 400 nm seems to only affect the different laser processing thresholds.

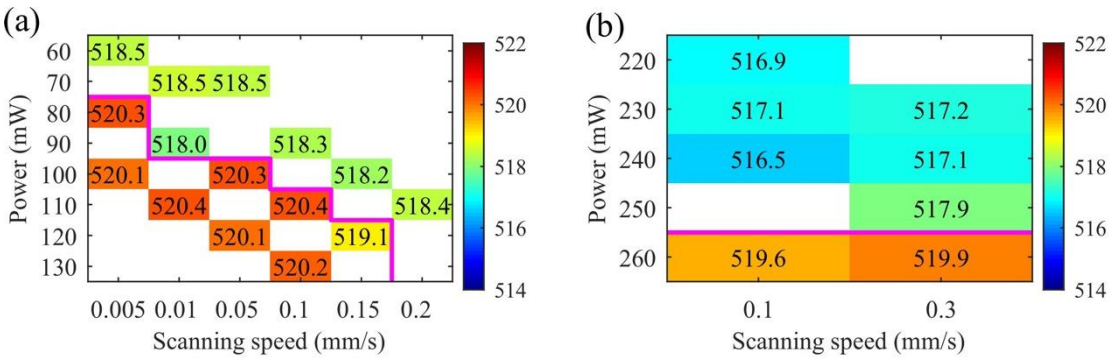

Figure 5.4: Raman peak position for a 2 µm wide, (a) 220 and (b) 400 nm thick a-Si wires for different laser processing powers. Damaged p-Si wires are situated below the magenta lines.

In Figure 5.5(a) and (b), two p-Si wires with a 2 µm width and a thickness of 220 and 400 nm, respectively, reveal the same long crystal patterns aligned with the writing direction. It is possible that with a thicker wire, more nucleation sites resulting in several small crystals could appear due to larger molten volume and larger air-cooled surfaces but from the observations in Figure 5.5, the change is negligible.

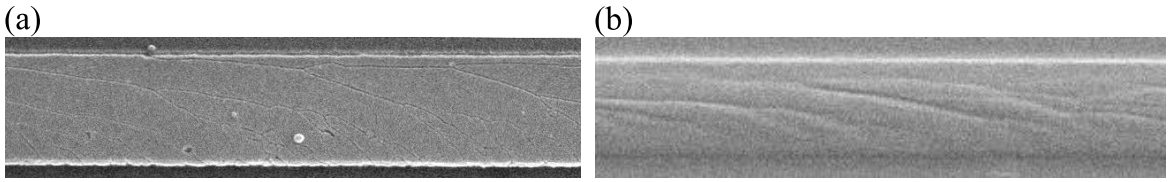

Figure 5.5: Micrographs of 2 µm wide p-Si wire with a thickness of (a) 220 and (b) 400 nm after a Secco etching treatment.

5.2.5 Effect of silica capping

During this project, different approaches have been investigated to enhance the silicon crystallisation. As crystals, up to 200 µm long have already been reported via laser processing of silicon core fibres that are completely encapsulated in silica, silicon wires of Generation IV samples have been covered with a 1 µm thick PECVD silica top layer to mimic the fibre geometry. In addition, to protecting the silicon wires from dust, the silica capping layer is also expected to allow tuning of the p-Si stress due to silicon confinement as in the corresponding fibre experiment [44]. To investigate if this result can be reproduced on a planar geometry, the pre-structured a-Si wires were laser processed using a ×10 objective at different scanning speeds and powers. Results of the Raman study are presented below for 2 µm wide wires.

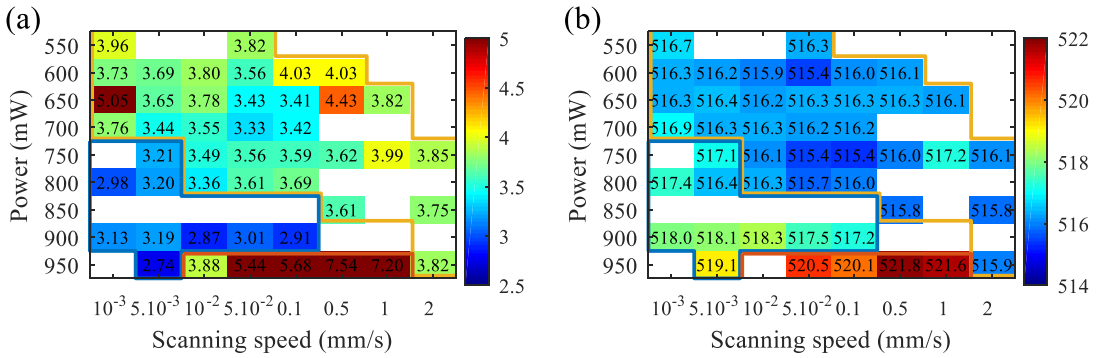

Figure 5.6: Raman maps of laser processed silica capped a-Si 2 µm wide waveguides for different scanning speeds and powers. (a) Lorentzian peak width Γ and (b) peak position.

The Raman maps in Figure 5.6 are composed of three different parts, delimited by coloured separator lines. In the areas delimited by orange lines, the a-Si wires did not receive enough energy and the p-

Si material is poorly crystallised with peak widths Γ > 3.2 and a Raman peak position shifted toward lower frequencies. As with planar laser processing, a tensile strain is imposed on the silicon by the surrounding silica when the p-Si shrinks because of its higher density compared to a-Si. In the blue delimited area, the a-Si wires received enough energy and have a high degree of crystallisation, as indicated by the Raman peak width Γ ≈ 2.8 cm^{-1}. However, in this area the p-Si doesn't show any sign of strain, as indicated by the position of the Raman peak. This is most likely due to softening of the silica capping layer during laser processing. Finally, when the a-Si wires have been exposed at higher energy, Γ becomes larger but the peak position shifts to values close to c-Si reference and even beyond, i.e. for the track processed with 950 mW at 0.5 mm/s.

The unexplained strain observed in some p-Si tracks is revealed by the optical microscope and SEM images in Figure 5.7, where partial ejection of silicon during laser processing is observed. The images (a-c) correspond to a wire laser processed with 900 mW at 0.01 mm/s and show a continuous bump in the central part with a funnel from where material escaped. The remaining silicon, not being stressed anymore by its silica cladding, has a high degree of crystallisation and a peak centred at 518.3 cm^{-1}. On images (d-e), the wire laser processed with 950 mW at 0.05 mm/s presents a larger number of funnels and the silica cladding seems to have 'collapsed' which would explain the high compressive strain observed with Raman.

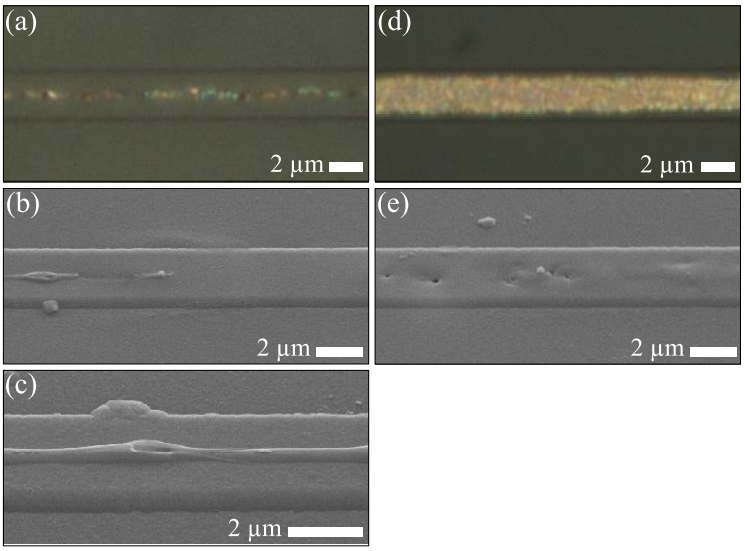

Figure 5.7: Optical microscope images and micrographs of a-Si silica capped 2 µm wide wire laser processed with 900 mW at 0.01 mm/s and laser processed with 950 mW at 0.05 mm/s, respectively (a-c) and (d-e). Samples are 45° tilted for SEM micrographs.

As with hydrogenated silicon, the silica capped project has not been investigated in more detail as the initial results, despite indicating that good material quality could be obtained, revealed that more work was needed to investigate the strain. For strain investigation, a thicker silica cladding in the

planar geometry should help to better confine silicon during the laser processing as in the case of silicon core fibre where the cladding is ~125 µm.

5.3 Silicon waveguides

The following part focuses on generation VI samples, the last generation of this project, which leverages the knowledge acquired from previous experiments and generations.

As compared to the initial test samples, used for the preliminary work, the last sample generation mainly profits from high-resolution patterning based on e-beam lithography, and a finer definition of a-Si wires from the use of the ICP-RIE etching method as shown in Figure 3.9. Although e-beam allows for wires that are 200 nm in width to be fabricated, the optical injection losses for the transmission measurements would have been too high. Furthermore, most of the 500 nm wide waveguides were broken due to vibrations during polishing and cleaning steps so we only focused on wires with widths of 2, 1.5 and 1 µm.

5.3.1 Laser processing

For the last sample generation, optimal laser processing parameters were obtained from both silicon light reflection observations and Raman spectroscopy. It is known that laser melting is accompanied by an increase of reflectivity due to the phase transition from solid to liquid silicon along with surface topography modification [168]. To observe this reflectivity transition, two photodiodes have been introduced in the laser processing along with beam splitters to collect both the back reflection of the laser from the sample surface and a portion directly from the laser output for normalisation. Traces representing reflectivity variations have been acquired but the low responsivity of the available photodiodes made the system impractical. However, during this experiment, strong correlations have been made between the visible scattered light during the process and the resulting p-Si wire shape.

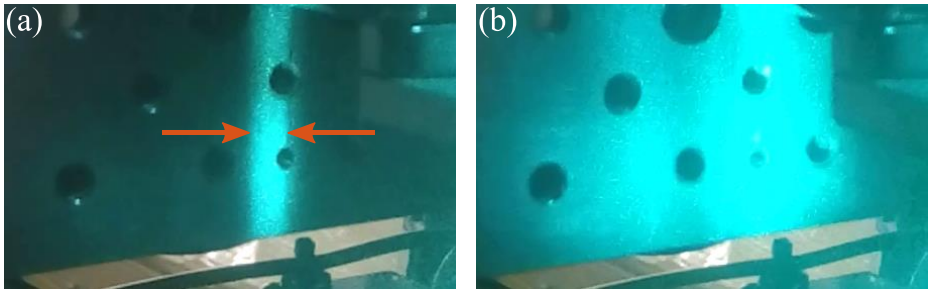

Figure 5.8: Images of the backscattered light from sample surface during laser processing. (a) Back reflection of a continuously crystallising wire, (b) scattered back reflection of a wire being damaged during the writing process.

Homogenous symmetric back scattering, as shown in Figure 5.8(a), results in a symmetrical homogeneously processed wire whilst distorted scattered light as shown in Figure 5.8(b) indicates ablation and damages. Offsets processing have also been identified using this method. The advantage of this method is that a wire damaged during laser processing can easily be identified and put aside. For safety reasons, laser goggles and anodised aluminium shielding were used to protect the lab user from laser reflections from the sample.

The back scattered method saves time and gives the opportunity to quickly converge toward optimal processing parameters but Raman spectroscopy is primarily still used to assess the p-Si quality. In addition to using the Raman peak position and width Γ, the intensity ratio I_p/I_c, between the p-Si and c-Si peaks is also taken into account. As shown in Figure 5.9(a), the Raman spectrum of a 2 µm wide waveguide laser processed with 260 mW at 0.05 mm/s has been fit using the two peak method, with the result revealing that the p-Si peak intensity is lower than c-Si peak. In this case, the p-Si material, despite having a Lorentzian width Γ of 3.05 cm^{-1}, has been ablated and the small amount of the remaining material results in a low intensity p-Si peak compared to the substrate c-Si peak. Therefore, if the ratio I_p/I_c is low, the substrate c-Si has the biggest participation and the track can be considered as damaged, as in the orange delimited area in in Figure 5.9(b). In contrast, high I_p/I_c ratios, such as delimited in magenta, indicate a non-damaged track.

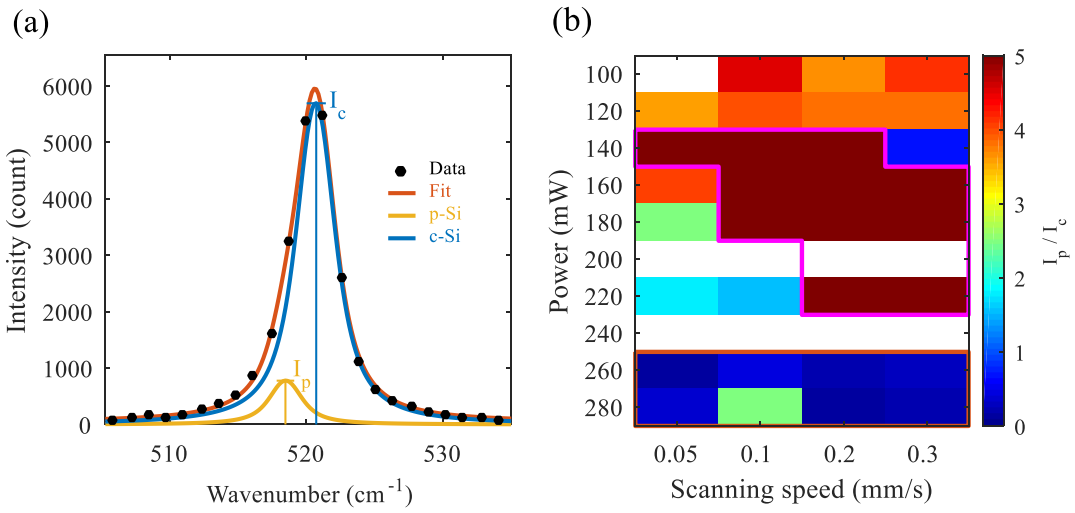

Figure 5.9: (a) Raman peak fitting using the two peaks method for a 2 µm wide wire laser processed with 260 mW at 0.05 mm/s, (b) Variations of Raman p-Si and c-Si peaks intensity ratio for a 2 µm wide wires.

The range of optimal processing parameters was obtained by combining the back scattered observations with optical microscopy and Raman spectroscopy for each wire width. Results are summarised in Table 5-1 with the damage threshold range indicated for different wire widths. Laser processing was performed using a ×10 objective to ensure beam overlap with the entire waveguide. To limit the investigation field, the scanning speed range has been mainly restricted to values of 0.1,

0.2 and 0.3 mm/s. However, for such a small range, no noticeable changes in the damage threshold were observed. For a fixed width, the damage threshold value will depend on different parameters such as the material, the local roughness, the alignment and the focus.

Wire width (µm)	Damage threshold range (mW)
2	> 200 - 220
1.5	> 250 - 260
1	> 280 - 310

Table 5-1: Laser power damage threshold for 400 nm thick wires with different widths processed at scanning speeds from 0.1 to 0.3 mm/s with a ×10 objective.

During the processing of the Raman data, it has been found that the material presenting the best degree of crystallisation was typically processed with laser powers ~20 mW below the damage threshold. These values should correspond to the near-complete-melting regime, described in Chapter 2, where all the exposed material is molten except for a small amount of solid silicon clusters that seed the growth of large crystals. However, as our Raman spectrometer system has a spot size of 1 µm diameter, it cannot evaluate the degree of crystallisation for p-Si wires with crystals larger than 1 µm. As seen in Figure 5.10, the 1.5 µm wide p-Si wire laser processed with 230 mW at 0.1 mm/s has a Γ of 2.8 cm^{-1} which is close to c-Si reference, albeit with a small shift in the peak position.

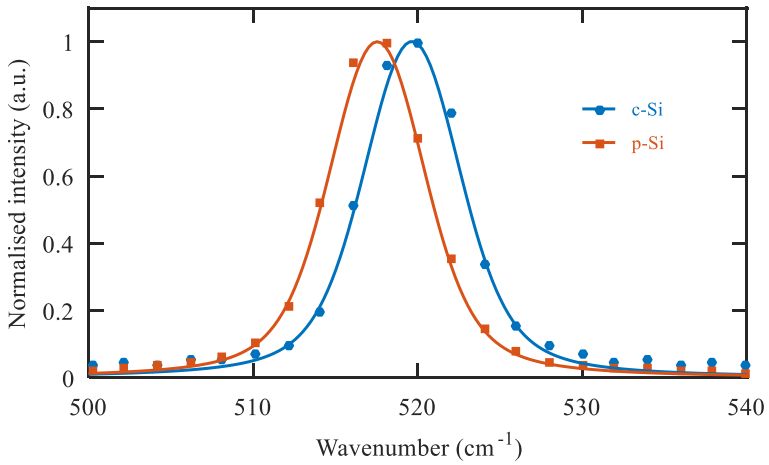

Figure 5.10: Raman spectra of a 1.5 µm wide a-Si wire laser processed with 230 mW at 0.1 mm/s (orange) and a c-Si reference (blue). For p-Si peak, $\Gamma = 2.8\ cm^{-1}$.

To further characterise the crystallisation degree of our p-Si wires, Secco etching, SEM and XRD characterization was also used.

5.3.2 SEM topography of p-Si wires

As seen in Chapter 3, Secco etching is an efficient way to reveal the presence of crystals when combined with SEM imaging. As chemical etching is a destructive tool, the samples that are investigated using this method cannot be used for waveguiding experiments afterwards.

Different crystallisation patterns are shown in Figure 5.11. The first wire has been laser processed with a small amount of energy, 50 mW at 0.04 mm/s. The material quickly reached the nucleation temperature whilst cooling down, resulting in the creation of numerous nucleation sites forming many small crystals, as explained in Chapter 2 with Figure 2.4. Also, as the edges cool faster because of their higher exposition to air, smaller crystals are formed in these regions.

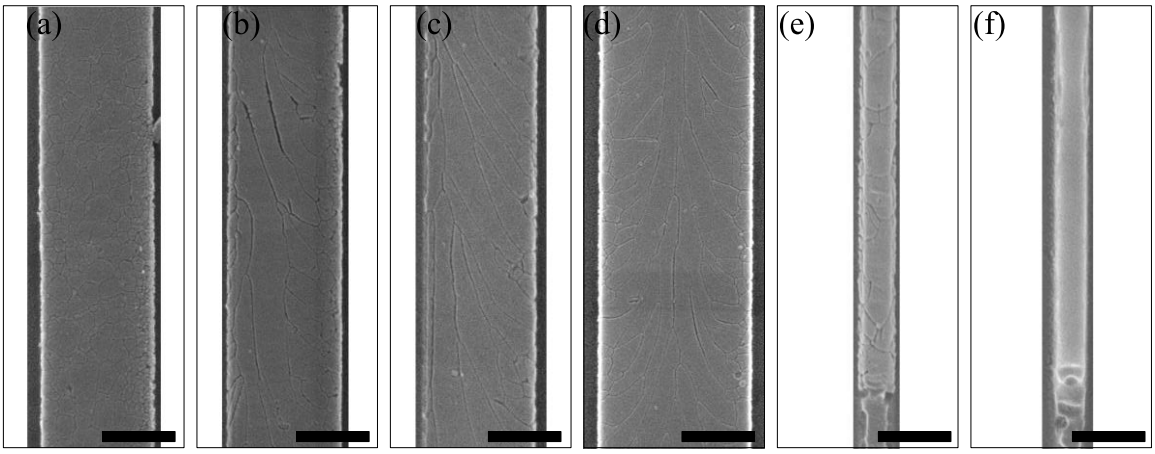

Figure 5.11: SEM micrographs of Secco etched p-Si wires with different topographies. (wire width, processing power, scanning speed) (a) 1.5 µm, 50 mW, 0.04 mm/s, (b) 1.5 µm, 60 mW, 0.02 mm/s, (c) 1.5 µm, 80 mW, 0.05 mm/s, (d) 2 µm, 110 mW, 0.04 mm/s, (e) 0.5 µm, 250 mW, 0.01 mm/s, (f) 0.5 µm, 300 mW, 0.01 mm/s. [scale bars: 1 µm]. Scanning direction from the bottom to the top.

In Figure 5.11(b), the track was laser processed with more energy, 60 mW at 0.02 mm/s, thus the liquid phase of silicon reached a higher temperature. Again, because sides are more exposed to air, they cool down faster to reach the nucleation temperature first. Small crystals then form on the edges and some of them seed the liquid phase of silicon in the middle part leading to the formation of larger crystals in this region. The wire in Figure 5.11(c) has been laser processed with more energy than the previous one, 80 mW at 0.02 mm/s, and the explanation of the crystallization remains identical. However, one can observe a shrinkage of the small crystal zone close to the edges, which implies the formation of larger crystals in the central region. Figure 5.11(d) and (e) show that these different crystallisation patterns can be observed with different wire widths if the laser power is adjusted accordingly. Note in (d) a “chevron” pattern is left by the laser scanning from the bottom to the top, with a long crystal forming in the central part of the wire where the silicon remains liquid for the longest time. Despite having many small crystals on their sides, these patterns are useful for the

understanding of crystallisation mechanism. Finally, the crystallisation patterned in Figure 5.11(f) has been observed mainly for 1 and 0.5 µm wide wires. The fact that no cracks can be observed along this wire after Secco etching indicates that it is composed of one crystal over the entire width of the wire.

This crystallisation study indicates that the largest crystals are obtained when the silicon wire is completely melted. This study also explains why materials with the highest degree of crystallisation are obtained for laser powers close to the threshold.

5.3.3 Waveguide reshaping

Another consequence of the complete melting that the wires are subjected to is that, while in the liquid phase, the wire is reshaped by surface tension that acts on the liquid air interface. Therefore, as it cools down, the initially rectangular cross section of the a-Si wire forms a semi-circular shape, as shown in Figure 5.12. Here, the SEM micrograph in (a) is an un-processed 2 µm wide a-Si wire, whilst the SEM micrograph in (b) is a 2 µm wide p-Si wire which has been laser processed with 200 mW at 0.1 mm/s. In addition to removing the sharp corners, the reshaping smooths any potential side roughness left after the patterning step, which is important for obtaining low waveguide losses. In Figure 5.12(b), debris from the polishing step can be observed. These debris are problematic for the loss measurements because it can cause light scattering and also interfere with the laser processing by introducing absorption points that can initiate laser damage. Later on we opted for covering some samples with a 1 µm thick silica layer after laser processing to keep them free of dust. A post silica-covered sample is shown in Figure 5.12(d), but no measurements have been obtained from these due to a material issues occurring during the deposition (wrong deposition temperature and material contamination during silica top layer deposition). Still, even if the effective index of this structure is different due to the presence of the top layer, material losses are expected to be similar and silica covered silicon wires are expected to be one of the future targets of this project as we work towards 3D stacking of the waveguides.

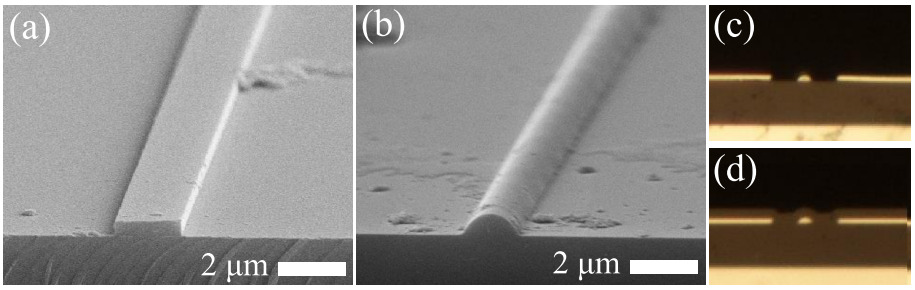

Figure 5.12: SEM micrographs of (a) an a-Si wire before processing and (b) a p-Si wire after processing at 0.1 mm/s with 200 mW. (c-d) Optical microscope cross-section of a p-Si wire without and with a silica cover.

5.3.4 X-Rays Diffraction analysis

XRD is a tool that can be used to assess the presence of crystals in the laser processed wires and collect information about individual crystals such as their length and orientation, whilst having the advantage of being a non-destructive method. To characterise our p-Si wires, the XRD setup was used in a grazing incidence configuration to avoid strong diffraction from the c-Si substrate. As illustrated in Figure 5.13, XRD analysis was performed by collecting the diffraction pattern from a large incident spot, 30 µm by 3 µm, for different scanning positions along the p-Si wire.

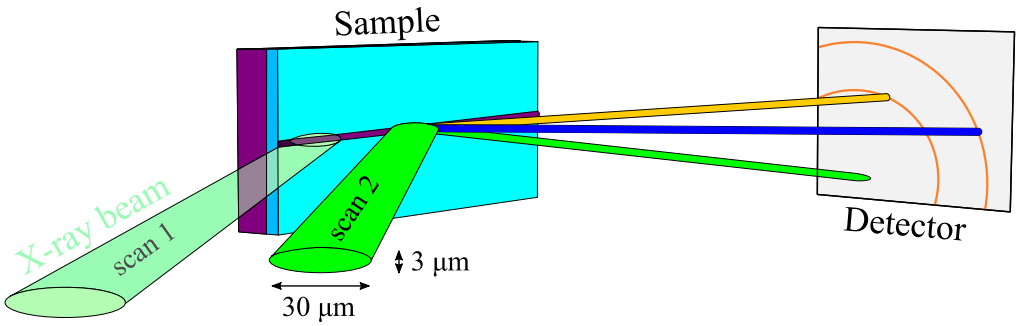

Figure 5.13: Illustration of the XRD experiment in reflection configuration. A large X-ray beam is scanned at different position of the silicon wire in grazing incidence. For each scan, the yellow and blue diffracted beams are collected by the CCD detector along with the reflected green X-ray beam.

The diffraction pattern of a 2 µm wide p-Si wire processed with 200 mW at 0.1 mm/s is shown in Figure 5.14. The scanned segment of this wire is not a single crystal as several diffracted spots can be observed. The two broad spots on the ⟨311⟩ and ⟨400⟩ silicon reference planes, indicated by red arrows, are the c-Si substrate diffraction with a measured azimuthal angle difference of 23.42° degree. In theory, for a diamond unit cell, the calculated angle difference between ⟨311⟩ and ⟨400⟩ crystallographic planes is 25.24°, thus confirming the c-Si substrate origin of these broad spots. Smaller spots can also be observed and are indicated by blue and green arrows. The spots indicated by blues arrows are positioned next to a c-Si plane and are associated with p-Si crystals, whilst the spot indicated by the magenta arrow is too far from a c-Si plane to be associated with a silicon signal, this is considered as an artefact or noise. Finally, a close-up view of the brightest spot indicated by a green arrow is shown in the inset of Figure 5.14, where the straight line corresponds to the crystalline silicon reference and the dashed line corresponds to the centre of the diffraction spot. As the d-space values of the ⟨220⟩ plane and the diffracted spot are 1.92017 Å and 1.9156 Å, respectively, these measurements indicate a compressive strain, which would correspond to a Raman peak position beyond 520 cm^{-1}. This result, being in opposition with our previous Raman conclusion, is attributed to the lack of precision of the XRD for the configuration that we used. To see more Debye cones on the detector, we reduced the distance between the sample and the detector, thus sacrificing the

precision of the instrument. Therefore, because of the large error for d-space measurements, no stress analysis will be performed with the XRD results.

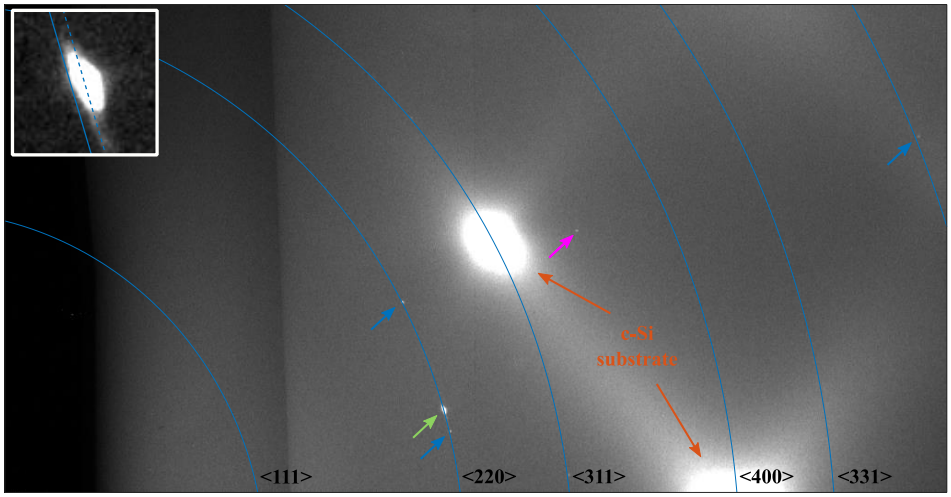

Figure 5.14: X-ray diffraction pattern of a p-Si wire with crystalline Debye's cone sections indicated by the blue lines. Diffraction spots are shown by blue and green arrows, green for the brightest. An artefact spot is indicated by the magenta arrow and the two broad spots correspond to c-Si substrate diffraction. Inset: brightest spot close-up.

To measure the length of this crystal, diffraction patterns were recorded at different positions along the p-Si wire with steps of 200 µm, as shown in Figure 5.13. For each step, the position and intensity for each visible spot were recorded and presented as shown in Figure 5.15. The map presented in (a) reports the 26 spots identified during the 3.8 mm long scanning of a 2 µm wide p-Si wire processed with 200 mW at 0.1 mm/s. Along this scanning, no single crystal sections have been identified as there is always more than one crystal detected per scan. However, some diffraction spots have been detected for several consecutive steps indicating the presence of long crystals. The intensity profiles of such crystals along the wire are shown in Figure 5.15(b). Crystal 7, in green, has an estimated length of 1.6 mm whilst crystal 17, in blue, has a length of 1.8 mm. Despite being polycrystalline, the presence of these long crystals in the p-Si wire drastically decreases the number of crystal boundaries, which we expect to result in reduced scattering losses during light propagation.

These XRD measurements also provide information about the crystallographic orientation of the grains under study. It has been reported that during a-Si crystallisation on a SiO_2 surface, ⟨100⟩ is the preferred crystal orientation for silicon films thinner than 0.5 µm in a complete melt regime as the Si-SiO_2 interfacial free energy is the lowest for this orientation [169]. Unfortunately, because of the symmetry of crystalline silicon diamond structure, the diffraction from ⟨100⟩ planes cannot be observed [170]. However, from the analysis of the different d-spaces identified in the p-Si grains reported in Figure 5.16, there is no preferential orientation. In fact, most spots are observed on the ⟨311⟩ and ⟨220⟩ planes, including the two longest crystals 7 and 17, respectively. For planes

associated with shorter d-spaces, the observable portion of the Debye's cone being smaller, less spots can be measured. Also, for that particular experiment, the available sample holder used in grazing incidence was obstructing the ⟨111⟩ Debye cone as seen in Figure 5.14. Hence, the ⟨111⟩ oriented crystals cannot be detected. Finally, crystals 3, 10 and 11 can be set aside as they are too far from a plane reference to be associated with silicon crystal and are therefore considered as artefacts or noise.

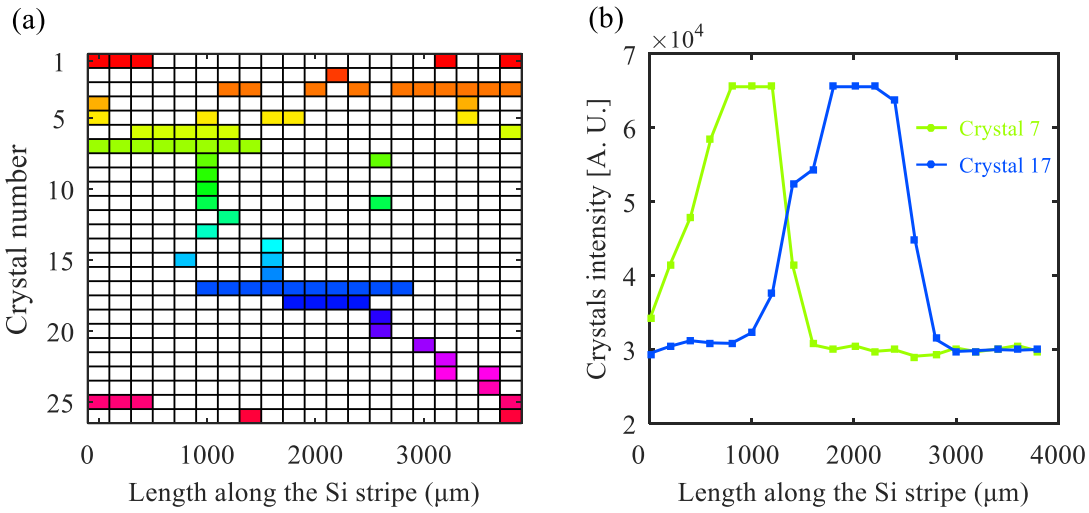

Figure 5.15: (a) Map of crystals detected along the p-Si wire. (b) Intensity of crystals 7 and 17 during the scanning along the p-Si wire .

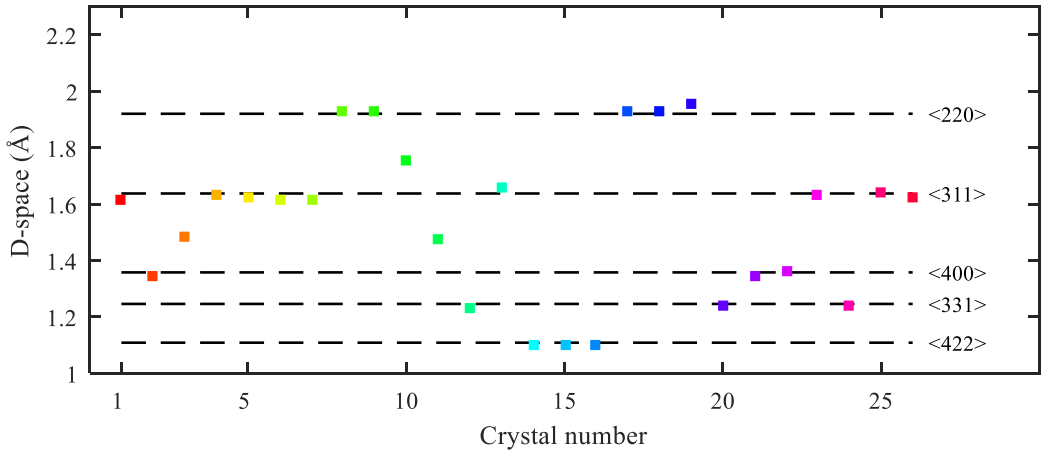

Figure 5.16: D-space associated to the crystals tracked during the scan along the p-Si wire. Crystals 3, 10 and 11 are either artefacts or noise.

5.3.5 Waveguide propagation loss measurements

From the Generation VI samples, many laser processed wires presenting different material qualities have been studied within this chapter. However, propagation loss measurements are quite sensitive

to defects such as scratches, debris or discontinuities. Furthermore, the polishing process requires many manipulations of the sample, along with chemical treatments for cleaning etc., which increase the chances of depositing debris on the sample surface or scratching the waveguide facet. For these reasons, only few p-Si waveguides were deed to guide sufficient light for transmission measurements. Both cut-back measurements and Fabry-Pérot interferometer measurements have been used to estimate the propagation losses in the p-Si wires. The different results obtained with each method are presented and discussed hereunder.

The cut-back measurements of the most optimised p-Si tracks are presented in Figure 5.17. These two ridges presented high material quality assessed by Raman spectroscopy with peak widths Γ of 2.93 and 2.80 cm^{-1} for the 2 and 1.5 µm wide tracks, respectively. For each waveguide, the overall losses were measured using Equation (3-7) for lengths of 8.1, 7.2 and 5.1 mm. After each polishing step, both facets of the waveguides were checked using an optical microscope, as shown in Figure 5.12(c) to ensure that no debris was blocking the light injection or collection ports. The data points are then fit with a linear line. The y-intercept provides information about the injection losses and the slope indicates the propagation losses of the waveguide. The 2 µm wide wire laser processed with 180 mW at 0.05 mm/s has propagation loss of 6.23 dB/cm with injection losses of 41.3 dB, whilst the 1.5 µm wide wire processed with 230 mW at 0.1 mm/s has propagation losses of 5.31 dB/cm with injection losses of 29.3 dB. The high injection loss is caused by a mixture of the Fresnel reflection, which represents 33% of the input power, the facet quality and the mode mismatch, with only 14% and 11% overlap between the spot of the 0.85 NA coupling objective and the TE_{00} mode of a 2 and 1.5 µm wide wire, respectively. Still, the losses in our waveguides are considerably lower than other CMOS compatible laser processed polycrystalline waveguides, which have presented losses on the order of 20 dB/cm [38].

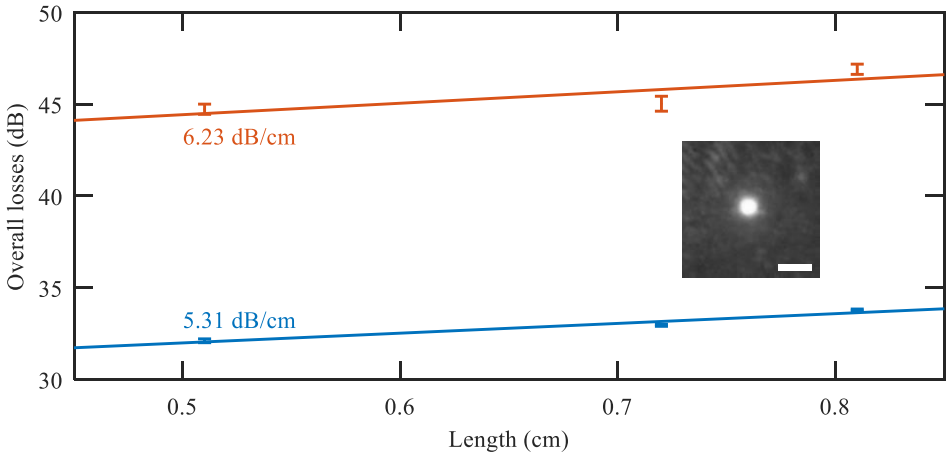

Figure 5.17: Cut-back loss measurements of 2 and 1.5 µm wide p-Si wires, respectively orange and blue. Inset: far field output mode of a 2 µm wide wire observed with an IR camera. Scale bar: 4 µm.

The inset in Figure 5.17(b) shows the output mode from a 2 µm wide waveguide, in the far-field, collected with an IR camera. The spot has a circular shape, coherent with the waveguide reshaping, and given the low resolution of the collection microscope objective. Also, only a negligible amount of light can be seen in the BOX layer, indicating a strong light confinement with no leakage into the cladding.

As the cut-back method for waveguide losses is time consuming and risky, as the polishing step can easily damage the waveguides which are not silica capped, another loss measurement method has been used to estimate propagation losses. As discussed in Chapter 3, the Fabry-Pérot method for loss measurements is based on the contrast of the fringes induced by the resonance of light in a medium between two mirrors. Using the Fabry-Pérot setup illustrated in Figure 3.25, a c-Si reference waveguide, 2 µm wide and 400 nm thick, has been used for calibration as shown in Figure 5.18.

Fringes for both TE and TM modes clearly appear and by measuring the maxima and minima of different fringes, propagation losses of 1.45 dB/cm for TE and 2.22 dB/cm for TM are calculated using Equation (3-9), with n=3.45 for the c-Si refractive index value and 1.25 cm the length of the waveguide. When measured with the cut-back method, propagation losses for the TE mode are 1.72 dB/cm, which are close to our measurements and validate the use of the Fabry-Pérot method for quick loss estimations.

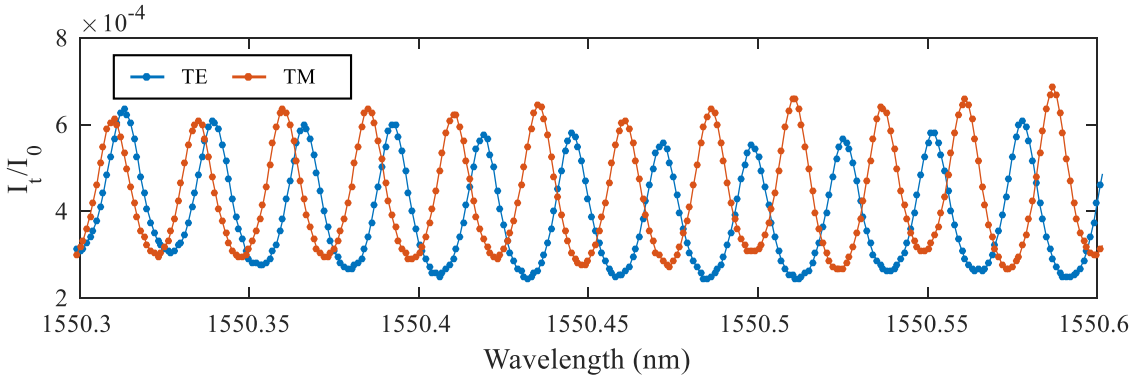

Figure 5.18: Fabry-Pérot fringes for a c-Si waveguides measured with both TE and TM polarisations.

The Fabry-Pérot measurements with TE polarised light in a 1.5 µm wide p-Si wire crystallised with 250mW at 0.1mm/s is shown in Figure 5.19. As with the c-Si Fabry-Pérot trace, fringes can be observed, but as the material has higher loss, the contrast is lowered. To ensure the fringes correspond to the waveguide resonance, the free-spectral range (FSR) of the waveguide, corresponding the period of the Fabry-Pérot fringes, can be measured and compared to its theoretical value defined as:

$$\Delta\lambda_{FSR} = \frac{\lambda^2}{2\,L\,n_g}, \tag{5-1}$$

with L the length of the waveguide and n_g the material group index. For n_g we used 3.59, the c-Si value, which might bring a negligible difference with p-Si [60]. Using the length of the waveguide, 0.88 cm, the calculated FSR is 39.28 pm whilst measurements on the graph indicate 32.8 pm. This small difference, which partially originate from the material differences between c-Si and p-Si, confirm that the observed fringes correspond to our waveguide. From this measurement, propagation losses for the TE polarisation are estimated to be 5.12 dB/cm. Despite being lower than the previous losses measured from cut-back measurements, we consider these Fabry-Pérot results as confirmation of the losses estimated via-cut-back.

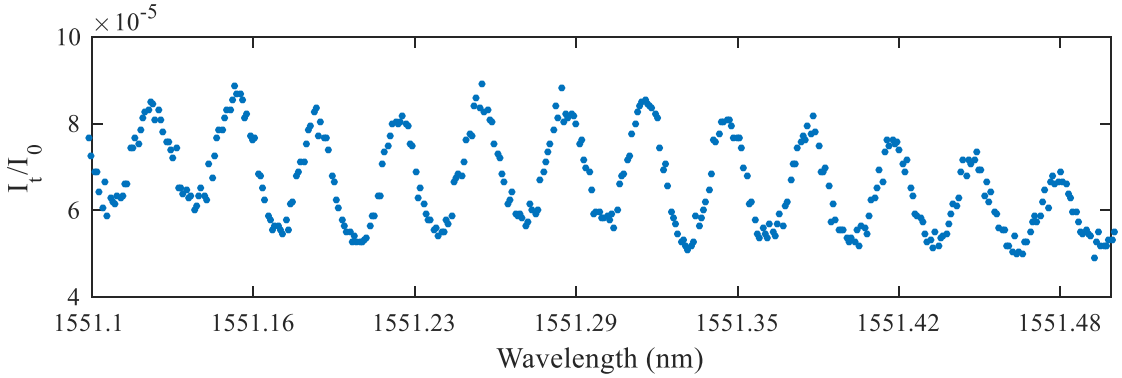

Figure 5.19: Fabry-Pérot fringes for a p-Si waveguides measured in TE polarisations.

One of the problems with using the Fabry-Pérot method is that if multiple modes are present, each mode will have a different FSR, and thus the fringes of each mode will super-impose resulting in a distorted trace. To establish whether our waveguides were multimode, simulations were performed using Comsol software. To take the reshaping of the p-Si waveguide into account, the waveguide cross-section is defined as a half circle with an area equal to the cross-section area of the as-deposited wire. Using the refractive index of c-Si, 3.45, and silica, 1.45, for the simulation, the different guided modes have been computed and are represented in Figure 5.20 for waveguide widths of 2, 1 and 0.5 µm. The TE mode with electric field polarised horizontally is the fundamental mode of the waveguide, followed by a TM mode polarised vertically. The larger overlap of higher modes with the waveguide walls induce higher losses due to light scattering. Also, in the case of the 0.5 µm wide waveguide, the last mode is not guided in the waveguide but in the BOX layer as the effective index n_{eff} is close to glass. Finally, even though the initial rectangular shape of the wire before laser processing is expected to favour TE over TM polarisation, due the increased scattering of the TM mode with the top wire surface, no preferential polarisation has been observed after wire reshaping. With the reshaped wire, TE and TM seem to equally interact with waveguide walls. Therefore, a polariser has to be used during measurements to select either TE or TM modes. The higher modes

being lossier due to their lower mode index, TE_{00} and TM_{00} are the dominant modes in these waveguides.

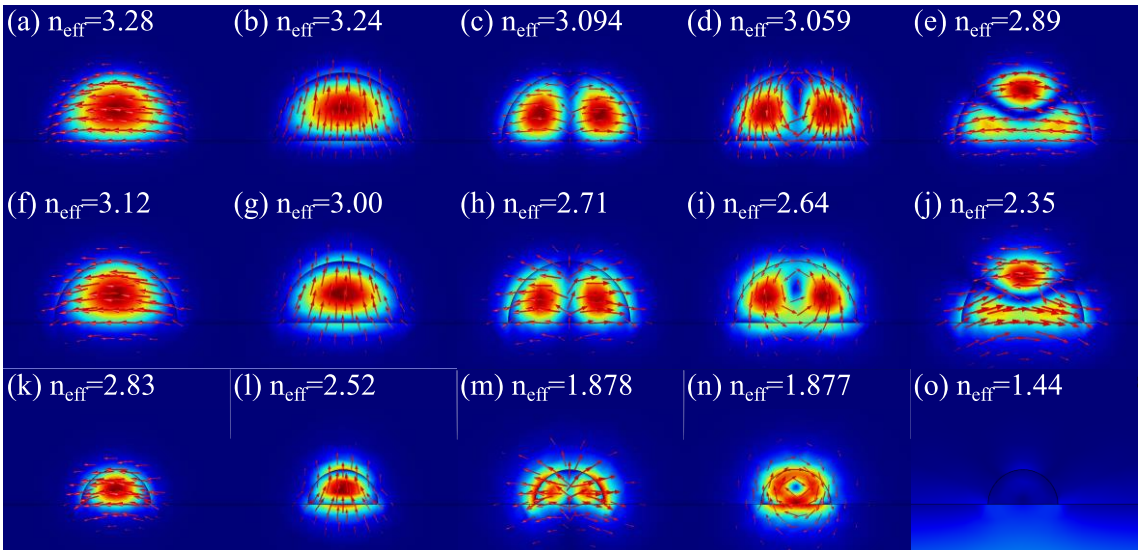

Figure 5.20: Numerical simulations of the guided modes in p-Si waveguides for width of 2, 1 and 0.5 µm, respectively (a-e), (f-j) and (k-o). Red arrows represent the electric field.

5.3.6 Nonlinear loss measurements

Before presenting the results of the nonlinear propagation experiments, the nonlinear properties of silicon when using high intensity optical pulses will be briefly explained to introduce concepts such as two-photon absorption and nonlinear refraction. I will then introduce the nonlinear Schrödinger equation which describes propagation under these effects.

5.3.6.1 Brief introduction to nonlinear optics in silicon

When a high power electromagnetic field propagates through silicon, the local properties of the material are modified. The electric field modifies the electron distribution around the atomic core therefore inducing a polarisation field. The polarisation field is typically formulated as a power series expansion [171][172]:

$$\mathbf{P}(\mathbf{r},t) = \varepsilon_0 \left(\chi^{(1)}\mathbf{E} + \chi^{(2)}\mathbf{EE} + \chi^{(3)}\mathbf{EEE} + \cdots\right), \tag{5-2}$$

with $\chi^{(n)}$ the n^{th} order susceptibility whose value decreases for higher orders.

The first order $\chi^{(1)}$ is the linear susceptibility and is the dominant contribution to **P**. The real part of $\chi^{(1)}$ is related to the medium refractive index n and its imaginary part to the attenuation coefficient α by the relations:

$$n(\omega) = 1 + \frac{1}{2}\,\mathbf{Re}\left(\tilde{\chi}^{(1)}(\omega)\right), \tag{5-3}$$

$$\alpha(\omega) = \frac{\omega}{n\,c}\,\mathbf{Im}\left(\tilde{\chi}^{(1)}(\omega)\right), \tag{5-4}$$

with $\tilde{\chi}^{(1)}(\omega)$ the Fourier transform of $\chi^{(1)}(t)$.

The second order susceptibility $\chi^{(2)}$ is responsible for nonlinear effects such as second harmonic generation and sum frequency generation. However, in centrosymmetric materials such as crystalline silicon, as a reversal of the electric field does not imply a reversal of the induced polarisation **P**, even ordered susceptibilities vanish [171].

The third order susceptibility $\chi^{(3)}$ is non-zero in silicon and is responsible for two important nonlinear dynamics: two-photon absorption (TPA) and nonlinear refraction. Both of these nonlinear dynamics are related to $\chi^{(3)}$ by the coefficients β_{TPA} and n_2 for TPA and nonlinear refraction, respectively, as follows:

$$\beta_{TPA} = \frac{3\omega}{2\varepsilon_0 c^2 n_0}\,\mathbf{Im}\left(\chi^{(3)}\right), \tag{5-5}$$

$$n_2 = \frac{1}{c\varepsilon_0 n_0^2}\,\frac{3}{4}\,\mathbf{Re}\left(\chi^{(3)}\right). \tag{5-6}$$

5.3.6.2 Nonlinear absorption

Two-photon absorption is a nonlinear effect which is particularly strong in semiconductors. This phenomenon happens when two photons, with the sum of the photon energies exceeding the band gap energy, are absorbed by an electron from the valence band. The transition of this electron from the valence band to the conduction band is assisted by a phonon due to the indirect band gap in silicon. If both photons have the same energy, this phenomenon is known as degenerated TPA and if the absorbed photons have different energies, this is non-degenerated TPA as shown in Figure 5.20. In this thesis, only a single pump laser is injected into the waveguides, hence no non-degenerated TPA can be observed but this phenomenon is common when both pump and signal are used.

In the case of degenerated TPA, the intensity dependence of the degenerated TPA can be expressed by [173]:

$$\frac{dI}{dz} = -\beta_{TPA}\,I^2(z,t)\,, \tag{5-7}$$

with the optical intensity related to the amplitude of the optical pulse by: $I(z,t) = |A(z,t)|^2/A_{eff}$ were $A(z,t)$ is the pulse amplitude pulse and A_{eff} the mode effective area defined in Chapter 2.

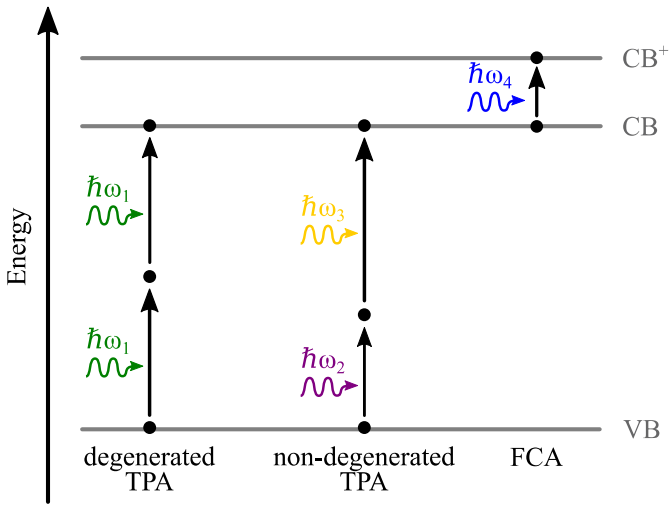

Figure 5.21: Energy-level diagram for different nonlinear absorption mechanisms.

Once an electron is in the conductive band, another absorption mechanism can be observed: the free-carrier absorption (FCA). A photon is absorbed by an electron in the conduction band, raising it to a higher energy level as shown in Figure 5.20. This TPA-induced intra-band absorption phenomenon modifies the optical intensity as follows:

$$\frac{dI}{dz} = -\beta_{TPA} I^2(z,t) - \sigma_{FCA} N(z,t) I(z,t) \ , \tag{5-8}$$

where σ_{FCA} is the FCA cross-section and $N(z,t)$ is the carrier density, which depends on the initial doping level of the silicon but also on β_{TPA} which brings free carriers in the conductive band. The carrier density is determined by the rate equation [174]:

$$\frac{\partial N(z,t)}{\partial t} = \frac{\beta_{TPA}}{2h\nu} I^2(z,t) - \frac{N(z,t)}{\tau_c} \ , \tag{5-9}$$

where $h\nu$ is the pump photon energy and τ_c is the carrier lifetime.

5.3.6.3 Nonlinear refraction

The second nonlinear phenomenon introduced by the third order susceptibility $\chi^{(3)}$ is the nonlinear refraction, also known as the optical Kerr effect. The nonlinear refractive index n_2 is at the origin of different nonlinear mechanisms such as the self-phase modulation (SPM), cross-phase modulation, third harmonic generation and four-wave mixing. For this thesis, only SPM will be described as cross-phase modulation requires both pump and signal beams to be present, and third harmonic generation and four-wave mixing are not efficient enough phenomena to be observed, unless extreme care is taken for phase matching.

SPM is a consequence of the intensity dependence of the refractive index as shown in Equation (5-10). The modification of the material refractive index introduces a variation of the pulse phase during the propagation causing a frequency chirp. New frequency components are continuously generated during the pulse propagation leading to a spectral broadening [175].

$$n(I) = n_0 + n_2 I \,. \tag{5-10}$$

5.3.6.4 Nonlinear Schrödinger equation (NLSE)

When a short pulse propagates within a waveguide, the evolution of this pulse can be described by a nonlinear partial differential equation derived from Maxwell's equations: the nonlinear Schrödinger equation (NLSE). This equation combines both nonlinear absorption and nonlinear refraction effects. In a semiconductor like silicon, the propagation of an optical pulse in a waveguide is governed by [174]:

$$\frac{\partial A(z,t)}{\partial z} = -i\frac{\beta_2}{2}\frac{\partial^2 A(z,t)}{\partial t^2} + i\gamma|A(z,t)|^2 A(z,t) - \frac{1}{2}(\sigma+\alpha)A(z,t) \,. \tag{5-11}$$

β_2 is the GVD and represents the overall dispersion, whilst the nonlinear coefficient γ represents the magnitude of the $\chi^{(3)}$ nonlinear interaction and is defined by:

$$\gamma = \frac{k_0\, n_2}{A_{eff}} + i\frac{\beta_{TPA}}{2\, A_{eff}} \,. \tag{5-12}$$

Finally, the attenuation coefficient α represents the linear losses of the waveguide and σ, the free carrier contribution term, is defined as $\sigma = (\sigma_{FCA} + i2k_c k_0)N(z,t)$ [174]. Here, k_c is the dispersion coefficient of the free carriers.

Within our group, a simulation script has been developed to calculate the amplitude of a high intensity pulse propagating in a silicon waveguide while taking account for the different nonlinear dynamics [50]. The first step consists in obtaining the β_{TPA} coefficient by solving a reduced version of Equation (5-11) where the effect of the dispersion is ignored given the short propagation length in our sample (below 1 cm). This reduced NLSE is [50]:

$$\frac{dI(z,t)}{dz} = -\beta_{TPA} I^2(z,t) - \alpha\, I(z,t) - \sigma_{FCA} N(z,t) I(z,t) \,, \tag{5-13}$$

with $I(z,t) = A^2(z,t)/A_{eff}$.

The second step of the script consists in solving the full NLSE using the estimated β_{TPA} coefficient and using the nonlinear refractive index n_2 as the free parameter. This last part is based on split Fourier transform where every half step, the linear and nonlinear contributions to the pulse are applied in the frequency and time domain, respectively [176].

5.3.6.5 Nonlinear loss measurements

The setup used for nonlinear measurements is illustrated in Figure 5.22. To achieve the high optical intensities that are necessary to observe nonlinear dynamics, a pulsed laser with up to 55 mW of average power, centred at 1540 nm and emitting 750 fs long hyperbolic secant pulses at a repetition rate of 40 MHz was used as the pump source in the setup. The output signal was monitored as a function of input power either by measuring it with a powermeter, to determinate the waveguide β_{TPA}, or via an optical spectrum analyser (OSA) to observe spectrum broadening caused by SPM.

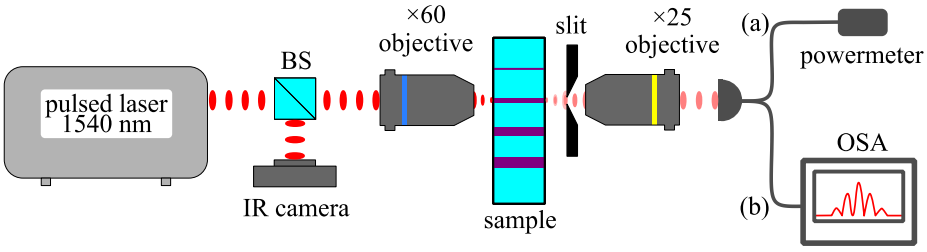

Figure 5.22: Experimental setup for nonlinear loss measurements using a pulsed laser. The powermeter path was used for β_{TPA} measurements (a) and the optical spectrum analyser was used for SPM measurements (b).

Experimental data used for the measurement of the β_{TPA} coefficient are presented in Figure 5.23. These measurements were obtained from a 2 μm wide wire processed with 200 mW at 0.1 mm/s. Here we must note that due to a cut-back polishing accident, the waveguide used for nonlinear measurements was fractured before optical loss was properly estimated. However, as this waveguide had been fabricated using identical conditions to the 2 μm wide waveguide presented in Figure 5.17, a similar loss value is expected. Additionally, in the first cut-back measurement, the overall loss of this waveguide was measured to be 31.17 dB, which suggests that both injection and propagation losses could be lower for this particular waveguide.

For the numerical simulation we used 15.5 dB and 6 dB/cm for the entry facet injection losses and propagation losses, respectively, and the length of the sample was fixed to 0.96 cm. Also, using c-Si silicon values, the FCA cross-section σ_{FCA} has been set to 1.45×10^{-21} m^{-2} and the carrier lifetime τ_c to 1 ps. Finally, using the Comsol simulations presented in Figure 5.20, the effective mode area for this waveguide has been calculated as $A_{eff} = 0.35 \times 10^{-12}$ m^2. The simulation in Figure 5.23 reveals the best fit value of $\beta_{TPA} = 7 \times 10^{-12}$ m/W.

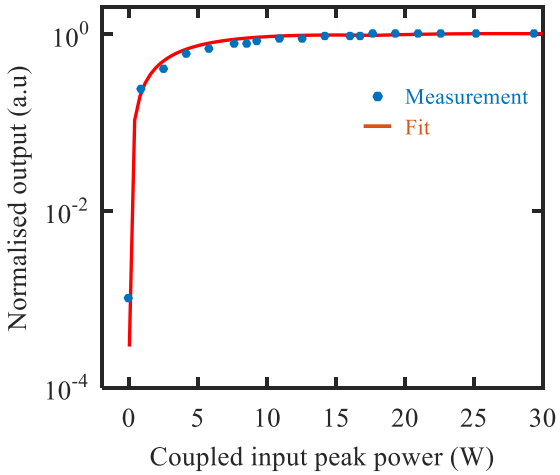

Figure 5.23: Nonlinear absorption measurements and fitting for a 2 µm wide p-Si wire processed with 200 mW at 0.1 mm/s. Normalised output power as a function of the coupled input peak power.

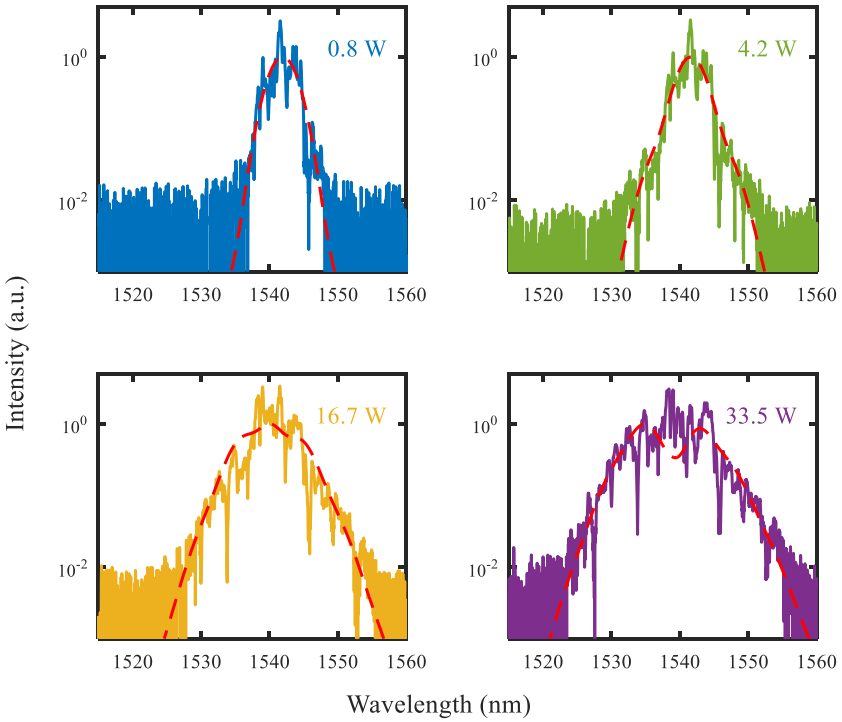

Figure 5.24: Self-phase modulation measurements and fitting for a 2 µm wide p-Si wire processed with 200 mW at 0.1 mm/s. Spectral evolution as a function of the coupled input peak power.

For the nonlinear refraction measurements, the same waveguide has been used and the output spectra obtained with different coupled input peak powers are presented in Figure 5.24. For the simulations, the full NLSE has been used with the β_{TPA} value previously obtained, the dispersion coefficient of

the free carriers k_c fixed to 1.35×10^{-27} m^3 [177] and the GVB β_2 has been estimated to be ~0.6 ps^2/m [178] whilst β_3 is set to 0 as its effect is negligible for such short propagation distance. Despite being noisy due to the higher propagation losses than c-Si material, spectral broadening is clearly visible and the fittings are in good agreement with the experimental data. The best fit value corresponds to a nonlinear refractive index $n_2 = 4.8 \times 10^{-18}$ m^2/W.

In order to compare these results to the literature, a nonlinear figure of merit of the waveguide is usually calculated as follows:

$$FOM_{NL} = \frac{n_2}{\beta_{TPA}\,\lambda}\,. \tag{5-14}$$

The FOM_{NL} defines the material efficiency of a waveguide for nonlinear interactions when both nonlinear refraction and absorption are present. When compared to results already published on c-Si reported in Table 5-2, our low-temperature deposited p-Si wire FOM_{NL} is situated within the average, hence suggesting high quality material.

Material	β_{TPA} (m/W)	n_2 (m^2/W)	FOM_{NL}	Reference
c-Si	7.9×10^{-12}	4.5×10^{-18}	0.37	[179]
c-Si	8.8×10^{-12}	4.3×10^{-18}	0.32	[179]
c-Si	4.5×10^{-12}	6×10^{-18}	0.86	[180]
c-Si	9×10^{-12}	7×10^{-18}	0.55	[181]
p-Si	7×10^{-12}	5×10^{-18}	0.44	[46]
p-Si	7×10^{-12}	4.8×10^{-18}	0.45	This work

Table 5-2: Comparison of nonlinear coefficients for silicon with previous works.

5.4 Improvement of as-deposited p-Si material

In parallel with this project, a collaborative work has been conducted with Dr Harold Chong's group to enhance the material properties of a p-Si material deposited by HWCVD. A crystalline silicon substrate was covered by a 2 µm thick BOX layer deposited by PECVD. Then, a 220 nm thick layer of p-Si was deposited at low temperature using a HWCVD system with the recipe presented in Table 5-3. Finally, the film was patterned into 400 nm wide silicon wires using e-beam and RIE with fluorine-based chemistry [182]. The samples were then covered with a 1 µm thick silica layer prior to optical measurements.

Temperature (°C)	360
Pressure (mbar)	0.024
SiH_4 Flow (sccm)	6
H_2 Flow (sccm)	294
Deposition Rate (nm/s)	0.06

Table 5-3: Recipe used for the deposition of p-Si using a HWCVD reactor.

Following fabrication, these waveguides were measured using a transmission setup and results indicated propagation losses as high as 16.9 dB/cm. Prior to any future application, these losses need to be reduced thus laser processing has been considered.

As for the a-Si wires, different laser processing powers were tested for the p-Si waveguides whilst maintaining the scanning speed at 0.2 mm/s. Using a ×20 microscope objective for the laser processing, the optimal condition for material improvement was observed for 90 mW of laser power. Then, the p-Si wires were characterised using Raman spectroscopy, with the results being fit with the two peak method to separate the p-Si peak from the c-Si substrate peak. These results are presented in Figure 5.25. The unprocessed material Raman peak is so broad that fitting using the two peaks method is difficult. The mismatch between the fit and the data points on the left side of the Raman peak indicates the presence of lossy µc-Si and nc-Si materials. The poor quality of the material is assessed by the p-Si peak width $\Gamma = 6.85\ cm^{-1}$. However, when laser processed with 90 mW at 0.2 mm/s, the fitting is much more accurate. The µc-Si and nc-Si materials have disappeared and the p-Si peak becomes thinner with $\Gamma = 2.99\ cm^{-1}$, indicating a clear improvement in the material quality.

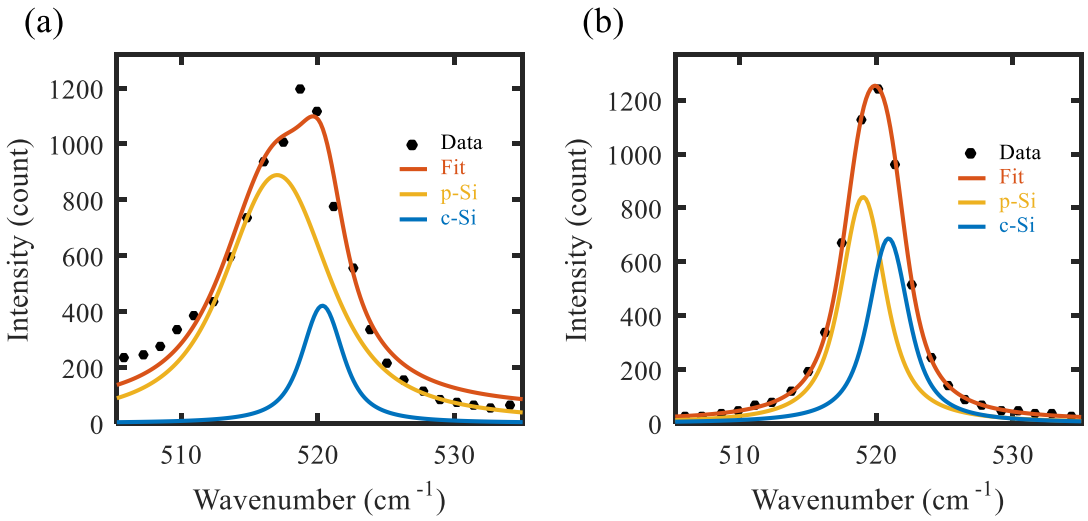

Figure 5.25: Raman spectra of as-deposited p-Si before (a) and after (b) laser processing.

Improvements on the same wire have also been observed using an XRD system. The as-deposited XRD results are shown in Figure 5.26(a) and reveal many low intensity crystals with a poor signal-to-noise ratio. However, after laser re-crystallisation, fewer crystals are observed and two large crystals, up to 12 µm long, clearly appear in Figure 5.26(b) with a better signal-to-noise ratio. It is clear that during the laser treatment, the small as-deposited crystals have merged to form larger crystals.

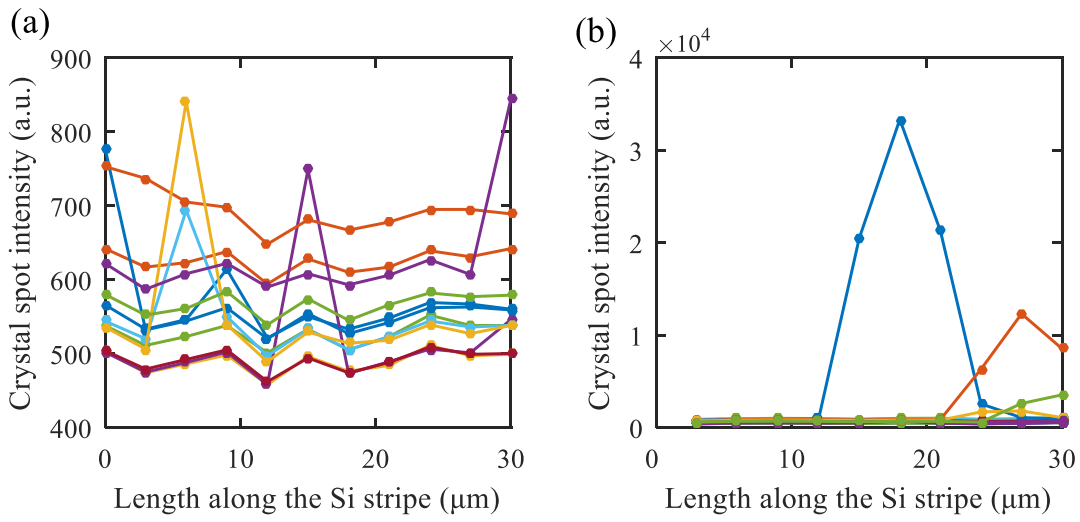

Figure 5.26: XRD of as-deposited p-Si before (a) and after (b) laser processing.

However, despite the promising results it was not possible the measure the transmission losses of these waveguides because of the laser processing starting and ending alignment marks generating too much scattering. Nevertheless, we expect the results to be lower than the initial 16 dB/cm.

5.5 Conclusion

After a brief presentation of the impacts of the different fabrication parameters, material and optical characterisation have been performed on the generation VI samples. The patterning of the silicon film allowed the heat to be better confined during the laser processing, resulting in p-Si materials with higher crystalline quality. Assessed by Raman spectroscopy, p-Si peak widths Γ as small as 2.74 cm^{-1} have been observed. Whilst using the XRD system, individual crystals up to 1.8 mm long have been recorded. The optical losses of these samples have also been measured using a standard transmission setup. For the 2 and 1.5 µm wide wires, propagations losses as low as 6.23 dB/cm and 5.31 dB/cm have been measured, respectively. To date, this is the lowest loss observed on low-temperature p-Si waveguides. Finally, some of these p-Si waveguides have been tested for nonlinear measurements. Both β_{TPA} and n_2 have been obtained by fitting the experimental data and the nonlinear FOM reveals efficiency competing with c-Si material.

In addition to the main results, we have observed significant improvements in the material quality of as-deposited p-Si waveguides that have been laser processed, indicating the versatility of this treatment method.

Chapter 6

Optical silicon fibres

6.1 Introduction

Since the mid-2000s, optical silicon core fibres have attracted a lot of attention owing to their capability to unite the advantages of highly functional silicon materials with fiberised systems capable of transmitting light over long distances. A lot of work has been done on these fibres with the aim to reduce optical propagation losses, and to date silicon fibres fabrication is dominated by two methods: high-pressure chemical vapour deposition (HPCVD) and molten core drawing (MCD). Whilst HPCVD a-Si:H core fibres show the lowest losses so far, they lack the crystalline quality required for efficient charge transport [40]. HPCVD fibres with p-Si cores can also be produced but for this material, optical losses are higher than p-Si fibres produced with MCD method. Furthermore, MC p-Si fibres have the advantage of being drawn with length of several meters.

In this chapter, I present two techniques that can improve the material quality of MCD fibres: a laser processing technique similar to the one presented previously for planar samples, and a tapering technique. The tapering technique does not only improve the quality of the core material but it also improves the nonlinear response by reducing the size of the core.

6.2 Fibre core material improved by laser processing

This section presents the results obtained with a laser processing technique when applied to silicon fibres produced by the MCD method. As described in Chapter 3, in the MCD core method, the fibres have been drawn at 1950 ^{o}C with a pulling speed of 0.18 m/s. Once drawn, the fibres have an outer

diameter of OD ~125 µm and an inner core diameter of ID ~10 µm as shown in the inset of Figure 6.1.

6.2.1 Laser processing of the fibres

The crystallization of the p-Si fibres was performed using the setup illustrated in Figure 6.1. A CO_2 laser, emitting at a wavelength of 10.6 µm, with a maximum output power of 28 W was used in the process. Using a ZnSe lens, the laser beam was focused to a spot size of 166 µm onto the fibre. Contrary to the laser processing setup presented in the previous chapters, silicon is less absorbent at the laser wavelength. Instead, it is the silica cladding which absorbs the radiation and homogeneously heats the silicon core up to its melting point. The core crystallizes as it cools down, back to room temperature. By scanning the laser beam along the fibres, long segments can be processed. To find the optimum processing conditions, different power ranges, from 6 to 18 W, and different scanning speeds, between 0.1 and 3 mm/s, were used. To monitor the laser processing, a CCD camera and a power-meter were used.

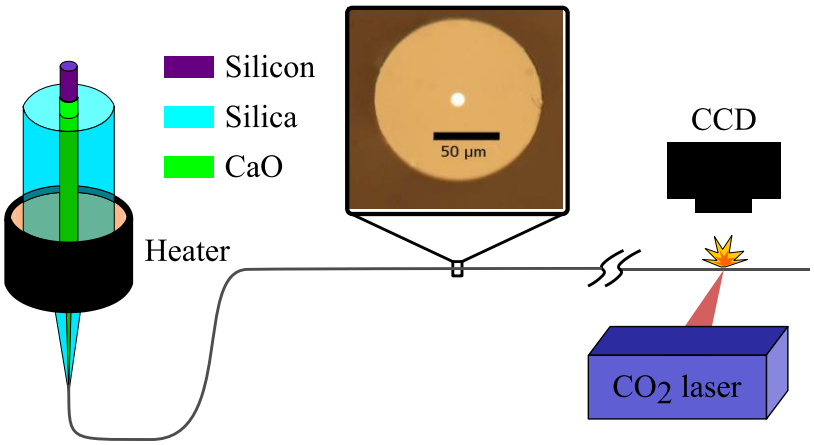

Figure 6.1: Illustration of the fibre drawing process followed by the laser CO_2 recrystallisation. Inset: optical microscope image of an as-drawn fibre cross-section.

Once the fibres have been recrystallised, marks have been made to indicate the start and end of a laser processed segment as shown in Figure 6.2. The high power used for these marks completely melted the silicon and, because of the silica capillary instability, causes the silicon core to break-up into a sphere to reduce its surface energy [183]. The fibre presented in Figure 6.2(a) has been laser processed using a laser power higher than 18 W and reveals many silicon spheres, as observed for the high power marking points. Although the sphere formation is an interesting effect it was beyond the scope of this project and therefore was not studied further.

In Figure 6.2(b), a fibre that has been laser processed with a power below 18 W presents some defects, as indicated by the arrows. These defects have been associated with impurities in the starting material or imperfections at the core/cladding interface that have been segregated in the melting

process. Fibres with these defects exhibit high scattering losses and so have been excluded from our transmission measurements.

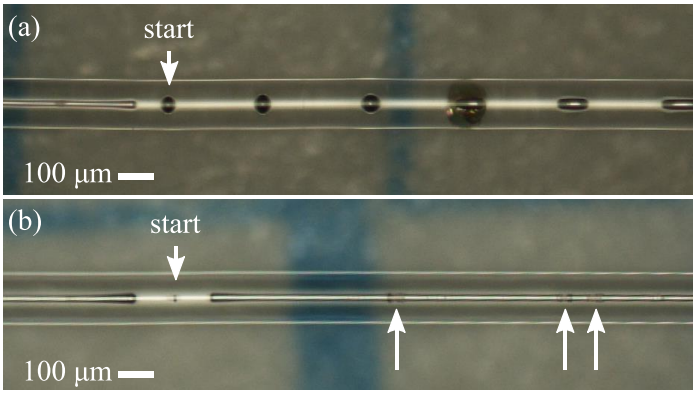

Figure 6.2: Optical microscope images of laser processed silicon core fibres with the start mark of the segment indicated by an arrow. (a) Fibre processed with laser power higher than 18 W and (b) fibre processed with a laser power below 18 W that presents defects indicated by arrows.

6.2.2 Optical transmission loss measurements

To assess any improvement in the material quality, we measured the optical losses of both the as-drawn and laser-processed fibres using the cut-back method on the optical setup described in Chapter 3 (Figure 3.23). Starting with one centimetre long fibre segments, loss values were obtained by progressively polishing off 1 mm long sections. Cut-back measurements results for the fibres, processed with 11, 14.4 and 18 W at speeds of 0.1, 1 and 3 mm/s are presented in Figure 6.3 along with the corresponding measurements for the unprocessed fibres. It can be noticed that for all the different scanning speeds, laser processing of 11 W results in no noticeable improvement as losses are situated within the 15-20 dB/cm, which is the loss range for the as-drawn fibres. However, improvements are observed at higher powers for scanning speeds of 1 and 3 mm/s. For the 0.1 mm/s scan rate, the cooling time is too long and allows for the formation of numerous nucleation sites in this large encapsulated volume of molten silicon. With a large number of crystal boundaries causing major scattering losses, fibres processed with speeds of 0.1 mm/s were abandoned. For scanning speeds of 1 and 3 mm/s, clear improvements are observed with lower losses measured for the fastest speed for which less time was available for nucleation sites to form.

Finally, increasing the laser processing power from 11 to 14.4 W resulted in a dramatic improvement of the material with a loss reduction of more than 10 dB/cm. However, further increasing the laser power from 14.4 to 18 W resulted in a smaller improvement as the material losses are close to their limit, ~2 dB/cm for the fibre processed at 3 mm/s with 18 W.

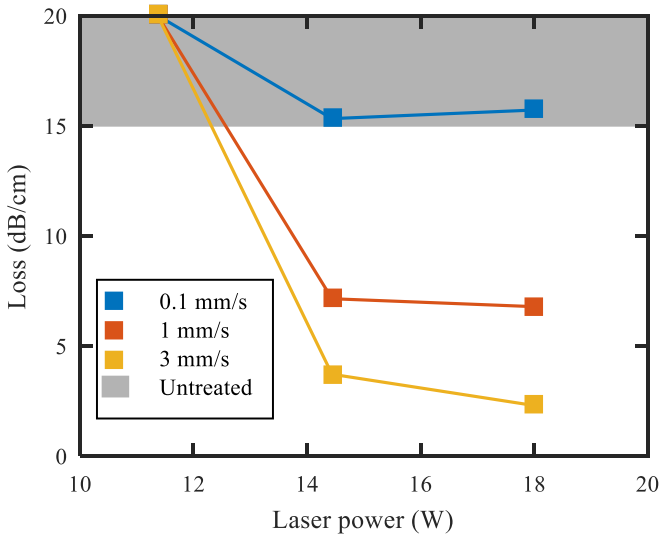

Figure 6.3: Optical loss measurements at 1.55 µm as a function of the CO_2 laser power for three different scanning speeds.

6.2.3 X-ray diffraction analysis

In addition to loss measurements, the fibre core material improvement was assessed by XRD using the setup presented in Figure 6.4(a). For these experiments, we used the XRD system in a transmission configuration as explained in Chapter 3 with a 3 µm diameter circular X-ray spot. The spot was scanned along the laser processed fibre and diffraction patterns were recorded to track the crystals present in the p-Si core. As the fibres processed at 0.1 mm/s have shown no improvement, the XRD study focuses on the fibre processed at 1 and 3 mm/s, along with the as-drawn fibres for comparison. Results of the observed crystals are presented in Figure 6.4(b).

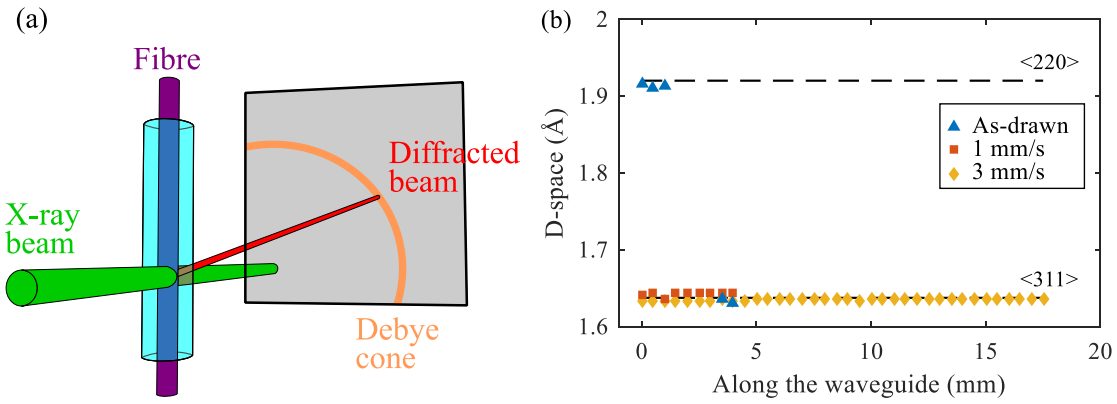

Figure 6.4: (a) Schematic of the XRD setup. (b) Lattice spacing of diffraction spots measured via XRD as a function of position along the as-drawn fibre (blue) and fibres process with 18 W at 1 and 3 mm/s, orange and yellow respectively.

For the as-drawn fibre, two small crystals have been observed along the 1.7 cm long scan. The absence of diffraction spots for most of the scan is a result of the limited field of view of the detector for this experiment, with only the ⟨311⟩ and the ⟨400⟩ crystallographic planes being detected. Still, the short length of the detected crystals indicates a lower quality material with many small crystals resulting in numerous crystal boundaries, which generate a lot of losses as observed in Figure 6.3. For the fibre processed at 1 mm/s with 18 W, a single 4 mm long crystal is observed, indicating the presence of larger crystals in the core material. Finally, for the fibre processed at 3 mm/s with 18 W, a single crystal has been observed for 17 mm, the entire scan length. The observation of such large crystal justifies the low loss that was observed with this fibre and validates the material improvement from the CO_2 laser processing technique.

6.3 Fibre enhancement by tapering

As discussed in the introduction, there is a need to reduce the losses in the p-Si core fibres and the laser processing method presented earlier has produced fibres with losses that are comparable to the lowest losses reported in the a-Si:H core fibres. However, the aforementioned method maintains the 10 µm large core diameter of the as-drawn fibre, which is too large for efficient nonlinear dynamics. Unfortunately, because of the Rayleigh-Plateau instabilities, it is challenging to draw silicon fibres to have core dimensions smaller than ~10 µm [132]. To overcome this limitation, we developed a post-processing step whereby the as-drawn fibres are tapered down to a few micrometre core sizes.

6.3.1 Tapering technique

The as-drawn fibres, described in Section 6.2, are first encased in a thick silica capillary, as shown in Figure 3.22(a), which helps to strengthen the structure as it is tapered to smaller dimensions. The sleeved fibre is then placed in a Vytran tapering rig (GPX-3300), where it is heated by a tungsten filament. While a motor feeds the fibre into the middle of the filament a second motor pulls the fibre at higher speed resulting in an elongated segment of the fibre and a tapering of the fibre diameter as illustrated in Figure 6.5(a).

During the process, both the silica cladding and the silica sleeve soften and fuse together, while the melted silicon core reshapes and crystallizes as it cools down. The tapered fibres fabricated via this technique display a smooth transition from the untapered fibre down to the waist, as shown in Figure 6.5 (b). By adjusting the filament power between 52 - 59 W, and the pulling velocity between 0.4 - 0.5 mm/s, a range of tapering ratios have been obtained, from 1:2 to 1:20, demonstrating the versatility of this process [46]. To illustrate this, Figure 6.5(c-f) shows microscope images of tapered fibres cross-sections with core diameters of 7.8, 4.4, 1.7 and 0.6 µm, respectively.

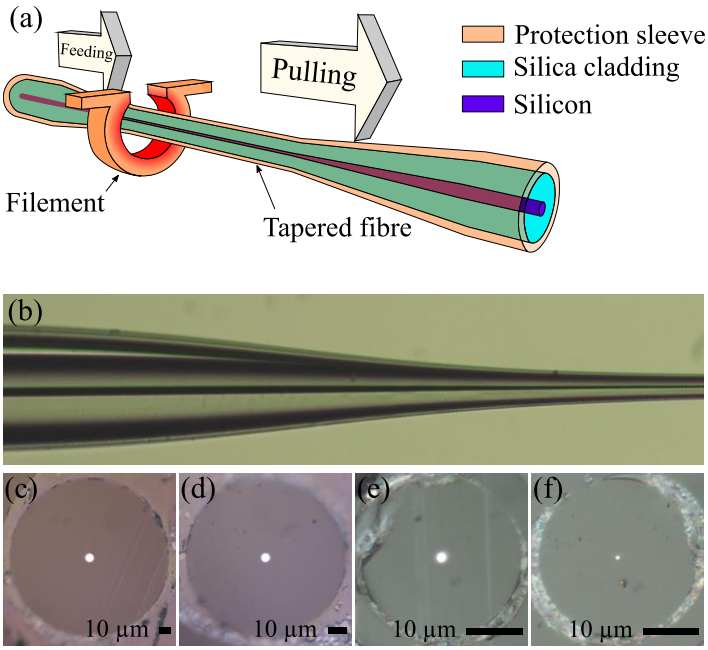

Figure 6.5: (a) Schematic of the tapering process, (b) Longitudinal image of a silicon core tapered fibre, (c-f) Microscope images of tapered fibre cross-sections with core diameters of 7.8, 4.4, 1.7 and 0.6 µm, respectively.

6.3.2 Raman spectroscopy characterisation

An initial assessment of the material properties of the tapered silicon cores was achieved by taking a series of Raman spectra along the fibre, from the untapered region of the fibre down to the waist region. The measurements were performed with the micro-Raman setup described in Chapter 3 and a single Voigt peak was used to fit experimental data. Raman results of a silicon core fibre tapered from 10 to 2 µm are displayed in Figure 6.6, where both the Lorentzian peak width Γ and the peak position values along the fibre are plotted. For visibility, the plot has been split into three sections: the untapered, the transition and the tapered regions.

From the results shown in Figure 6.6(a) we see that the peak width Γ is largely unaffected by the tapering process, within the resolution of our system, with all three sections exhibiting an average value of $\Gamma = 3.04\ \mathrm{cm}^{-1}$. This is slightly larger than the width of our single crystal silicon reference ($\Gamma = 2.7\ \mathrm{cm}^{-1}$), which suggests that the core maintains a polycrystalline form during the processing. On the other hand, the position of the peak is clearly influenced by the processing, moving further away from position of the reference peak at 520 cm^{-1} as the core diameter is decreased. The red shift in the peak position is most likely due to increased stress in the tapered silicon core material, which arises due to the differences in the thermal expansion coefficients of the strongly bonded materials, Si and SiO_2, as they cool down [47]. However, it is well known that stress-induced deformation of the silicon lattice can lift the degeneracy of the optical phonon modes, which can manifest as a

broadening of the Raman peak [184]. To gain more insight about the crystalline properties of the tapered core material, XRD experiments where conducted on these fibres.

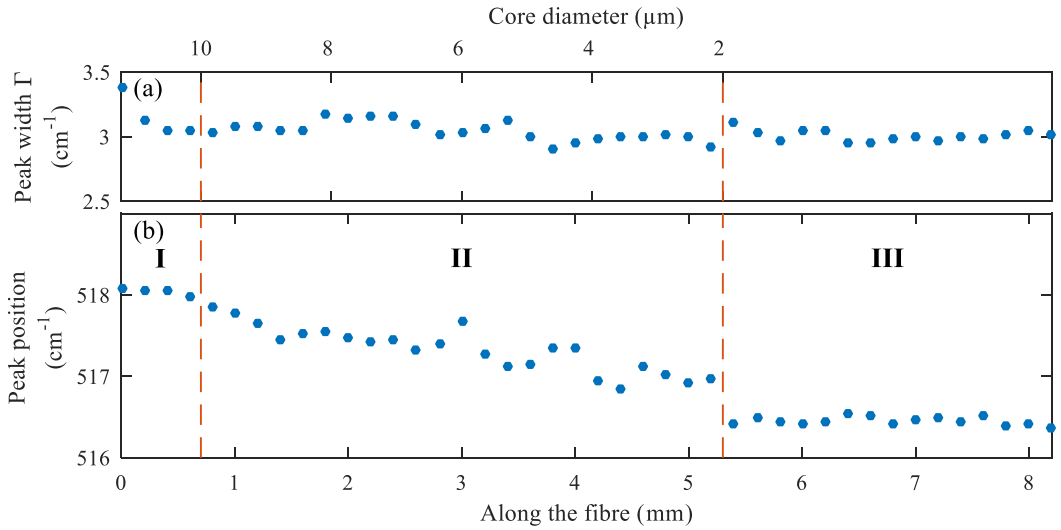

Figure 6.6: Evolution of the Raman peak width (a) and position (b) along a 2 µm core fibre. The untapered, transition and tapered regions are indicated by **I**, **II** and **III** respectively. The red dashed lines mark out the different sections of the taper.

6.3.3 Crystallographic characterisation

Owing to the small material volume of the tapered core, the 3 µm diameter X-ray diffraction beam was expanded to 30 µm wide and 3 µm high to increase the interaction area as shown in Figure 6.7.

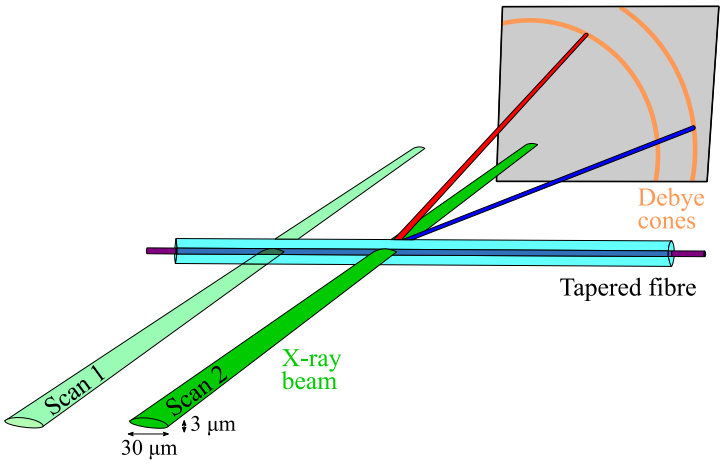

Figure 6.7: Illustration of the XRD experiment. A large X-ray beam is scanned at different positions along the silicon core fibre and the diffraction pattern is collected by an X-ray detector array .

Both the incident and diffracted beams were then collected by the detector, as shown in Figure 6.8(a) and (b) where diffraction patterns measured for both the as-drawn fibre and the tapered waist are

presented, respectively. We note that the stronger signal measured for the as-drawn fibre is simply due the larger material volume in this section.

It is clear from Figure 6.8(a) that there is only one diffraction spot in the detection plane, indicating that the core consists of a single crystal which extends across the entire 10 µm diameter core, at least within the 30 µm length of the X-ray beam. Furthermore, the symmetry of the spot, and the fact that it is well aligned to the dashed reference for the ⟨311⟩ crystallographic plane, provides evidence that any residual stress remaining in the core following the high temperature draw process is small. In contrast, the single diffraction spot in Figure 6.8(b), is stretched in the radial direction. This stretch, suggesting that within the same crystal all the interlayers spacing are not the same, is associated to an anisotropic strain [44]. Although the centre of this spot is also slightly shifted from the c-Si reference line (a measured d-spacing of 1.918 Å compared to the predicted 1.920 Å), this shift is within the 0.006 Å error of the XRD system, as discussed in Chapter 5, and thus is not deemed to be significant.

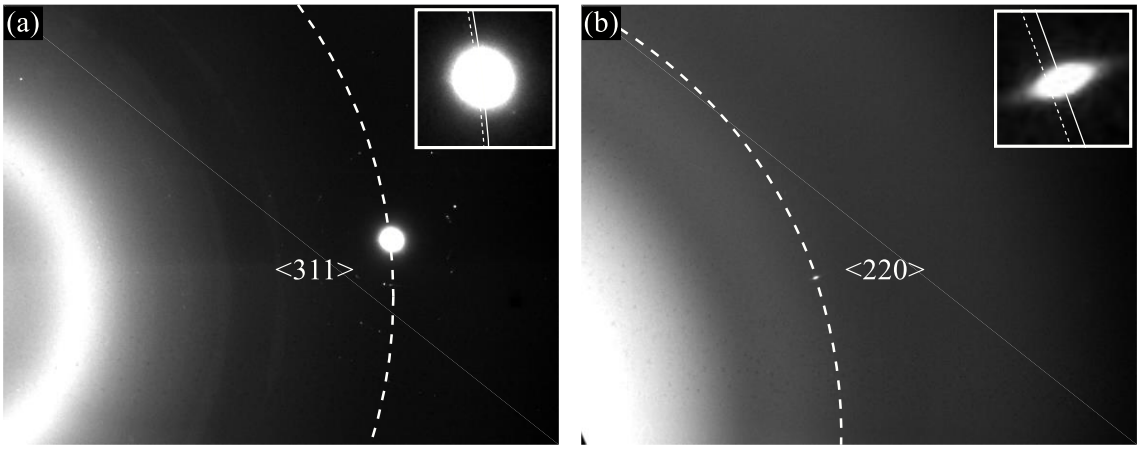

Figure 6.8: Two-dimensional XRD patterns for single crystal materials sampled within (a) the as-drawn fibre and (b) the waist section tapered down to 2 µm. The large dashed curves indicate the projection of the Debye cone for the ⟨311⟩ silicon plane and the ⟨220⟩ plane. The insets show close up images of the diffracted beam, where the straight curve is aligned with the centre of the spot.

For a full analysis of the core material, the X-ray beam was then scanned along the fibre length to map the crystal size. The complete mapping of the crystallinity within two ~1 cm long sections of the fibre with ~500 µm steps, corresponding to the as-draw fibre, plotted with blue diamonds, and the tapered waist, plotted with red squares, is shown in Figure 6.9. The as-drawn fibre is clearly composed of several millimetre long crystals, including some parts where several crystals are observed in the same cross-section, in agreement with previous measurements of these fibres [45], [48]. However, the tapered region is found to consist of only a single crystal which extends over a length of ~9 mm, verifying that the crystallinity has been improved by the tapering process, as predicted in [46].

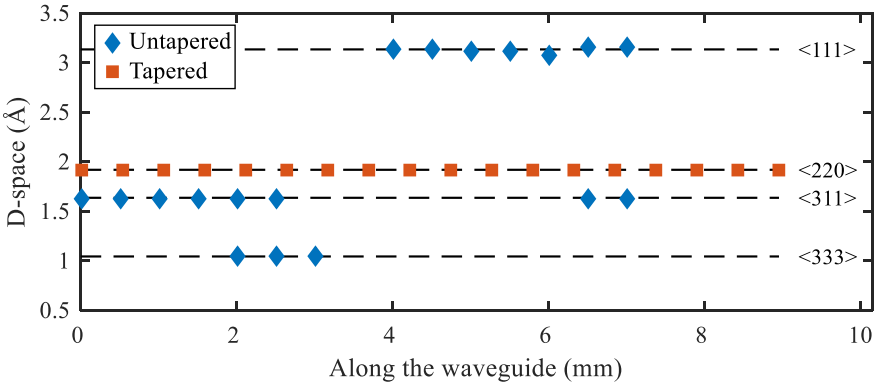

Figure 6.9: Lattice spacing of diffraction spots measured via XRD as a function of position along the as-drawn fibre (blue diamonds) and the 2 µm waist (red squares).

Additional measurements were also conducted on two further tapered fibres with waist diameters of 3 µm and 0.9 µm, with the longest measured single crystal in each fibre reported in Table 6-1. This table shows a general trend of increasing crystal size for decreasing core size, in the micrometre range, which we attribute to faster cooling rates that help to suppress the number of nucleation sites to enable the formation of larger crystals [45], [185], [186]. We note that the slightly smaller crystal size measured for the sub-micron core fibre is most likely due to the fact that the CaO interface layer is not optimised for these dimensions, resulting in an increased strain between the core and cladding materials. Nevertheless, we expect the increased crystal sizes measured in the tapered fibres to significantly improve the transmission properties of the polysilicon fibres, as by reducing the number of crystal boundaries we also reduce the defect material that surrounds these.

6.3.4 Optical transmission losses

The core quality of these fibres has been assessed through optical loss measurements using the cut-back method. The results, reported in Table 6-1, are an average loss of the fundamental mode through the tapered waist of the fibre. Significantly, the losses of ~2 dB/cm reported for the 1-2 µm diameter fibres represent a marked improvement (of more than 1 dB/cm) over previous results reported by our group in Ref [46]. Thus we expect that comprehensive XRD characterisations could be used to further optimize the tapering process to produce even longer single crystal in both the micro and nano-scale cores, ultimately allowing for the production of silicon fibres with losses below 1 dB/cm.

Core diameter (µm)	Crystal length (mm)	Optical loss (dB/cm)
10 (as-drawn)	3	12
3	4.6	3.5
2	9.2	2.0
0.9	7.5	2.4

Table 6-1: Measurements of the maximum crystal length together with loss values at 1550 nm for different tapered core sizes.

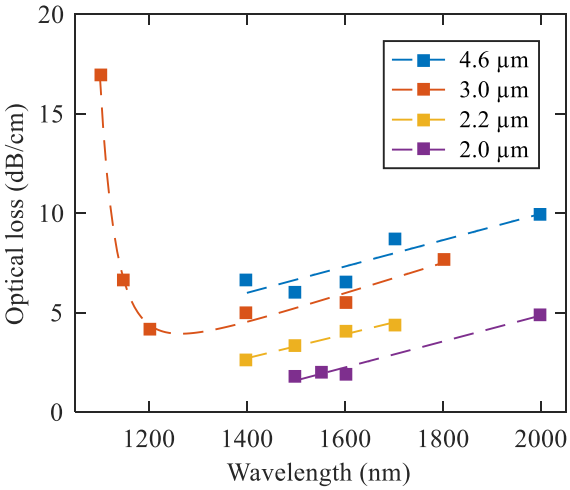

Figure 6.10: Optical loss cut-back measurements for different tapered core sizes at different wavelengths. Dashed lines are given as guides to the eye.

For future applications such as the generation of supercontinuum, the optical losses of fibres with different core sizes have also been measured using the wavelength dependent transmission setup across the region of 1.1 µm to 2 µm. The propagation losses for the 4.6, 3, 2.2 and 2 µm diameter core size fibres are reported in Figure 6.10. Because these measurements were performed on different fibres from the ones presented in Table 6-1, the losses are not identical. The first observation is that, as observed in Table 6-1, lower losses are observed for smaller cores. The second observation is that higher losses are measured at longer wavelengths. However, the optical loss in the silicon core fibres is expected to be constant up to wavelengths of ~3 µm, at which point the silica cladding becomes very lossy. The observed increase in loss was first attributed to stronger interactions with the CaO interface layer containing segregated impurities from the tapering process. However, investigations performed by the fibre fabrication group, on the as-drawn fibres, revealed that the increased loss at longer wavelengths was actually related to the intrinsic material and not the CaO interface layer. The optical losses of the next batch of drawn silicon core fibre is expected to maintain low losses beyond 1.55 µm for future work within this project. Finally, we note that the sharp increase around 1.1 µm corresponds to the short wavelength edge of silicon transparency window.

6.3.5 Core/cladding interface quality

Although for the micron-sized fibres used in this work the main source of loss is from the bulk material, as we continue to scale the core sizes down towards the nanoscale regime, the surface quality of the silicon/silica interface will play an increasingly important role. As a final investigation, we imaged the core surface using different techniques.

To gain more insight on the core surface than what is possible using optical microscopy, a SEM has been used to image the cross-section of the fibres at higher magnification. However, as shown in Figure 6.11 where optical microscope and SEM images are compared side by side, the contrast between silica and silicon is too weak for proper imaging. Also, the polymer wax used to maintain the fibre within the capillaries during the tapering and polishing, was pulled out of the fibre when positioned in the SEM vacuum chamber.

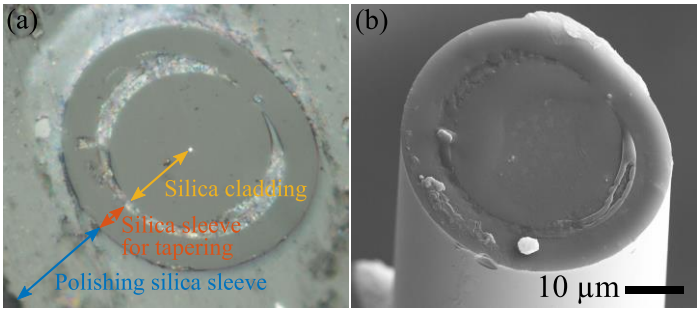

Figure 6.11: Optical microscope (a) and SEM (b) images of the polish facet of a 0.6 µm core diameter silicon fibre.

Therefore, we used a 7:1 buffered hydrofluoric acid solution to etch the silica cladding away from the core, so that we can assess the surface roughness of the silicon wire directly. Using microscope imaging, as shown in Figure 6.12(a), different etching durations have been tested and the silica etching rate with this solution was estimated at 5.6 µm/h. After fully etching the silica cladding away, the waist of the silicon core was imaged with the SEM as shown in Figure 6.12(b) and (c), revealing a smooth surface without any obvious crystal boundaries.

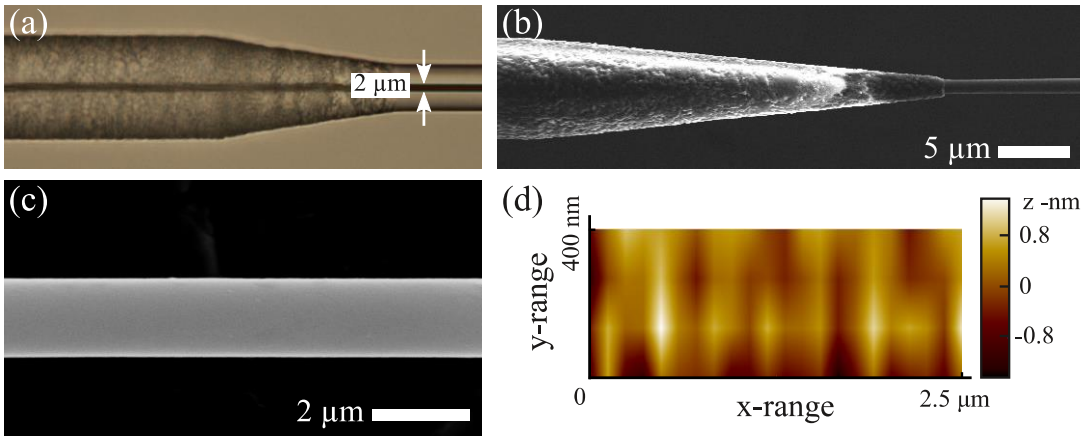

Figure 6.12: (a) Optical microscope image of a partially etched fibre, (b-c) SEM micrographs of a silicon core fibre with partially and fully etched cladding, respectively, and (d) topographical scan of a silicon core fibre waist (~2 µm diameter) after removal of the silica cladding.

Finally, further confirmation of the good interface quality was obtained using a ZeScope three dimensional optical profiler, from which we measured a root-mean-square roughness of ~0.7 nm as

shown in Figure 6.12(d). Thus, these results confirm the tapering procedure as a viable route to obtaining low loss crystalline silicon core fibres with sub-micron core sizes, which would be of great value for nonlinear optical applications [187].

6.3.6 Conclusion

This chapter introduced two techniques for the post-fabrication improvement of silicon core optical fibres. Starting from a polycrystalline material, the first technique based on laser processing improved the core material quality by re-melting small silicon crystals into larger and less numerous crystals up to 17 mm in length. This improvement allowed the optical loss to drop from 20 dB/cm to ~2 dB/cm. However, despite this huge enhancement, the core diameter of these fibres is still too large for optimal nonlinear processing.

In a second section, another improvement technique was presented based on tapering the p-Si core fibres. In addition to improving the silicon core material through melting and recrystallization, the tapering process allowed to finely adjust the final core diameter size for mode effective area tuning. Using this technique, optical losses of 2 dB/cm have been measured, but starting material still requires some improvement. Finally, a fibre with a 0.9 µm silicon core diameter and losses of ~2 dB/cm has been fabricated and should be suitable for future nonlinear applications.

Chapter 7

Conclusion and Future Work

7.1 Conclusions

During this PhD project, different objectives have been achieved forming a base for the opening of various new project opportunities in silicon photonics on both planar and fibre geometries.

The first accomplishment in this thesis has been the development of a back-end deposition technique for the integration of silicon waveguides with a thermal budget of 450 °C to be compatible with a large variety of substrates including CMOS chips. Based on CVD a-Si, laser crystallisation and patterns dimensions achievable by industrial photolithography, the technique presented here produces high quality p-Si at low cost. With preliminary work led on planar samples, crystallisation of silicon has been observed with crystals up to 6 µm long and Raman peak width as low as 2.87 cm^{-1}. Later, patterned samples have been investigated in. The material quality of the p-Si wires has been assessed by Raman spectroscopy with peak width of 2.74 cm^{-1} and XRD with the observation of crystals up to 1.8 mm long. Also, microscopy indicated a semi-circular reshaping of the waveguide due to surface tension occurring during the laser processing. Finally, the most promising samples have also been optically tested on a transmission setup revealing propagation losses as low as 5.31 dB/cm, lower than what has previously been presented for both high and low temperature p-Si, and nonlinear dynamics competing with crystalline silicon materials.

In parallel to planar geometry, the laser crystallisation technique has also been applied to silicon core fibres drawn by MC technique. The first technique, based only on laser crystallisation, revealed material improvement with the presence of larger crystals and lower losses. However, the few microns core is too large for efficient nonlinear dynamics. A second technique, based on tapering, allowed both re-crystallisation and core diameter reduction by using a tapering rig. This technique

demonstrated material with losses as low as 2 dB/cm and core diameters of 0.9 µm better suited for nonlinear applications.

7.2 Future Work

As presented above, the work realised during this project opens several doors in term of device fabrication and nonlinear applications. Different possible future research work ignited by this thesis are summarised hereunder:

i. Technique improvement. Now that a fabrication technique to deposit high quality p-Si wire waveguides at low temperatures has been developed, it can still be improved further. The automatic deposition of a capping silica layer on top of the laser processed waveguides should reduce propagation losses by keeping the waveguide surface pristine and protect it from potential debris. Also, the lowered refractive index difference at the core/cladding interface will reduce light scattering on waveguide walls. Furthermore, this technique can be improved by introducing more complex laser processing designs such as Y-junctions, Mach-Zehnder interferometers or ring resonators and using multiple depositions for 3D stacking of optoelectronic layers.

ii. Larger choice of material and sources. Another opening for this project consists in applying this crystallisation technique to different semiconductors such as germanium or silicon-germanium (SiGe) alloys. Preliminary work from our group based on SiGe laser crystallisation has already been presented at a conference, and brief tests realised on germanium films indicated similar results to silicon with lower laser powers due to higher absorption of germanium at 488 nm. In addition to different materials, difference laser sources can also be investigated such as UV radiation with a shorter absorption depth.

iii. Nonlinear dynamics. This project introduced waveguides on both planar and fibre geometries with losses that are low enough for the observation of nonlinear dynamics. These dynamics have to be thoroughly investigated in order to push forward research on low-temperature p-Si and find applications such as all-optical treatment.

Appendix A

List of publications

Journal Papers

[1] **Y. Franz**, A. F. J. Runge, S. Z. Oo, G. Jimenez-Martinez, N. Healy, A, Khokhar, A. Tarazona, H. M. H. Chong, S. Mailis and A. C. Peacock, *Laser crystallized low-loss polycrystalline silicon ridge waveguides*, Optics Letters, 2018. *(Submitted)*

[2] M. Milosevic, X. Chen, W. Cao, A. F. Runge, **Y Franz**, C. Littlejohns, S. Mailis, A. C. Peacock, D. J. Thomson and G. T. Reed, *Ion implantation in silicon for trimming the operating wavelength of ring resonators*, IEEE Journal of selected topics in quantum electronics, 2017.

[3] H. Ren, O. Aktas, **Y. Franz**, A. F.J. Runge, T. Hawkins, J. Ballato, U. J. Gibson, A. C. Peacock, *Tapered silicon core fibers with nano-spikes for optical coupling via spliced silica fibers*, Optics Express, 2017

[4] X. Chen, M. Milosevic, D. J. Thomson, A. Z. Khokhar, **Y. Franz**, A. F. Runge, S. Mailis, A. C. Peacock and G. Reed, *Post-fabrication phase trimming of Mach-Zehnder interferometers by laser annealing of germanium implanted waveguides*, Photonics Research, 2017.

[5] G. Zisis, G. Martinez Jimenez, **Y. Franz**, N. Healy, T. Ben Masaud, H. M. Chong, E. Soergel, A. C. Peacock and S. Mailis, *Laser-induced ferroelectric domain engineering in $LiNbO_3$ crystals using an amorphous silicon overlayer*, Journal of Optics, 2017.

[6] **Y. Franz**, A. F. Runge, H. Ren, N. Healy, K. Ignatyev, M. Jones, T. Hawkins, J. Ballato, U. Gibson and A. Peacock, *Material properties of tapered crystalline silicon core fibers*, Optical Materials Express, vol. 7, no. 6, pp. 2055-2061, 2017.

[7] N. Healy, M. Fokine, **Y. Franz**, T. Hawkins, M. Jones, J. Ballato, A. C. Peacock and U. J. Gibson, *CO_2 laser-induced directional recrystallization to produce single crystal silicon-core optical fibers with low loss*, Advanced Optical Materials, vol. 4, no. 7, pp. 1004–1008, 2016.

[8] F. H. Suhailin, N. Healy, **Y. Franz**, M. Sumetsky, J. Ballato, A. Dibbs, U. Gibson and A. C. Peacock, *Kerr nonlinear switching in a hybrid silica-silicon microspherical resonator*, Optics express, vol. 23, no. 13, pp. 17263–17268, 2015.

Conference Papers

[1] X. Chen, M. Milosevic, D. J. Thomson, A. Z. Khokhar, **Y. Franz**, A. F. Runge, S. Mailis, A. C. Peacock and G. Reed, *Phase trimming of Mach-Zehnder interferometers by laser annealing of germanium implanted waveguides*, IEEE 14th International Conference on Group IV Photonics (Berlin), 2017.

[2] A. F. Runge, **Y. Franz**, C. Littlejohns, K. Grabska, S. Mailis, F. Gardes and A. C. Peacock, *Laser-assisted material composition engineering of SiGe planar waveguides*, CLEO Pacific Rim Conference (Singapore), Optical Society of America, 2017.

[3] **Y. Franz**, A. F. Runge, S. Z. Oo, N. Healy, G. Martinez-Jimenez, A. Z. Khokhar, A. Tarazona, H. M. Chong, S. Mailis and A. C. Peacock, *Laser annealed low temperature deposited polysilicon waveguides for nonlinear photonics*, CLEO/Europe-EQEC (Munich), CE-6.5, Optical Society of America, 2017. *(Talk)*

[4] G. Martinez Jimenez, **Y. Franz**, A. F. Runge, M. Ceschia, N. Healy, S. Z. Oo, A. Tarazona, H. M. Chong, A. C. Peacock and S. Mailis, *Laser writing of polycrystalline Si ridge waveguides*, CLEO/Europe-EQEC (Munich), CE-P.26, Optical Society of America, 2017.

[5] **Y. Franz**, A. F. Runge, S. Z. Oo, N. Healy, G. Martinez-Jimenez, A. Z. Khokhar, A. Tarazona, H. M. Chong, S. Mailis and A. C. Peacock, *Laser annealing of low temperature deposited silicon waveguides*, CLEO: Science and Innovations (San José), SM3K–4, Optical Society of America, 2017. *(Talk)*

[6] S. Mailis, G. Martinez Jimenez, G. Zisis, **Y. Franz**, N. Healy, D. Grech, H. M. Chong and A. C. Peacock, *Laser processing of amorphous silicon on lithium niobate for photonic applications*, FNM: International Workshop on Functional and Nanostructured Materials (Tbilisi), 2016.

[7] F. Gardes, C. Littlejohns, M. Nedeljkovic, T. B. Dominguez, N. Hattasan, M. Banakar, A. L. Mastronardi, A. Khokhar, K. Grabska, G. Reed, G. Z. Mashanovich, A. F. Runge, **Y. Franz**, A. C. Peacock, A. Al-Attili and S. Saito, *Group IV compounds for integrated photonic applications*, in Group IV Photonics, IEEE 13th International Conference (Shangai), pp. 174– 175, IEEE, 2016.

[8] **Y. Franz**, N. Healy, G. Martinez Jimenez, T. Ben Masaud, H. M. Chong, S. Mailis and A. C. Peacock, "Development of polycrystalline silicon waveguides by laser crystallization," European Congress and Exhibition on Advanced Materials and Processes (Warsaw), 2015. *(Talk)*

[9] S. Mailis, N. Healy, G. Martinez Jimenez, G. Zisis, **Y. Franz**, D. Grech, H. M. Chong and A. C. Peacock, *A silicon/lithium niobate hybrid photonic material platform produced by laser processing*, European Congress and Exhibition on Advanced Materials and Processes (Warsaw), 2015.

[10] G. Martinez-Jimenez, G. Zisis, **Y. Franz**, N. Healy, D. Grech, H. M. Chong, A. C. Peacock and S. Mailis, *A poly-Si on $LiNbO_3$ photonic platform*, The European Conference on Lasers and Electro-Optics (Munich), CE-4.2, Optical Society of America, 2015.

[11] G. Martinez-Jimenez, G. Zisis, **Y. Franz**, N. Healy, A. C. Peacock, H. M. Chong, D. Grech and S. Mailis, *Laser crystallization of silicon on lithium niobate*, CLEO: QELS Fundamental Science (San José), JTh2A–85, Optical Society of America, 2014.

[12] S. Mailis, G. Martinez, G. Zisis, **Y. Franz**, N. Healy and A. Peacock, *Annealing of amorphous silicon using cw visible lasers*, Materials Research Society Spring Meeting, (Lille), 2014.

References

[1] J. Leuthold, C. Koos, and W. Freude, “Nonlinear silicon photonics,” *Nat. Photonics*, vol. 4, no. 8, p. 535, 2010.

[2] R. A. Soref and J. P. Lorenzo, “Single-crystal silicon: a new material for 1.3 and 1.6 $μ$m integrated-optical components,” *Electron. Lett.*, vol. 21, no. 21, pp. 953–954, 1985.

[3] C. Z. Zhao, E. K. Liu, G. Z. Li, and L. Guo, “Silicon-on-insulator optical intensity modulator based on waveguide-vanishing effect,” *Electron. Lett.*, vol. 32, no. 18, pp. 1667–1668, 1996.

[4] J. P. Lorenzo and R. A. Soref, “1.3 $μ$m electro-optic silicon switch,” *Appl. Phys. Lett.*, vol. 51, no. 1, pp. 6–8, 1987.

[5] M. Lipson, “Guiding, modulating, and emitting light on silicon-challenges and opportunities,” *J. Light. Technol.*, vol. 23, no. 12, pp. 4222–4238, 2005.

[6] M. Haurylau *et al.*, “On-chip optical interconnect roadmap: Challenges and critical directions,” *IEEE J. Sel. Top. Quantum Electron.*, vol. 12, no. 6, pp. 1699–1705, 2006.

[7] L. Pavesi and G. Guillot, “Optical interconnects,” *Springer Ser. Opt. Sci.*, vol. 119, 2006.

[8] D. Thomson *et al.*, “Roadmap on silicon photonics,” *J. Opt.*, vol. 18, no. 7, p. 73003, 2016.

[9] R. Soref, “The past, present, and future of silicon photonics,” *IEEE J. Sel. Top. quantum Electron.*, vol. 12, no. 6, pp. 1678–1687, 2006.

[10] A. Rickman, G. T. Reed, B. L. Weiss, and F. Namavar, “Low-loss planar optical waveguides fabricated in SIMOX material,” *IEEE photonics Technol. Lett.*, vol. 4, no. 6, pp. 633–635, 1992.

[11] J. Cardenas, C. B. Poitras, J. T. Robinson, K. Preston, L. Chen, and M. Lipson, “Low loss etchless silicon photonic waveguides,” *Opt. Express*, vol. 17, no. 6, pp. 4752–4757, 2009.

[12] X. Xiao *et al.*, “High-speed, low-loss silicon Mach--Zehnder modulators with doping optimization,” *Opt. Express*, vol. 21, no. 4, pp. 4116–4125, 2013.

[13] Q. Xu, D. Fattal, and R. G. Beausoleil, “Silicon microring resonators with 1.5 μm radius,” *Opt. Express*, vol. 16, no. 6, pp. 4309–4315, 2008.

[14] H. Rong, R. Jones, A. Liu, O. Cohen, and others, “A continuous-wave Raman silicon laser,” *Nature*, vol. 433, no. 7027, p. 725, 2005.

[15] R. E. Camacho-Aguilera *et al.*, “An electrically pumped germanium laser,” *Opt. Express*, vol. 20, no. 10, pp. 11316–11320, 2012.

[16] L. Chen, K. Preston, S. Manipatruni, and M. Lipson, "Integrated GHz silicon photonic interconnect with micrometer-scale modulators and detectors," *Opt. Express*, vol. 17, no. 17, pp. 15248–15256, 2009.

[17] L. Vivien *et al.*, "Zero-bias 40Gbit/s germanium waveguide photodetector on silicon," *Opt. Express*, vol. 20, no. 2, pp. 1096–1101, 2012.

[18] A. Harke, M. Krause, and J. Mueller, "Low-loss singlemode amorphous silicon waveguides," *Electron. Lett.*, vol. 41, no. 25, pp. 1377–1379, 2005.

[19] M. J. A. De Dood, A. Polman, T. Zijlstra, and E. der Drift, "Amorphous silicon waveguides for microphotonics," *J. Appl. Phys.*, vol. 92, no. 2, pp. 649–653, 2002.

[20] F. G. Della Corte and S. Rao, "Use of amorphous silicon for active photonic devices," *IEEE Trans. Electron Devices*, vol. 60, no. 5, pp. 1495–1505, 2013.

[21] J. Gaspar, O. Paul, V. Chu, and J. P. Conde, "Mechanical properties of thin silicon films deposited at low temperatures by PECVD," *J. Micromechanics Microengineering*, vol. 20, no. 3, p. 35022, 2010.

[22] N. H. Nickel, *Laser Crystallization of Silicon-Fundamentals to Devices*, vol. 75. Academic Press, 2003.

[23] D. L. Staebler and C. R. Wronski, "Reversible conductivity changes in discharge-produced amorphous Si," *Appl. Phys. Lett.*, vol. 31, no. 4, pp. 292–294, 1977.

[24] B. Kuyken *et al.*, "Nonlinear properties of and nonlinear processing in hydrogenated amorphous silicon waveguides," *Opt. Express*, vol. 19, no. 26, pp. B146--B153, 2011.

[25] J. S. Orcutt *et al.*, "Nanophotonic integration in state-of-the-art CMOS foundries," *Opt. Express*, vol. 19, no. 3, pp. 2335–2346, 2011.

[26] T. Pinguet *et al.*, "Monolithically integrated high-speed CMOS photonic transceivers," in *Group IV Photonics, 2008 5th IEEE International Conference on*, 2008, pp. 362–364.

[27] G. T. Reed and A. P. Knights, *Silicon photonics: an introduction*. John Wiley & Sons, 2004.

[28] M. Alexe and U. Gösele, *Wafer bonding: applications and technology*, vol. 75. Springer Science & Business Media, 2013.

[29] C. Yu, L. Huan, and L. Mo, "Flexible and tunable silicon photonic circuits on plastic substrates," *Sci. Rep.*, vol. 2, p. 622, 2012.

[30] K. Preston, P. Dong, B. Schmidt, and M. Lipson, "High-speed all-optical modulation using polycrystalline silicon microring resonators," *Appl. Phys. Lett.*, vol. 92, no. 15, p. 151104, 2008.

[31] L. Liao, D. R. Lim, A. M. Agarwal, X. Duan, K. K. Lee, and L. C. Kimerling, "Optical

transmission losses in polycrystalline silicon strip waveguides: effects of waveguide dimensions, thermal treatment, hydrogen passivation, and wavelength," *J. Electron. Mater.*, vol. 29, no. 12, pp. 1380–1386, 2000.

[32] A. M. Agarwal, L. Liao, J. S. Foresi, M. R. Black, X. Duan, and L. C. Kimerling, "Low-loss polycrystalline silicon waveguides for silicon photonics," *J. Appl. Phys.*, vol. 80, no. 11, pp. 6120–6123, 1996.

[33] K. Preston, S. Manipatruni, A. Gondarenko, C. B. Poitras, and M. Lipson, "Deposited silicon high-speed integrated electro-optic modulator," *Opt. Express*, vol. 17, no. 7, pp. 5118–5124, 2009.

[34] J. S. Orcutt *et al.*, "Low-loss polysilicon waveguides fabricated in an emulated high-volume electronics process," *Opt. Express*, vol. 20, no. 7, pp. 7243–7254, 2012.

[35] J. M. Shainline *et al.*, "Depletion-mode polysilicon optical modulators in a bulk complementary metal-oxide semiconductor process," *Opt. Lett.*, vol. 38, no. 15, pp. 2729–2731, 2013.

[36] P. M. Smith, P. G. Carey, and T. W. Sigmon, "Excimer laser crystallization and doping of silicon films on plastic substrates," *Appl. Phys. Lett.*, vol. 70, no. 3, pp. 342–344, 1997.

[37] S. D. Brotherton *et al.*, "Laser crystallised poly-Si TFTs for AMLCDs," *Thin Solid Films*, vol. 337, no. 1, pp. 188–195, 1999.

[38] Y. H. D. Lee, M. O. Thompson, and M. Lipson, "Deposited low temperature silicon GHz modulator," *Opt. Express*, vol. 21, no. 22, pp. 26688–26692, 2013.

[39] P. J. A. Sazio *et al.*, "Microstructured optical fibers as high-pressure microfluidic reactors," *Science (80-.).*, vol. 311, no. 5767, pp. 1583–1586, 2006.

[40] A. C. Peacock, U. J. Gibson, and J. Ballato, "Silicon optical fibres--past, present, and future," *Adv. Phys. X*, vol. 1, no. 1, pp. 114–127, 2016.

[41] A. C. Peacock, J. R. Sparks, and N. Healy, "Semiconductor optical fibres: progress and opportunities," *Laser Photon. Rev.*, vol. 8, no. 1, pp. 53–72, 2014.

[42] J. Ballato *et al.*, "Silicon optical fiber," *Opt. Express*, vol. 16, no. 23, pp. 18675–18683, 2008.

[43] P. Mehta, N. Healy, T. D. Day, P. J. A. Sazio, J. V Badding, and A. C. Peacock, "Effect of core size on nonlinear transmission in silicon optical fibers," in *Lasers and Electro-Optics (CLEO), 2012 Conference on*, 2012, pp. 1–2.

[44] N. Healy *et al.*, "Extreme electronic bandgap modification in laser-crystallized silicon optical fibres," *Nat. Mater.*, vol. 13, no. 12, pp. 1122–1127, 2014.

[45] N. Healy *et al.*, "CO2 Laser-Induced Directional Recrystallization to Produce Single Crystal Silicon-Core Optical Fibers with Low Loss," *Adv. Opt. Mater.*, vol. 4, no. 7, pp. 1004–1008,

2016.

[46] F. H. Suhailin *et al.*, "Tapered polysilicon core fibers for nonlinear photonics," *Opt. Lett.*, vol. 41, no. 7, pp. 1360–1363, 2016.

[47] L. Lagonigro *et al.*, "Low loss silicon fibers for photonics applications," *Appl. Phys. Lett.*, vol. 96, no. 4, p. 41105, 2010.

[48] E. F. Nordstrand, A. N. Dibbs, A. J. Eraker, and U. J. Gibson, "Alkaline oxide interface modifiers for silicon fiber production," *Opt. Mater. Express*, vol. 3, no. 5, pp. 651–657, 2013.

[49] P. Mehta *et al.*, "All-optical modulation using two-photon absorption in silicon core optical fibers," *Opt. Express*, vol. 19, no. 20, pp. 19078–19083, 2011.

[50] P. Mehta, N. Healy, N. F. Baril, P. J. A. Sazio, J. V Badding, and A. C. Peacock, "Nonlinear transmission properties of hydrogenated amorphous silicon core optical fibers," *Opt. Express*, vol. 18, no. 16, pp. 16826–16831, 2010.

[51] D.-J. Won *et al.*, "All-optical modulation of laser light in amorphous silicon-filled microstructured optical fibers," *Appl. Phys. Lett.*, vol. 91, no. 16, p. 161112, 2007.

[52] G. Chartier, *Introduction to optics*. Springer Science & Business Media, 2005.

[53] J.-M. Liu, *Photonic devices*. Cambridge University Press, 2009.

[54] C. DeCusatis and I. Kaminow, *The Optical Communications Reference*. Academic Press, 2009.

[55] K. Okamoto, *Fundamentals of optical waveguides*. Academic press, 2010.

[56] P. G. Huray, *Maxwell's equations*. John Wiley & Sons, 2011.

[57] M. E. Fermann, A. Galvanauskas, and G. Sucha, *Ultrafast lasers: technology and applications*, vol. 80. CRC Press, 2002.

[58] C. Caloz and T. Itoh, *Electromagnetic metamaterials: transmission line theory and microwave applications*. John Wiley & Sons, 2005.

[59] B. Tatian, "Fitting refractive-index data with the Sellmeier dispersion formula," *Appl. Opt.*, vol. 23, no. 24, pp. 4477–4485, 1984.

[60] H. H. Li, "Refractive index of silicon and germanium and its wavelength and temperature derivatives," *J. Phys. Chem. Ref. Data*, vol. 9, no. 3, pp. 561–658, 1980.

[61] K. Luke, Y. Okawachi, M. R. E. Lamont, A. L. Gaeta, and M. Lipson, "Broadband mid-infrared frequency comb generation in a Si 3 N 4 microresonator," *Opt. Lett.*, vol. 40, no. 21, pp. 4823–4826, 2015.

[62] A. Gondarenko, J. S. Levy, and M. Lipson, "High confinement micron-scale silicon nitride high Q ring resonator," *Opt. Express*, vol. 17, no. 14, pp. 11366–11370, 2009.

[63] K. Ikeda, R. E. Saperstein, N. Alic, and Y. Fainman, “Thermal and Kerr nonlinear properties of plasma-deposited silicon nitride/silicon dioxide waveguides,” *Opt. Express*, vol. 16, no. 17, pp. 12987–12994, 2008.

[64] J. S. Levy, A. Gondarenko, M. A. Foster, A. C. Turner-Foster, A. L. Gaeta, and M. Lipson, “CMOS-compatible multiple-wavelength oscillator for on-chip optical interconnects,” *Nat. Photonics*, vol. 4, no. 1, pp. 37–40, 2010.

[65] N. Sherwood-Droz and M. Lipson, “Scalable 3D dense integration of photonics on bulk silicon,” *Opt. Express*, vol. 19, no. 18, pp. 17758–17765, 2011.

[66] C. Lacava *et al.*, “Si-rich silicon nitride for nonlinear signal processing applications,” *Sci. Rep.*, vol. 7, no. 1, p. 22, 2017.

[67] E. Vianello *et al.*, “Impact of the charge transport in the conduction band on the retention of Si-nitride based memories,” in *Solid-State Device Research Conference, 2008. ESSDERC 2008. 38th European*, 2008, pp. 107–110.

[68] S. K. Selvaraja *et al.*, “Low-loss amorphous silicon-on-insulator technology for photonic integrated circuitry,” *Opt. Commun.*, vol. 282, no. 9, pp. 1767–1770, 2009.

[69] K. Furuya *et al.*, “Nanometer-scale thickness control of amorphous silicon using isotropic wet-etching and low loss wire waveguide fabrication with the etched material,” *Appl. Phys. Lett.*, vol. 100, no. 25, p. 251108, 2012.

[70] R. Takei, S. Manako, E. Omoda, Y. Sakakibara, M. Mori, and T. Kamei, “Sub-1 dB/cm submicrometer-scale amorphous silicon waveguide for backend on-chip optical interconnect,” *Opt. Express*, vol. 22, no. 4, pp. 4779–4788, 2014.

[71] G. Cocorullo, F. G. Della Corte, R. De Rosa, I. Rendina, A. Rubino, and E. Terzini, “Amorphous silicon-based guided-wave passive and active devices for silicon integrated optoelectronics,” *IEEE J. Sel. Top. quantum Electron.*, vol. 4, no. 6, pp. 997–1002, 1998.

[72] S. Rao, C. D’Addio, and F. G. Della Corte, “All-optical modulation in a CMOS-compatible amorphous silicon-based device,” *J. Eur. Opt. Soc. Publ.*, vol. 7, 2012.

[73] K. Narayanan and S. F. Preble, “Optical nonlinearities in hydrogenated-amorphous silicon waveguides,” *Opt. Express*, vol. 18, no. 9, pp. 8998–9005, 2010.

[74] A. C. Foster, “Advances in amorphous silicon waveguides for nonlinear optical signal processing,” in *Summer Topicals Meeting Series (SUM), 2015*, 2015, pp. 90–91.

[75] X. Gai, D.-Y. Choi, and B. Luther-Davies, “Negligible nonlinear absorption in hydrogenated amorphous silicon at 1.55 $μ$m for ultra-fast nonlinear signal processing,” *Opt. Express*, vol. 22, no. 8, pp. 9948–9958, 2014.

[76] R. A. Street, *Hydrogenated amorphous silicon*. Cambridge University Press, 2005.

[77] C. Jacoboni, C. Canali, G. Ottaviani, and A. A. Quaranta, "A review of some charge transport properties of silicon," *Solid. State. Electron.*, vol. 20, no. 2, pp. 77–89, 1977.

[78] D. Kwong, J. Covey, A. Hosseini, Y. Zhang, X. Xu, and R. T. Chen, "Ultralow-loss polycrystalline silicon waveguides and high uniformity 1x12 MMI fanout for 3D photonic integration," *Opt. Express*, vol. 20, no. 19, pp. 21722–21728, 2012.

[79] P. Dumon *et al.*, "Low-loss SOI photonic wires and ring resonators fabricated with deep UV lithography," *IEEE Photonics Technol. Lett.*, vol. 16, no. 5, pp. 1328–1330, 2004.

[80] T. Tsuchizawa, K. Yamada, H. Fukuda, T. Watanabe, S. Uchiyama, and S. Itabashi, "Low-loss Si wire waveguides and their application to thermooptic switches," *Jpn. J. Appl. Phys.*, vol. 45, no. 8S, p. 6658, 2006.

[81] R. Claps, D. Dimitropoulos, V. Raghunathan, Y. Han, and B. Jalali, "Observation of stimulated Raman amplification in silicon waveguides," *Opt. Express*, vol. 11, no. 15, pp. 1731–1739, 2003.

[82] K. Yamada, H. Fukuda, T. Tsuchizawa, T. Watanabe, T. Shoji, and S. Itabashi, "All-optical efficient wavelength conversion using silicon photonic wire waveguide," *IEEE Photonics Technol. Lett.*, vol. 18, no. 9, pp. 1046–1048, 2006.

[83] I.-W. Hsieh *et al.*, "Supercontinuum generation in silicon photonic wires," *Opt. Express*, vol. 15, no. 23, pp. 15242–15249, 2007.

[84] M. A. Foster, A. C. Turner, J. E. Sharping, B. S. Schmidt, M. Lipson, and A. L. Gaeta, "Broad-band optical parametric gain on a silicon photonic chip," *Nature*, vol. 441, no. 7096, pp. 960–963, 2006.

[85] L. Shen, "Semiconductor waveguides for mid-infrared photonics," University of Southampton, 2015.

[86] M. A. Green and M. J. Keevers, "Optical properties of intrinsic silicon at 300 K," *Prog. Photovoltaics Res. Appl.*, vol. 3, no. 3, pp. 189–192, 1995.

[87] S. Gall, M. Muske, I. Sieber, O. Nast, and W. Fuhs, "Aluminum-induced crystallization of amorphous silicon," *J. Non. Cryst. Solids*, vol. 299, pp. 741–745, 2002.

[88] Z. Jin, G. A. Bhat, M. Yeung, H. S. Kwok, and M. Wong, "Nickel induced crystallization of amorphous silicon thin films," *J. Appl. Phys.*, vol. 84, no. 1, pp. 194–200, 1998.

[89] A. M. Mahamad and G. K. Mamidipudi, "Metal induced crystallization," in *Crystallization-Science and Technology*, InTech, 2012.

[90] S. Y. Yoon, K. H. Kim, C. O. Kim, J. Y. Oh, and J. Jang, "Low temperature metal induced crystallization of amorphous silicon using a Ni solution," *J. Appl. Phys.*, vol. 82, no. 11, pp. 5865–5867, 1997.

[91] R. Kishore, A. K. Srivastava, H. A. Naseem, and W. D. Brown, "Aluminum induced crystallization of amorphous silicon: Microstructural and crystallographic investigations," in *Physics of Semiconductor Devices, 2007. IWPSD 2007. International Workshop on*, 2007, pp. 217–220.

[92] Y.-C. Wu *et al.*, "High-performance metal-induced lateral-crystallization polysilicon thin-film transistors with multiple nanowire channels and multiple gates," *IEEE Trans. Nanotechnol.*, vol. 5, no. 3, pp. 157–162, 2006.

[93] B.-R. Wu *et al.*, "Direct growth of large grain polycrystalline silicon films on aluminum-induced crystallization seed layer using hot-wire chemical vapor deposition," *Thin Solid Films*, vol. 520, no. 18, pp. 5860–5866, 2012.

[94] K. F. Kelton, A. L. Greer, and C. V Thompson, "Transient nucleation in condensed systems," *J. Chem. Phys.*, vol. 79, no. 12, pp. 6261–6276, 1983.

[95] V. Subramanian, "Control of nucleation and grain growth in solid-phase crystallized silicon for high-performance thin film transistors," Stanford University, 1998.

[96] M. Çelikbilek, A. E. Ersundu, and S. Aydin, "Crystallization kinetics of amorphous materials," in *Advances in crystallization processes*, InTech, 2012.

[97] Q. Fang, J. F. Song, S. H. Tao, M. B. Yu, G. Q. Lo, and D. L. Kwong, "Low loss (~ 6.45 dB/cm) sub-micron polycrystalline silicon waveguide integrated with efficient SiON waveguide coupler," *Opt. Express*, vol. 16, no. 9, pp. 6425–6432, 2008.

[98] S.-M. Han, M.-C. Lee, M.-Y. Shin, J.-H. Park, and M.-K. Han, "Poly-Si TFT Fabricated at 150 deg C Using ICP-CVD and Excimer Laser Annealing," *Proc. IEEE*, vol. 93, no. 7, pp. 1297–1305, 2005.

[99] J. S. Im, H. J. Kim, and M. O. Thompson, "Phase transformation mechanisms involved in excimer laser crystallization of amorphous silicon films," *Appl. Phys. Lett.*, vol. 63, no. 14, pp. 1969–1971, 1993.

[100] M. Hatano, S. Moon, M. Lee, K. Suzuki, and C. P. Grigoropoulos, "Excimer laser-induced temperature field in melting and resolidification of silicon thin films," *J. Appl. Phys.*, vol. 87, no. 1, pp. 36–43, 2000.

[101] M. Lee, S. Moon, M. Hatano, K. Suzuki, and C. P. Grigoropoulos, "Relationship between fluence gradient and lateral grain growth in spatially controlled excimer laser crystallization of amorphous silicon films," *J. Appl. Phys.*, vol. 88, no. 9, pp. 4994–4999, 2000.

[102] R. S. Sposili and J. S. Im, "Sequential lateral solidification of thin silicon films on SiO2," *Appl. Phys. Lett.*, vol. 69, no. 19, pp. 2864–2866, 1996.

[103] J. Perrière, E. Millon, and E. Fogarassy, *Recent advances in laser processing of materials*.

Elsevier, 2006.

[104] K. Preston, C. B. Poitras, M. O. Thompson, and M. Lipson, "Photonic devices in low-temperature laser-crystallized deposited silicon," in *Conference on Lasers and Electro-Optics*, 2010, p. CThW4.

[105] K. Ishikawa, M. Ozawa, C.-H. Oh, and M. Matsumura, "Excimer-laser-induced lateral-growth of silicon thin-films," *Jpn. J. Appl. Phys.*, vol. 37, no. 3R, p. 731, 1998.

[106] A. Hara *et al.*, "High-performance polycrystalline silicon thin film transistors on non-alkali glass produced using continuous wave laser lateral crystallization," *Jpn. J. Appl. Phys.*, vol. 41, no. 3B, p. L311, 2002.

[107] S. J. Park *et al.*, "CW laser crystallization of amorphous silicon; dependence of amorphous silicon thickness and pattern width on the grain size," *Thin Solid Films*, vol. 511, pp. 243–247, 2006.

[108] A. Hara *et al.*, "High performance low temperature polycrystalline silicon thin film transistors on non-alkaline glass produced using diode pumped solid state continuous wave laser lateral crystallization," *Jpn. J. Appl. Phys.*, vol. 43, no. 4R, p. 1269, 2004.

[109] C.-H. Chou *et al.*, "High-Performance Single-Crystal-Like Strained-Silicon Nanowire Thin-Film Transistors Via Continuous-Wave Laser Crystallization," *IEEE Electron Device Lett.*, vol. 36, no. 4, pp. 348–350, 2015.

[110] A. Yadav and P. Agarwal, "Laser Induced Selective Crystallization of Amorphous Silicon Thin Film for Device Applications," *Mater. Today Proc.*, vol. 4, no. 14, pp. 12722–12725, 2017.

[111] A. C. Jones and M. L. Hitchman, "Overview of chemical vapour deposition," *Chem. Vap. Depos. Precursors, Process. Appl.*, pp. 1–36, 2009.

[112] F. Gaspari, "Optoelectronic properties of amorphous silicon the role of hydrogen: from experiment to modeling," in *Optoelectronics-Materials and Techniques*, InTech, 2011.

[113] T. N. Bell, K. A. Perkins, and P. G. Perkins, "Kinetics and mechanism of silane decomposition. Silanes and disilanes containing silicon-hydrogen bonds," *J. Phys. Chem.*, vol. 88, no. 1, pp. 116–118, 1984.

[114] D. J. Lockwood and L. Pavesi, *Silicon photonics II: components and integration series: topics in applied physics*. Springer, Berlin, 2011.

[115] V. Lindroos, M. Tilli, A. Lehto, and T. Motooka, *Handbook of silicon based MEMS materials and technologies*. William Andrew, 2010.

[116] L. Vivien and L. Pavesi, *Handbook of silicon photonics*. Taylor & Francis, 2013.

[117] A. C. Jones and M. L. Hitchman, *Chemical vapour deposition: precursors, processes and*

applications. Royal Society of Chemistry, 2009.

[118] R. E. I. Schropp, B. Stannowski, A. M. Brockhoff, P. Van Veenendaal, and J. K. Rath, "Hot wire CVD of heterogeneous and polycrystalline silicon semiconducting thin films for application in thin film transistors and solar cells," *Mater. Phys. Mech*, vol. 1, no. 2, pp. 73–82, 2000.

[119] W. Van Sark, "Methods of deposition of hydrogenated amorphous silicon for device applications," *Thin Film. Nanostructures*, vol. 30, pp. 1–216, 2002.

[120] A. H. Mahan, J. Carapella, B. P. Nelson, R. S. Crandall, and I. Balberg, "Deposition of device quality, low H content amorphous silicon," *J. Appl. Phys.*, vol. 69, no. 9, pp. 6728–6730, 1991.

[121] J. W. Marvin and J. Weber, "Handbook of optical materials," *Laser Opt. Sci. Technol. Ser. CRC Press. Append. V. ISBN*, pp. 970–978, 2003.

[122] S. Moon, M. Hatano, M. Lee, and C. P. Grigoropoulos, "Thermal conductivity of amorphous silicon thin films," *Int. J. Heat Mass Transf.*, vol. 45, no. 12, pp. 2439–2447, 2002.

[123] A. S. Mujumdar, *Handbook of industrial drying*. CRC press, 2014.

[124] T. Ben Masaud, "Development of low temperature fabrication processes of n-ZnO/p-Si optical switch and poly-silicon waveguides for CMOS-compatible multi-layered silicon photonics," University of Southampton, 2014.

[125] M. Quirk and J. Serda, *Semiconductor manufacturing technology*, vol. 1. Prentice Hall Upper Saddle River, NJ, 2001.

[126] M. J. Madou, *Manufacturing techniques for microfabrication and nanotechnology*, vol. 2. CRC press, 2011.

[127] D. Li, *Encyclopedia of microfluidics and nanofluidics*. Springer Science & Business Media, 2008.

[128] V. R. Almeida, C. A. Barrios, R. R. Panepucci, and M. Lipson, "All-optical control of light on a silicon chip," *Nature*, vol. 431, no. 7012, pp. 1081–1084, 2004.

[129] N. F. Baril *et al.*, "Confined high-pressure chemical deposition of hydrogenated amorphous silicon," *J. Am. Chem. Soc.*, vol. 134, no. 1, pp. 19–22, 2011.

[130] S. Morris *et al.*, "Semiconductor Core Optical Fibers," *IEEE Photonics J.*, vol. 3, no. 2, pp. 259–262, 2011.

[131] J. Ballato and E. Snitzer, "Fabrication of fibers with high rare-earth concentrations for Faraday isolator applications," *Appl. Opt.*, vol. 34, no. 30, pp. 6848–6854, 1995.

[132] S. Shabahang, J. J. Kaufman, D. S. Deng, and A. F. Abouraddy, "Observation of the Plateau-

Rayleigh capillary instability in multi-material optical fibers," *Appl. Phys. Lett.*, vol. 99, no. 16, p. 161909, 2011.

[133] S. Y. Lin and C. W. Dence, *Methods in lignin chemistry*. Springer Science & Business Media, 2012.

[134] S. K. Gupta and P. K. Jha, "Modified phonon confinement model for size dependent Raman shift and linewidth of silicon nanocrystals," *Solid State Commun.*, vol. 149, no. 45, pp. 1989–1992, 2009.

[135] S. Anwar, M. Y. A. Raja, S. Qazi, and M. Ilyas, *Nanotechnology for telecommunications*. Crc Press, 2010.

[136] G. Gouadec and P. Colomban, "Raman Spectroscopy of nanomaterials: How spectra relate to disorder, particle size and mechanical properties," *Prog. Cryst. growth Charact. Mater.*, vol. 53, no. 1, pp. 1–56, 2007.

[137] F. W. J. Olver, *NIST handbook of mathematical*. Cambridge University Press, 2010.

[138] M. Gołkabczak and A. Konstantynowicz, "Raman spectra evaluation of the carbon layers with Voigt profile," *J. Achiev. Mater. Manuf. Eng.*, vol. 37, no. 2, pp. 270–276, 2009.

[139] B. Di Bartolo, *Optical interactions in solids*. World Scientific Publishing Co Inc, 2010.

[140] C. L. Mayfield and M. N. Huda, "The effect of hydrogen passivation on Si nanocrystals: Surface and spin states," *Comput. Theor. Chem.*, vol. 1019, pp. 125–131, 2013.

[141] I. H. Campbell and P. M. Fauchet, "The effects of microcrystal size and shape on the one phonon Raman spectra of crystalline semiconductors," *Solid State Commun.*, vol. 58, no. 10, pp. 739–741, 1986.

[142] Y. Ji, D. Shan, M. Qian, J. Xu, W. Li, and K. Chen, "Formation of high conductive nano-crystalline silicon embedded in amorphous silicon-carbide films with large optical band gap," *AIP Adv.*, vol. 6, no. 10, p. 105107, 2016.

[143] C. Droz, E. Vallat-Sauvain, J. Bailat, L. Feitknecht, J. Meier, and A. Shah, "Relationship between Raman crystallinity and open-circuit voltage in microcrystalline silicon solar cells," *Sol. Energy Mater. Sol. Cells*, vol. 81, no. 1, pp. 61–71, 2004.

[144] C.-Y. Peng *et al.*, "Comprehensive study of the Raman shifts of strained silicon and germanium," *J. Appl. Phys.*, vol. 105, no. 8, p. 83537, 2009.

[145] I. De Wolf, "Micro-Raman spectroscopy to study local mechanical stress in silicon integrated circuits," *Semicond. Sci. Technol.*, vol. 11, no. 2, p. 139, 1996.

[146] H. S. Nalwa, *Silicon-based material and devices, two-volume set: materials and processing, Properties and Devices*, vol. 1. Academic Press, 2001.

[147] M. H. Brodsky, M. Cardona, and J. J. Cuomo, “Infrared and Raman spectra of the silicon-hydrogen bonds in amorphous silicon prepared by glow discharge and sputtering,” *Phys. Rev. B*, vol. 16, no. 8, p. 3556, 1977.

[148] V. A. Volodin and D. I. Koshelev, “Quantitative analysis of hydrogen in amorphous silicon using Raman scattering spectroscopy,” *J. Raman Spectrosc.*, vol. 44, no. 12, pp. 1760–1764, 2013.

[149] W. L. Bragg, “The diffraction of short electromagnetic waves by a crystal,” *Proc. Camb. Philol. Soc.*, vol. 17, pp. 43–57, 1913.

[150] D. E. Sands, *Introduction to crystallography*. Courier Corporation, 1969.

[151] C. Hammond and C. Hammond, *Basics of crystallography and diffraction*, vol. 214. Oxford, 2001.

[152] P. J. Mohr, B. N. Taylor, and D. B. Newell, “CODATA recommended values of the fundamental physical constants: 2010 a,” *J. Phys. Chem. Ref. Data*, vol. 84, no. 4, p. 1527, 2012.

[153] H. E. Swanson, E. Tatge, and R. K. Fuyat, “Standard X-ray diffraction powder patterns,” 1953.

[154] M. E. Fitzpatrick, A. T. Fry, P. Holdway, F. A. Kandil, J. Shackleton, and L. Suominen, “Determination of residual stresses by X-ray diffraction,” 2005.

[155] I. C. Noyan, T. C. Huang, and B. R. York, “Residual stress/strain analysis in thin films by X-ray diffraction,” *Crit. Rev. Solid State Mater. Sci.*, vol. 20, no. 2, pp. 125–177, 1995.

[156] M. Tateda, T. Horiguchi, M. Tokuda, and N. Uchida, “Optical loss measurement in graded-index fiber using a dummy fiber,” *Appl. Opt.*, vol. 18, no. 19, pp. 3272–3275, 1979.

[157] S. Taebi, M. Khorasaninejad, and S. S. Saini, “Modified Fabry-Perot interferometric method for waveguide loss measurement,” *Appl. Opt.*, vol. 47, no. 35, pp. 6625–6630, 2008.

[158] A. De Rossi *et al.*, “Measuring propagation loss in a multimode semiconductor waveguide,” *J. Appl. Phys.*, vol. 97, no. 7, p. 73105, 2005.

[159] R. P. Prasankumar and A. J. Taylor, *Optical techniques for solid-state materials characterization*. CRC Press, 2016.

[160] C. A. Valenzuela, *Design and demonstration of a near-field optical instrument for study of data storage with organometallic materials*. Herbert Utz Verlag, 1997.

[161] E. Wolf, *Progress in Optics, Volume 49*. Elsevier, 1993.

[162] E. Iannone, *Labs on chip: Principles, design and technology*. CRC Press, 2014.

[163] S. Knief and W. von Niessen, “Disorder, defects, and optical absorption in a-Si and a-Si:H,”

Phys. Rev. B, vol. 59, no. 20, p. 12940, 1999.

[164] F. Zhu and J. Singh, "Approach to study the relation between optical energy gap and hydrogen concentration in hydrogenated amorphous silicon thin films," *J. Appl. Phys.*, vol. 73, no. 9, pp. 4709–4711, 1993.

[165] E. L. Mathe, A. Naudon, M. Elliq, E. Fogarassy, and S. De Unamuno, "Influence of hydrogen on the structure and surface morphology of pulsed ArF excimer laser crystallized amorphous silicon thin films," *Appl. Surf. Sci.*, vol. 54, pp. 392–400, 1992.

[166] P. Walker and W. H. Tarn, *CRC handbook of metal etchants*. CRC press, 1990.

[167] B. L. Sopori, "A new defect etch for polycrystalline silicon," *J. Electrochem. Soc.*, vol. 131, no. 3, pp. 667–672, 1984.

[168] G. D. Ivlev and E. I. Gatskevich, "Liquid phase reflectivity under conditions of laser-induced silicon melting," *Semiconductors*, vol. 34, no. 7, pp. 759–762, 2000.

[169] D. K. Biegelsen, L. E. Fennell, and J. C. Zesch, "Origin of oriented crystal growth of radiantly melted silicon on SiO2," *Appl. Phys. Lett.*, vol. 45, no. 5, pp. 546–548, 1984.

[170] S. H. Simon, *The Oxford solid state basics*. OUP Oxford, 2013.

[171] R. Boyd, *Nonlinear optics (Thrid edition)*. Academic Press, 2008.

[172] F. Träger, *Springer handbook of lasers and optics*. Springer Science & Business Media, 2012.

[173] S. Fathpour and B. Jalali, *Silicon photonics for telecommunications and biomedicine*. CRC Press, 2011.

[174] L. Yin and G. P. Agrawal, "Impact of two-photon absorption on self-phase modulation in silicon waveguides," *Opt. Lett.*, vol. 32, no. 14, pp. 2031–2033, 2007.

[175] G. P. Agrawal, "Nonlinear fiber optics," in *Nonlinear Science at the Dawn of the 21st Century*, Springer, 2000, pp. 195–211.

[176] L. Yin, Q. Lin, and G. P. Agrawal, "Soliton fission and supercontinuum generation in silicon waveguides," *Opt. Lett.*, vol. 32, no. 4, pp. 391–393, 2007.

[177] Q. Xu and M. Lipson, "Carrier-induced optical bistability in silicon ring resonators," *Opt. Lett.*, vol. 31, no. 3, pp. 341–343, 2006.

[178] A. C. Turner *et al.*, "Tailored anomalous group-velocity dispersion in silicon channel waveguides," *Opt. Express*, vol. 14, no. 10, pp. 4357–4362, 2006.

[179] M. Dinu, F. Quochi, and H. Garcia, "Third-order nonlinearities in silicon at telecom wavelengths," *Appl. Phys. Lett.*, vol. 82, no. 18, pp. 2954–2956, 2003.

[180] H. K. Tsang *et al.*, "Optical dispersion, two-photon absorption and self-phase modulation in silicon waveguides at 1.5 $μ$ m wavelength," *Appl. Phys. Lett.*, vol. 80, no. 3, pp. 416–418,

2002.

[181] G. W. Rieger, K. S. Virk, and J. F. Young, “Nonlinear propagation of ultrafast 1.5 $μ$m pulses in high-index-contrast silicon-on-insulator waveguides,” *Appl. Phys. Lett.*, vol. 84, no. 6, pp. 900–902, 2004.

[182] T. M. Ben Masaud *et al.*, “Hot-wire polysilicon waveguides with low deposition temperature,” *Opt. Lett.*, vol. 38, no. 20, pp. 4030–4032, 2013.

[183] A. Gumennik *et al.*, “Silicon-in-silica spheres via axial thermal gradient in-fibre capillary instabilities,” *Nat. Commun.*, vol. 4, p. 2216, 2013.

[184] R. Wang *et al.*, “Raman spectral study of silicon nanowires: high-order scattering and phonon confinement effects,” *Phys. Rev. B*, vol. 61, no. 24, p. 16827, 2000.

[185] N. Healy, J. R. Sparks, P. J. A. Sazio, J. V Badding, and A. C. Peacock, “Tapered silicon optical fibers,” *Opt. Express*, vol. 18, no. 8, pp. 7596–7601, 2010.

[186] B. L. Scott and G. R. Pickrell, “Silicon optical fiber diameter dependent grain size,” *J. Cryst. Growth*, vol. 371, pp. 134–141, 2013.

[187] A. C. Peacock, “Soliton propagation in tapered silicon core fibers,” *Opt. Lett.*, vol. 35, no. 21, pp. 3697–3699, 2010.